

Structure and Bonding in Thiolate-Coated Au Nanostructures

by

Stephen Lynd Christensen

Submitted in partial fulfillment of the requirements
for the degree of Doctor of Philosophy

at

Dalhousie University
Halifax, Nova Scotia
April 2013

© Copyright by Stephen Lynd Christensen, 2013

DALHOUSIE UNIVERSITY
DEPARTMENT OF CHEMISTRY

The undersigned hereby certify that they have read and recommend to the Faculty of Graduate Studies for acceptance a thesis entitled "Structure and Bonding in Thiolate-Coated Au Nanostructure" by Stephen Lynd Christensen in partial fulfilment of the requirements for the degree of Doctor of Philosophy.

Dated: April 26, 2013

External Examiner: _____

Research Co- _____

Supervisors: _____

Examining Committee: _____

Departmental Representative: _____

DALHOUSIE UNIVERSITY

DATE: April 26, 2013

AUTHOR: Stephen Lynd Christensen

TITLE: Structure and Bonding in Thiolate-Coated Au Nanostructures

DEPARTMENT OR SCHOOL: Department of Chemistry

DEGREE: PhD CONVOCATION: October YEAR: 2013

Permission is herewith granted to Dalhousie University to circulate and to have copied for non-commercial purposes, at its discretion, the above title upon the request of individuals or institutions. I understand that my thesis will be electronically available to the public.

The author reserves other publication rights, and neither the thesis nor extensive extracts from it may be printed or otherwise reproduced without the author's written permission.

The author attests that permission has been obtained for the use of any copyrighted material appearing in the thesis (other than the brief excerpts requiring only proper acknowledgement in scholarly writing), and that all such use is clearly acknowledged.

Signature of Author

TABLE OF CONTENTS

LIST OF TABLES	vi
LIST OF FIGURES	vii
ABSTRACT	xii
LIST OF ABBREVIATIONS USED	xiii
ACKNOWLEDGEMENTS.....	xiv
CHAPTER 1 INTRODUCTION.....	1
1.1 NANOMATERIALS IN BRIEF	1
1.2 HISTORY OF GOLD NANOSTRUCTURES.....	1
1.3 PROPERTIES.....	4
1.3.1 <i>Optical Properties</i>	4
1.3.2 <i>Electronic Properties</i>	4
1.3.3 <i>Chemical Properties</i>	7
1.3.4 <i>Unique Structure</i>	8
1.4 POTENTIAL APPLICATIONS	10
1.4.1 <i>Orthopaedic Applications</i>	10
1.4.2 <i>Catalysis</i>	12
1.5 CHALLENGES IN SYNTHESIS AND CHARACTERIZATION	14
1.5.1 <i>Synthetic Challenges</i>	14
1.5.2 <i>Challenges in Characterization</i>	15
1.6 OVERVIEW OF THESIS	16
1.6.1 <i>Thesis Motivation</i>	16
1.6.2 <i>Structure of Thesis</i>	17
CHAPTER 2 METHODS	20
2.1 SYNTHESIS.....	20
2.1.1 <i>Solution-based Synthesis</i>	20
2.1.2 <i>Substrate-based Synthesis</i>	21
2.2 MODEL BIOMOLECULES	25
2.3 CHARACTERIZATION TECHNIQUES.....	26
2.3.1 <i>Scanning Electron Microscopy (SEM)</i>	26
2.3.2 <i>Synchrotron Radiation</i>	28
2.3.3 <i>X-Ray Photoelectron Spectroscopy (XPS)</i>	30
2.3.4 <i>X-Ray Absorption Spectroscopy (XAS)</i>	32
2.3.5 <i>X-Ray Absorption Near-Edge Structure (XANES) Spectroscopy</i>	34
2.3.6 <i>Extended X-Ray Absorption Fine-Structure (EXAFS) Spectroscopy</i>	35
2.4 COMPUTATIONAL STUDIES.....	39
2.4.1 <i>FEFF Calculations</i>	40
2.4.2 <i>Crystal and Molecule Modeling Software</i>	40
CHAPTER 3 LIGAND EFFECT (PART 1).....	42
3.0 MOTIVATION.....	42
3.1 INTRODUCTION.....	42
3.2 EXPERIMENTAL	44
3.2.1 <i>Synthesis</i>	44
3.2.2 <i>Characterization</i>	45
3.3 RESULTS AND DISCUSSION	47
3.4 SUMMARY	65

CHAPTER 4 LIGAND EFFECT (PART 2)	67
4.0 MOTIVATION.....	67
4.1 INTRODUCTION.....	67
4.2 EXPERIMENTAL.....	69
4.2.1 <i>Synthesis</i>	69
4.2.2 <i>Characterization</i>	70
4.3 RESULTS AND DISCUSSION.....	71
4.4 SUMMARY.....	84
CHAPTER 5 METAL EFFECT (PART 1)	85
5.0 MOTIVATION.....	85
5.1 INTRODUCTION.....	85
5.2 EXPERIMENTAL.....	88
5.3 RESULTS AND DISCUSSION.....	89
5.3.1 <i>Local Coordination Environment</i>	89
5.3.2 <i>Electronic Properties</i>	94
5.4 SUMMARY.....	97
CHAPTER 6 METAL EFFECT (PART 2)	99
6.0 MOTIVATION.....	99
6.1 INTRODUCTION.....	99
6.2 EXPERIMENTAL.....	101
6.2.1 <i>Synthesis and Mass Spectroscopy Characterization</i>	101
6.2.2 <i>X-ray Spectroscopy and Calculations</i>	101
6.2.3 <i>Calculations</i>	102
6.3 RESULTS AND DISCUSSION.....	103
6.3.1 <i>Dopant Location</i>	103
6.3.2 <i>Local Structure</i>	109
6.3.3 <i>Electronic Properties</i>	111
6.4 SUMMARY.....	117
CHAPTER 7 CONCLUSIONS AND FUTURE WORK	118
7.1 CONCLUSIONS.....	118
7.2 FUTURE WORK.....	120
REFERENCES	122
APPENDIX A	135
A-1. STUDY OF SILVER NANOPARTICLES.....	135
<i>Ag:BSA Systems</i>	135
<i>Ag:MPG Systems</i>	137
APPENDIX B	141
B-1. COPYRIGHT AGREEMENT LETTER – CHAPTER 3.....	141
B-2. COPYRIGHT AGREEMENT LETTER – CHAPTER 4.....	142
B-3. COPYRIGHT AGREEMENT LETTER – CHAPTER 6.....	143

LIST OF TABLES

Table 2-1. Model biomolecules and their structure.....	25
Table 3-1. Au L ₃ -edge R-Space EXAFS Fitting Results for 20AuBSA and 20AuMPG systems, as well as Au foil for comparison.....	52
Table 3-2. Metal:S ratios from XPS survey scan spectra.....	55
Table 4-1. Au L ₃ -Edge EXAFS Fit Results for AuMPG, AuGSH, bare Au Nanoparticles, and Au-Thiolate Polymer Systems.....	81
Table 6-1. XPS Compositional analysis data of the Au ₂₄ Pt sample.....	105
Table 6-2. Pt L ₃ -edge EXAFS fit results of Au ₂₄ Pt.....	107
Table 6-3. Au L ₃ -edge EXAFS two-shell fit results for Au ₂₅ and Au ₂₄ Pt.....	110
Table 6-4. Site-specific comparison of the Au 4f _{7/2} XPS peak positions and full-width half-maxima for Au ₂₅ and Au ₂₄ Pt.....	112

LIST OF FIGURES

Figure 1-1. A) Roman Lycurgus Cup (Figure adapted from Johnbod, under Creative Commons Attribution-Share Alike License), B) Cover of Francisci Antonii's <i>Panacea Aurea – Auro Potabili</i> , and C) Faraday's ruby-Au colloid (Figure by Royal Institution of Great Britain).....	2
Figure 1-2. Brust-Schiffrin synthesis. (alkanethiol ligand are black and Au atoms are yellow)	3
Figure 1-3. Schematic of energy level quantization in molecular Au, small Au nanoparticles, large Au nanoparticles, and bulk metallic Au.	5
Figure 1-4. Diagram of Au ₂₅ and Au ₁₀₂ . Components of A) Au ₂₅ NP including B) icosahedral core and C) double-staple. Components of D) Au ₁₀₂ NP including E) core, F) single-staple, G) double-staple, and H) double-anchor staple structures. Ligand molecules removed and size of Au atoms adjusted for visualization purposes. Au atoms are yellow, and S atoms are red.....	9
Figure 2-1. Experimental setup for one-step procedure. A) Beaker with Ti substrate and Teflon ring, and B) graphical procedure for deposition of BSA onto Au NP-functionalized Ti surface.....	23
Figure 2-2. SEM micrographs of bare surfaces which have been etched for A) too long (~2 h) and B) an appropriate length of time (~1 h).....	24
Figure 2-3. SEM micrograph of 20:1 Au:BSA biomolecule-functionalized Au nanoparticles supported on Ti (100,000x magnification at an accelerating voltage of 20 kV).	27
Figure 2-4. General diagram of a synchrotron radiation facility.	29
Figure 2-5. Diagram depicting typical mechanisms for X-ray photoemission (XPS) and X-ray absorption (XANES and EXAFS). The orbitals are identified under traditional core-level transition nomenclature (e.g. K = 1s, L = 2s, 2p).....	31
Figure 2-6. Au L ₃ -Edge (2p _{3/2}) XAS spectrum showing near-edge (XANES), and extended post-edge (EXAFS) regions.	33
Figure 2-7. Incident photon (yellow) exciting photoelectron wave from an atom (red) and interference caused by neighbouring atoms (blue).	36
Figure 2-8. Processing of an EXAFS spectrum, depicting the corresponding A) extended region of the X-ray absorption spectrum, B) <i>k</i> -space spectrum, and C) R-space spectrum.	38

Figure 3-1. Scanning electron micrographs of bio-functionalized Au nanoparticles on Ti substrate. (A) 20:1 Au:BSA micrograph and (B) histogram, and (C) 20:1 Au:MPG micrograph and (D) histogram.	48
Figure 3-2. (A) Overlain and (B) staggered Au L ₃ -edge XANES of 20AuBSA (black solid) and 20AuMPG (red dash) systems, with Au foil (blue dot) for feature comparison.	49
Figure 3-3. Au L ₃ -edge k-space EXAFS of 20AuBSA (red circle), 20AuMPG (blue square), and bulk Au foil (black triangle) systems.	50
Figure 3-4. (A) Overlain and (B) staggered Au L ₃ -edge R-space EXAFS of 20AuBSA (black solid), 20AuMPG (red dash) systems, with bulk Au foil (blue dot) for comparison.	51
Figure 3-5. Au L ₃ -edge R-space EXAFS (black solid) and fits (red dash) of (A) 20AuBSA and (B) 20AuMPG systems. Spectra are not corrected for phase. Fits are one-shell Au-Au path and do not include features outside of a 1.6 to 3.3 Å window.	52
Figure 3-6. Schematic illustration of biomolecule functionalized Au nanoparticle deposition for (A) protein functionalized Au nanoparticles on a Ti substrate, and (B) small model-biomolecule functionalized Au nanoparticles on a Ti substrate.	53
Figure 3-7. Au 4f _{7/2} XPS spectra of 20AuBSA (black solid) and 20AuMPG (red dash) systems, denoting broadening and shift to higher binding energy in the 20AuMPG system.	55
Figure 3-8. XPS survey scan spectra of the 20AuBSA, 20AgBSA, and 20PdBSA systems.	56
Figure 3-9. Au L ₃ -edge XANES spectra of AuBSA and AuMPG systems, comparing differences in concentration of ligand systems. (A) Overlain and (B) staggered Au L ₃ -edge XANES spectra of 20:1, 5:1, and 2:1 Au:BSA systems. (C) Overlain and (D) staggered Au L ₃ -edge XANES spectra of 20:1, 5:1, and 2:1 Au:MPG systems.	58
Figure 3-10. Scanning electron micrographs of bio-functionalized Au nanoparticles on Ti substrate. (A) 20:1 Au:BSA, (B) 5:1 Au:BSA, (C) 2:1 Au:BSA, (D) 20:1 Au:MPG, (E) 5:1 Au:MPG, and (F) 2:1 Au:MPG.	59
Figure 3-11. (A) Overlain Au 4f _{7/2} XPS spectra of 20AuBSA (black solid), 5AuBSA (red dash), and 2AuBSA (blue dot) systems, and (B) overlain Au 4f _{7/2} XPS spectra of 20AuMPG (black solid), 5AuMPG (red dash), and 2AuMPG (blue dot) systems, denoting a broadening occurring with greater concentration of the MPG ligand system, as well as a shift to higher binding energy.	59

Figure 3-12. (A) S K-edge XANES spectra of 20AuBSA (black solid), 5AuBSA (red dash), and 2AuBSA (blue dot) systems, in comparison with BSA standard (orange dash-dot), denoting the disappearance of the 2474.3 eV and 2475.7 eV disulfide bridge peaks. (B) S K-edge XANES spectra of 20AuMPG (black solid), 5AuMPG (red dash), and 2AuMPG (blue dot) systems, in comparison with MPG standard (orange dash-dot), denoting a shift toward higher incident photon energies (higher binding energies) with increases in Au-thiolate bonding.....	61
Figure 3-13. S 2p XPS spectra of 20AuBSA (black solid) and 20AuMPG (red dash) systems.....	61
Figure 3-14. Scanning electron micrographs of bio-functionalized Ag nanoparticles on Ti substrate of (A) 20:1 Ag:BSA and (B) 20:1 Ag:MPG systems. Ag L ₃ -edge XANES spectra (C) are shown of the 20AgBSA and 20AgMPG systems, as well as Ag foil for comparison. The Ag 3d _{5/2} XPS spectrum (D) denotes shift and broadening in the 20AgMPG system.....	63
Figure 3-15. Scanning electron micrographs of bio-functionalized Pd nanoparticles on Ti substrate of (A) 20:1 Pd:BSA and (B) 20:1 Pd:MPG systems. Pd L ₃ -edge XANES spectra (C) are shown of the 20PdBSA and 20PdMPG systems, as well as Pd foil for comparison. The Pd 3d XPS spectrum (D) denotes surface protection from oxidation in the 20PdBSA system.	64
Figure 4-1. Scanning electron micrographs of the bio-functionalized AuGSH systems (A-D), AuMPG systems (F-I), and bare Au nanoparticles (E) on Ti substrate (100,000x magnification @ 20 kV). HCl-etched bare Ti (J) shown for comparative purposes.	72
Figure 4-2. (A) Schematic detailing rotating sample plate setup used for glancing angle fluorescence EXAFS measurements, (B) Au L ₃ -edge XANES spectrum of 2AuMPG using spin method and (C) Au L ₃ -edge XANES spectrum of 2AuMPG without spinning the sample. Inset in (B) denotes signal after averaging several spectra. (Graphs are scaled for better comparison).....	74
Figure 4-3. Experimental Au L ₃ -edge <i>k</i> -space EXAFS spectra of the (A) AuMPG and (B) AuGSH systems, compared with bare Au NPs and Au-thiolate polymer samples.....	75
Figure 4-4. Experimental Au L ₃ -edge <i>R</i> -space EXAFS spectra of the (A) AuMPG and (B) AuGSH systems, compared with bare Au NPs and Au-thiolate polymer samples. Red box denotes region of Au-S coordination shell, blue box denotes region of Au-Au coordination shell.	76
Figure 4-5. Molecular models of A) reduced glutathione (GSH) and B) N-(2-mercapto-propionyl) glycine (MPG) (yellow: sulfur, cyan: carbon, blue: nitrogen, red: oxygen, white: hydrogen).....	79

Figure 4-6. Experimental Au L ₃ -edge EXAFS spectra and fitting of the Au-S and Au-Au coordination shells for the (A) AuMPG and (B) AuGSH systems. (black: experimental data, red: best fit envelope).....	79
Figure 4-7. Experimental Au L ₃ -edge EXAFS spectra and fitting of the Au-S and Au-Au coordination shells for the bulk Au NP and Au-thiolate oligomer systems. (black: experimental data, red: best fit envelope).....	80
Figure 4-8. Plot of EXAFS-fitted Au-Au CN of AuGSH and AuMPG peptide-Au NPs. CN values for representative reference systems (Au FCC nanoparticles, Au ₁₄₄ nanocluster, Au-SR Reference) are denoted by dotted lines.	82
Figure 5-1. Au ₁₀₂ and Au ₂₅ ⁻ models showing the double anchor, double staple, and single staple bonding motifs.	87
Figure 5-2. Averaged Au L ₃ -edge EXAFS of Au ₁₀₂ after Fourier transformation over different ranges in k-space. Spectra were normalized to Au-S peak at ~1.9 Å for comparison.....	91
Figure 5-3. Comparison of averaged Fourier-transformed Au L ₃ -edge EXAFS of Au atoms in Au ₁₀₂ and Au ₂₅ ⁻ double-staple motif.....	91
Figure 5-4. Nearest three Au-Au aurophilic interactions and their average for the A) Au ₁₀₂ and B) Au ₂₅ ⁻ systems.....	93
Figure 5-5. Graph of d-hole counts for the staple Au centres in Au ₂₅ ⁻ and Au ₁₀₂	94
Figure 5-6. Crystal structure of Au ₂₅ ⁻ nanocluster. Yellow atoms are Au, red are sulfur (additional ligand atoms are removed for clarity), blue are N (from TOA ⁺), and green are the two staple-Au sites most strongly affected by TOA ⁺	96
Figure 5-7. Distributions of averaged d-electron density of states (<i>d</i> -DOS), for double-staple Au in the Au ₁₀₂ and Au ₂₅ ⁻ nanoclusters. The Au ₁₀₂ <i>d</i> -DOS was 3-point smoothed to facilitate the comparison.	96
Figure 6-1. Positive mode matrix-assisted laser desorption ionization (MALDI) mass spectrum of Au ₂₄ Pt(SCH ₂ CH ₂ Ph) ₁₈ nanoclusters.	104
Figure 6-2. Schematic representations and theoretical coordination numbers for averaged Au-S and Pt-Au bonding in A) Au ₂₅ , B) Au ₂₄ Pt with Pt in core position, C) Au ₂₄ Pt with Pt in surface position, and D) Au ₂₄ Pt with Pt in staple position.	105
Figure 6-3. XPS survey scan spectra of the Au ₂₄ Pt nanocluster system taken with incident photon energy of 1000 eV.....	106

Figure 6-4. Experimental Pt L ₃ -edge EXAFS spectrum and fitting of the Pt-S shell....	108
Figure 6-5. Experimental Au L ₃ -edge EXAFS spectra of the Au ₂₄ Pt (black solid) and Au ₂₅ (red dashed) nanocluster systems.	109
Figure 6-7. A) High-resolution Au 4f _{7/2} XPS spectra of the Au ₂₅ (red dash), Au ₂₄ Pt (blue dot), and Au foil (black line) denoting binding energy shift of 0.19 eV (Au ₂₅) and 0.08 eV (Au ₂₄ Pt). All spectra normalized for peak height, so as to better denote binding energy shift. High-resolution Au 4f spectra of B) Au ₂₅ and C) Au ₂₄ Pt are shown, where experimental data is denoted as black dots, envelope and component fitting are denoted in red, and Shirley background is denoted as a black line. All spectra acquired with an incident photon energy of 700 eV.....	113
Figure 6-8. Calculated electron counts for 6s+p and 5d-electrons of surface gold atoms in three series of model systems based on the crystal structure of Au ₂₅ . The three systems are Au ₂₅ , Au ₂₄ Pt (central Au replaced with Pt) and Au ₂₄ (in absence of central Au atom). Models with 1% contracted bond distances (e.g. Au ₂₅ -c, Au ₂₄ Pt-c and Au ₂₄ -c) bond distance are also used in calculations in order to illustrate the lattice contraction effect. For clarity, model systems are depicted without staple motif Au and S atoms.	115
Figure A-1. SEM Micrographs of Ag:BSA on titanium system. A) 20:1 Ag:BSA, B) 5:1 Ag:BSA and C) 2:1 Ag:BSA.....	135
Figure A-2. Sulfur K-edge XANES spectra of 20:1, 5:1, and 2:1 Ag:BSA on titanium, in comparison with a BSA standard.	136
Figure A-3. XPS spectrum of Au:BSA on titanium. A) Ag 3d spectra, B) S 2p spectra with BSA standard for comparison.	137
Figure A-4. SEM Micrographs of Ag:MPG on titanium system. A) 20:1 Ag:MPG, B) 5:1 Ag:MPG and C) 2:1 Ag:MPG.	138
Figure A-5. Sulfur K-edge XANES spectra of 20:1, 5:1, and 2:1 Ag:MPG on titanium, in comparison with a MPG standard.	139
Figure A-6. XPS spectrum of Au:MPG on titanium. A) Ag 3d spectra, B) S 2p spectra with MPG standard for comparison.....	140

ABSTRACT

Structure and bonding properties of gold (Au) nanoparticles (NPs) are of great interest due to the unique size-dependent quantum-confinement effect exhibited by structures on the nanoscale. As such, Au NPs have demonstrated their potential use in a variety of fields (*e.g.* imaging, drug delivery, catalysis). The popularity of Au NPs is largely due to its versatility in synthesizing different NP compositions and surfaces. In this thesis, structure and bonding in Au NPs was examined from both surface functionalization/ligand and composition/metal bonding perspectives.

Functionalization of Au-surface with model biomolecule ligands enables formation and electroless deposition of Au NPs onto a biocompatible Ti substrate. Through variation of model biomolecule size and concentration with respect to a Au precursor, insight was gained into the formation mechanisms of Au NPs, and the processes that lead to deposition upon the Ti substrate. Furthermore, using extended X-ray absorption fine-structure (EXAFS) with sample spinning and glancing angle setup allowed us to resolve small differences in coordination, leading to new findings on fine-tuning of peptide-coated Au NP size on Ti substrates.

To explicitly analyze Au NP structure and bonding from a metallic perspective, NP model systems with precisely controlled compositions were studied with *ab initio* calculations to compare local environment and electronic character. It was determined that while surface features may be structurally similar, the effect of local environment and geometry can affect the electronic character of these features.

Finally, small Au NP samples were studied to understand the alloying effect. The position of a heteroatom dopant Pt atom within Au₂₅ has been a disputed issue, with no definitive means of determination. Using a combination of EXAFS spectra and *ab initio* calculations, it was possible to determine that the Pt atom resides in the central position of the icosahedral core. Furthermore, Pt doping in Au₂₅ resulted in a contraction of the surface Au structure, an unobserved phenomenon until now.

Through the careful and systematic comparison of Au NP systems, this thesis will contribute to a better understanding of Au local structure and bonding in ligand-functionalized substrate-supported Au NPs, as well as compositionally precise Au nanoclusters.

LIST OF ABBREVIATIONS USED

Au ₂₄ Pt	Au ₂₄ Pt(SCH ₂ CH ₂ C ₆ H ₅) ₁₈
Au ₂₅	Au ₂₅ (SCH ₂ CH ₂ C ₆ H ₅) ₁₈
Au ₃₆	Au ₃₆ (SC ₆ H ₅ C(CH ₃) ₃) ₂₄
Au ₃₈	Au ₃₈ (SCH ₂ CH ₂ C ₆ H ₅) ₂₄
Au ₁₀₂	Au ₁₀₂ (p-(SHC ₆ H ₄ CO ₂ H)) ₄₄
FCC	Face-Centered Cubic
CLS	Canadian Light Source, University of Saskatchewan, SK
CN	Coordination Number
DCM	Dichloromethane
DFT	Density Functional Theory
EXAFS	Extended X-ray Absorption Fine Structure
FLY	Fluorescence Yield
FT	Fourier-transform
HXMA	Hard X-ray Microanalysis Beamline, CLS
<i>I</i> -DOS	Local Density of States
MALDI-TOF	Matrix-Assisted Laser-Desorption Ionization – Time of Flight
NEXAFS	Near-Edge X-ray Absorption Fine Structure
NC	Nanocluster
NP	Nanoparticle
APS	Advanced Photon Source, Argonne National Labs, IL
R.S.F.	Relative Sensitivity Factor
SEM	Scanning Electron Microscopy
SGM	Spherical Grating Monochromator Beamline, CLS
SPR	Surface Plasmon Resonance
SR	Generic Thiolate Molecule
SXRMB	Soft X-ray Microcharacterization Beamline
TEY	Total Electron Yield
TOABr	Tetraoctylammonium Bromide
TON	Turnover Number
XANES	X-ray Absorption Near-Edge Structure
XAS	X-ray Absorption Spectroscopy
XPS	X-ray Photoelectron Spectroscopy
IP	Ionization Potential
UV-Vis	Ultraviolet-Visible Absorption Spectroscopy
Z	Atomic Number

ACKNOWLEDGEMENTS

I would like to thank my supervisors, Dr. Peng Zhang and Dr. Amares Chatt. Their direction, guidance, and support allowed me to accomplish much in my studies, piquing my interest in science on the nanoscale. Their leadership and bestowed knowledge will no doubt be an asset in future challenges and opportunities.

I am grateful to my advisory committee, consisting of Dr. R. Boyd, Dr. A. Doucette, and Dr. K. Hewitt, whose constructive criticism and feedback have made this project more scientifically rigorous and robust.

The Zhang Group, consisting of J. Daniel Padmos, Mark MacDonald, Zac Cormier, Paul Duchesne, and Dan Chevrier deserve recognition for their support, as do Dr. Yongfeng Hu, Dr. Ning Chen, and Dr. Tom Regier of the Canadian Light Source, Dr. Robert Gordon of the Advanced Photon Source, Dr. Ross Dickson of Atlantic Computational Excellence Network, and Patricia Scallion of the Institute for Research in Materials.

Finally, to my family I am enormously grateful. My wife Morgan, my son Joah, my parents Helen and Brian, my sister Amanda, and my in-laws Terri, Barry, and Jenna, have all been exceptionally understanding and encouraging. If not for their love, support, and wisdom, I would not be where I am today.

CHAPTER 1 INTRODUCTION

1.1 Nanomaterials in Brief

Nanoscale materials, defined as having at least one dimension on the nanometer scale (normally 1-100 nm), are of interest due to their unique size-dependent properties. Nanoscale materials (nanomaterials) may behave differently than their bulk counterparts, exhibiting new and unique physicochemical properties. Changes in composition,¹⁻³ shape (*e.g.* spheres, cubes, wires),⁴⁻⁷ and size (*e.g.* particles, clusters)⁸⁻¹⁰ can all exhibit unique and interesting characteristics. Nanomaterials have garnered much interest because of their tunable size and structure, leading to unique and attractive properties for a variety of applications.¹¹ As examples, CdSe quantum dots photoluminesce at a large range of wavelengths, while no luminescence occurs in the bulk material,¹² while a single atom of Mn can impart a magnetic moment on some small Au nanoparticles.¹³ Though all metal nanomaterials behave differently than their bulk counterparts, it is Au nanomaterials which are amongst the most widely used and studied in nanoscience and nanotechnology.

1.2 History of Gold Nanostructures

The first documented uses of colloidal Au can be traced back to ~300 C.E. where a Roman goblet, referred to as the Lycurgus Cup, was determined to use colloidal Au as a colorant in a glass diorama on the outside of the cup (Figure 1-1A).¹⁴ Though the reason for why their dye exhibited colour was unknown, it is a prime example of the unique size-dependant optical properties exhibited by nanoscale Au. More than a millennium later, in 1618, an alchemist by the name of Francisci Antonii published a book, the *Panacea Aurea* –

Auro Potabili (Figure 1-1B) on the preparation and curative properties of colloidal Au, often referred to as “potable gold”, which was thought to cure one of all ailments.^{15,16}

The first documented synthesis of colloidal Au was by Michael Faraday in 1857, where he reduced a Au salt solution with phosphorus.¹⁷ The resulting product, when dried, was a thin colloid film that underwent reversible colour change with applied pressure.¹⁷ Furthermore, Faraday was the first to suggest that the colour of colloidal Au was due to its “minute size”.¹⁷



Figure 1-1. A) Roman Lycurgus Cup (Figure adapted from Johnbod, under Creative Commons Attribution-Share Alike License),¹⁸ B) Cover of Francisci Antonii’s *Panacea Aurea – Auro Potabili*,¹⁶ and C) Faraday’s ruby-Au colloid (Figure by Royal Institution of Great Britain).¹⁷

Little progress in nanomaterials was made for almost a century when, in 1951, Turkevich *et al.* developed a method to simultaneously cap and reduce Au salt using sodium citrate.¹⁹ The Turkevich method allowed the reproducible synthesis of relatively monodisperse Au nanoparticles (NPs) in aqueous solutions, which are ~10-20 nm in size depending on the ratio of Au to citrate used. In 1994, four decades after development of the

Turkevich method, Brust and Shiffrin developed a method to synthesize Au NPs in organic solutions (Figure 1-2).²⁰ Using tetraoctylammonium bromide (TOABr) to stabilize the Au NPs in toluene solution, and aqueous sodium borohydride (NaBH_4) to reduce the particles, the Brust method allows the synthesis to take advantage of surface Au-S bonding.²⁰ Introduction of the aqueous NaBH_4 to the Au/toluene solution forms the Au NPs at the solvent interface. This creates a more monodisperse product, because of the slower reaction rate at the phase interface. This enabled Au NPs to be stabilized by a thiolate ligand of choice, producing Au NPs which could be dried, and re-dispersed as needed for careful and detailed studies. Drying the Au NPs increases the stability, allowing for long term storage with minimal structural change. By changing the thiolate-ligand R-group (HS-R), the size and shape of Au NPs could be varied, resulting in size-controlled and monodispersed systems.

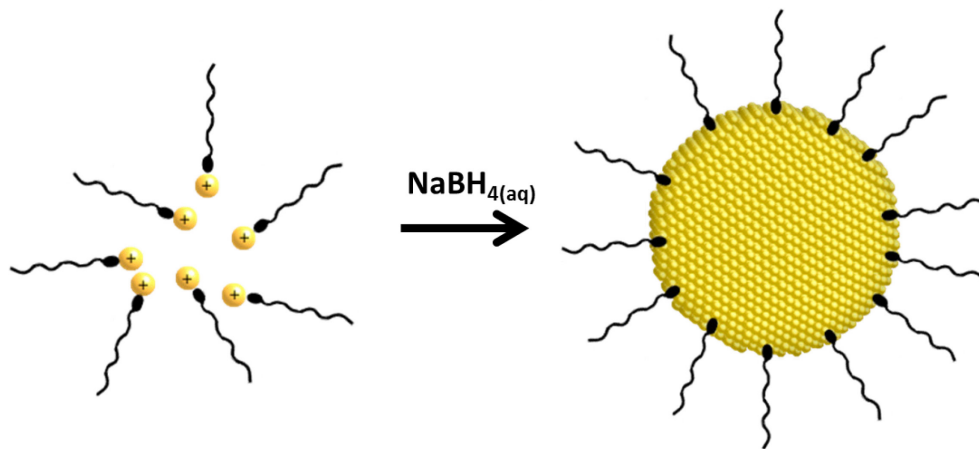


Figure 1-2. Brust-Schiffrin synthesis. (alkanethiol ligand are black and Au atoms are yellow)

1.3 Properties

1.3.1 Optical Properties

When Au is structured on the nanoscale, quantum confinement of electrons can lead to what is known as a localized surface plasmon resonance (SPR). The collective oscillations of conductive electrons on the Au nanostructure (*i.e.* Au 6s electrons) give rise to SPR bands, resulting in an absorption peak whose wavelength is dependent on nanostructure size, shape, and composition (~520 nm for Au NPs).²¹ The electronic properties of nanostructures change drastically with size and shape, due to quantum confinement effects.²² As the core size of a Au NP decreases, the intensity of the SPR band decreases in intensity. When the Au NP is smaller than ~2 nm molecular-like orbitals dominate (covered in section 1.3.2), causing the SPR to disappear and a weak photoluminescence can occur via interband transitions.^{23,24} Optical properties are heavily tied to the electronic properties of these systems.

1.3.2 Electronic Properties

Though the energy-level structure of larger Au NPs (~ 2-100 nm) can be considered quasi-continuous under most conditions, that of smaller Au NPs cannot. Unlike the continuous band structure of bulk metal systems and larger Au NPs (energy level differences are less than thermal energy, $k_B T$), very small NPs (< ~2 nm) exhibit discrete energy levels (energy level differences are greater than thermal energy).²⁵ These quantum size effects can be determined by using free electron theory to calculate energy level spacing (δ):

$$\delta \approx \frac{E_F}{N} \quad (1.1)$$

where E_F is the Fermi energy of Au and N is the number of gold atoms in the NP (assuming a spherical model).²⁶

The molecule-like character originating from these discrete energy levels, along with the metal-like character due to the existence of metallic bonds, give rise to both molecular orbitals and metallic bonding electronic character in small Au NPs (Figure 1-3).^{21,26} As such, synthetic control over any of these properties can be utilized to tailor the properties of metal NPs for specific applications.

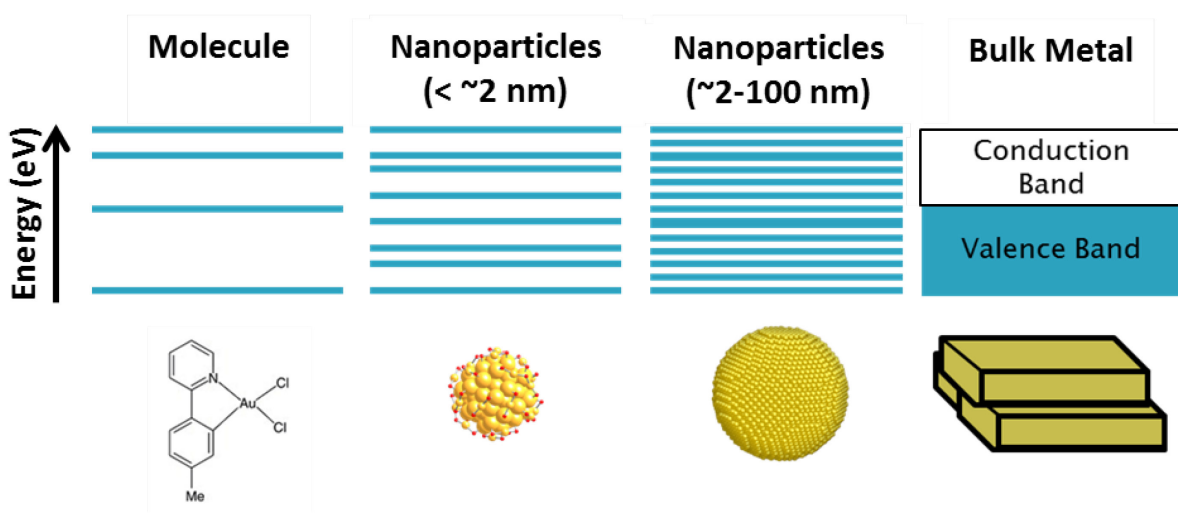


Figure 1-3. Schematic of energy level quantization in molecular Au,²⁷ small Au nanoparticles,²⁸ large Au nanoparticles, and bulk metallic Au.

Long-range, “aurophilic” Au-Au bonding, is a significant electronic effect which contributes to the stability and structure of Au NP surfaces.^{29–32} Aurophilic bonding is stronger than the metallophilic bonding of its congeners, meaning that structure and bonding in Au NPs is unique when compared to other metallic NPs. While metallophilic interactions exist for lighter coinage metals like silver and copper (argentophilicity and numismophilicity,

respectively),³³ as well as heavier species such as platinum, mercury, and thallium,²⁹ the energies involved with Au-Au interactions in particular are much greater. The increased bond energies of aurophilic interactions (7-12 kcal/mol) is due to the relativistic effects of Au.^{29,34} This places the strength of the aurophilic interactions below that covalent bonding (98 kcal/mol for C-H), yet greater than van der Waal forces (5 kcal/mol for H-O...H-O).³⁵ Schmidbaur proposes the aggregation of gold atoms is due to the interaction of closed-shell $5d^{10} Au^+$ species.²⁹ The $5d^{10}$ - $5d^{10}$ interaction comes from the mixing of $6s^2$ states^{34,36} in combination with the reduction of the energy gap due to relativistic effects.^{37,38}

The relativistic effect can be described by an apparent increase in electron mass (~20%) near the nucleus of the gold atom, due to the large positive nuclear charge,³⁷⁻³⁹ as well as lanthanide contraction, the name given to the contraction of the atomic radius due to the poor shielding effect of the f-orbitals.^{37,38} This contraction leads to Au having a decreased atomic radius, slightly smaller than that of Ag, and an increase in interaction due to the proximity of 6s electrons to the valence shell.^{37,38} Aurophilicity has therefore been determined to significantly influence organization in systems containing Au-Au interactions, such as nanoscale Au systems.

Furthermore, the relativistic effect in Au creates new bonding opportunities, such as Au-thiolate bonding, known to be favourable in attaching various thiol-terminated ligands to Au NPs.²¹ The Au-S bonding is due to an electronic donation/back-donation mechanism. Au and S bond through the hybridized 5d and 6s orbitals of Au with sulfur sp^3 -hybridized orbitals.⁴⁰ This in turn, leads to back-donation from the sulfur 3p orbitals to the unfilled Au 6p orbitals.⁴⁰ This Au-S bonding mechanism is responsible for the high-stability present in

small Au NP systems (e.g. Au₂₅, Au₁₀₂), but has also been shown to govern the surface structure of Au-thiolate self-assembled monolayers.⁴¹

1.3.3 Chemical Properties

One of the main reasons why Au NPs are of such interest is due to the abnormally large surface area when compared with their bulk counterparts, playing a large role in the chemical properties of Au NPs. When the size of Au NPs decreases, the surface-to-volume ratio increases.²¹ Therefore, Au NPs are more reactive than their bulk counterparts. To take this one step further, small Au NPs ($\sim <2$ nm) are significantly more reactive (with surface-to-bulk ratios nearing 1:1), and single-atom Au salts are even more reactive due to their increased oxidation state.⁴² By using the same quantity of Au, but changing the size of the NPs, reactivity can be tuned.

Another interesting property of Au NPs is their strong affinity for Au-S bonding. While the Au-S bond is covalent, ligand length and steric effects enable substitution of different thiol ligands. Some experiments have even made use of this Au-thiolate bonding to tune the solubility of Au NPs in solution.⁴³ Changing the attached ligand can change the reactivity of the Au NP as well, affecting local structure and electronic properties.⁴⁴ Alloying Au NPs with other metals (e.g. Ag, Pd, Pt) can also have a substantial effect on their chemical properties.^{45,46} While larger homogenous alloyed Au NPs tend to share the reactivity of their composing elements, smaller Au NPs can exhibit changes in magnetic moment,^{47,48} stability,⁴⁹ and electronic character.^{50,51}

1.3.4 Unique Structure

In NP systems physical and chemical properties are linked, and it is difficult to discuss electronic and chemical properties without discussing structure. While the Brust synthesis (Figure 1-2) enabled more directed synthesis, and therefore more detailed Au NP studies, the directed synthesis of smaller Au NPs (< 2 nm) was not yet possible. In the past decade, modification of the Brust technique by a few research groups succeeded in synthesis of extremely small Au NPs.^{52,53} These Au NPs, consisting of an exact number of Au atoms, exhibited properties which varied wildly from larger Au NPs.^{54,55} Mass spectrometry experiments determined these Au NPs to consist of less than ~350 Au atoms, with only certain ratios of Au to ligand ($\text{Au}_x(\text{SR})_y$) being stable.⁵⁶⁻⁵⁹

Due to their small size and lack of long-range order, mass spectrometry (MS) and density functional theory (DFT) geometry calculations are the primary tools for structural and compositional determination of small Au NPs.^{22,60-63} Thus far, X-ray crystallography has determined the structure in only four “compositionally precise” Au NPs containing 102,²⁸ 25,^{52,64} 38,⁶⁵ and 36⁶⁶ Au atoms (listed by historical determination). These small Au NPs enabled research into Au nanostructure formation, organization, and electronic character. With the total structural determination of the $\text{Au}_{102}(\textit{p}\text{-mercaptobenzoic acid})_{44}$ NP (henceforth referred to as Au_{102} – Figure 1-4D)²⁸ and $[\text{Au}_{25}(\text{SCH}_2\text{CH}_2\text{Ph})_{18}]^-(\text{TOA}^+)$ NP (henceforth referred to as Au_{25} – Figure 1-4A) (TOA^+ = tetraoctylammonium cation),^{52,64} further electronic and structural characterization is now possible.

The most important discovery from the crystallographic data of Au_{25} and Au_{102} is the formation of a surface “staple-motif” $-(\text{Au-S-Au})-$. This discovery revealed the nature of surface bonding in small Au NPs, wherein the S atoms from the thiol-ligands are drawn into

the surface of the Au NP, forming bridged Au-S structures.^{52,65,67} High stability in these small Au NPs is due to both the 13-atom icosahedral core and the “staple-like” structures affixed to its surface (as in Au₂₅). More shells of Au can be added to the core, followed by the same “staple-like” surface functionalization (as in the Au₁₀₂).²⁸

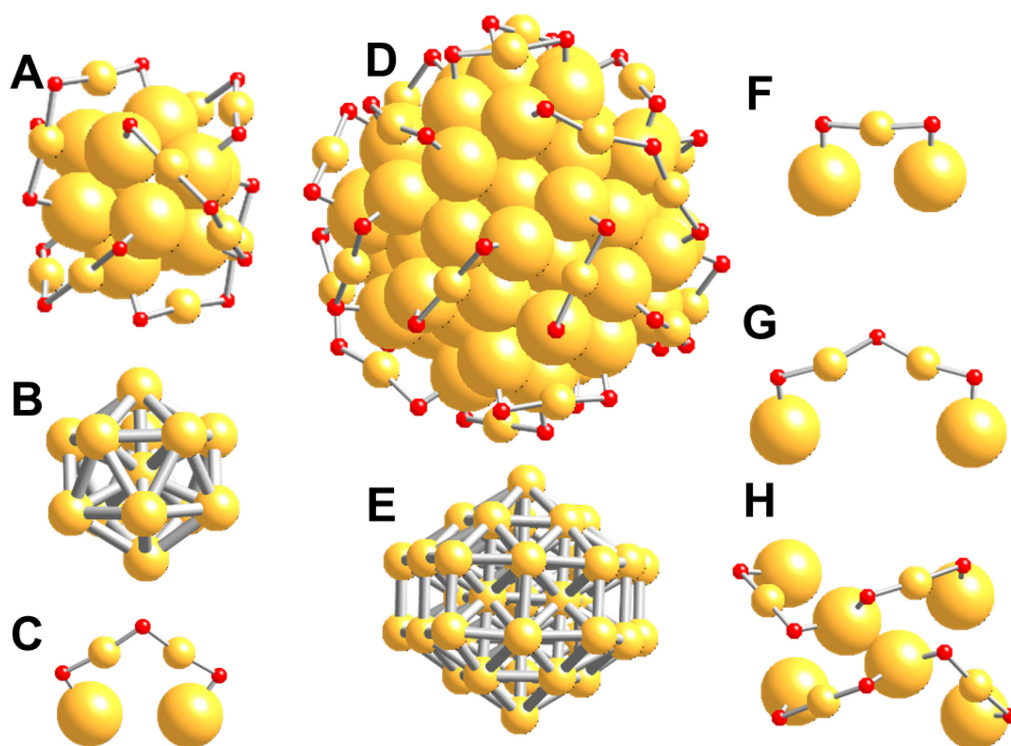


Figure 1-4. Diagram of Au₂₅ and Au₁₀₂. Components of A) Au₂₅ NP including B) icosahedral core and C) double-staple. Components of D) Au₁₀₂ NP including E) core, F) single-staple, G) double-staple, and H) double-anchor staple structures. Ligand molecules removed and size of Au atoms adjusted for visualization purposes. Au atoms are yellow, and S atoms are red.

By better understanding structure and bonding in small Au NPs through the use of Au₂₅ and Au₁₀₂ as model systems, it may be possible to determine better synthetic pathways,^{53,68,69} rationalize DFT calculations,^{70–72} interpret mass spectrometry findings,^{73–75} and better understand stability in these Au NPs.^{76,77} The synthesis of compositionally-precise

Au NPs and nanostructures has rapidly progressed in recent years, enabling the relatively high yield synthesis of neutral and anionic Au₂₅,^{53,69} Au₂₅ nanorods,⁷⁸ and many other Au and bimetallic nanostructures.^{49,79–81}

1.4 Potential Applications

The potential applications for Au NPs are numerous, therefore, due to the sheer volume of research and unique approaches for exploitation of their properties, only a few more pertinent examples will be discussed. Substrate-supported Au NPs may find application in orthopaedic implant studies due to their ability to functionalize implant surfaces,⁸² while smaller Au NPs have potential as catalysts and are used to study structure and electronic properties.^{83,84} This thesis will only present potential applications that are closely related to the NPs studied in this work (orthopaedics and catalysis).

1.4.1 Orthopaedic Applications

The unique properties exhibited by Au NPs find use in a variety of biomedical applications. The optical properties of functionalized Au NPs can change with a variety of ligands. Taking advantage of these properties for biodiagnostic applications enables the creation of sensitive tests, where changes to the Au surface or replacement/binding of the attached ligand would exhibit marked spectroscopic change.^{41,85} Likewise, Au NPs functionalized to target specific biomarkers *in vivo* are being studied for pathologically-specific imaging (*e.g.* biomarkers, cancer identification).^{86–88} The same targeted Au NP technique is being applied to other problems as well, such as drug delivery^{89–91} and

photothermal therapy,⁹² wherein Au NPs are functionalized, provide targets, or release drugs to specific *in vivo* locations.

The interaction of Au NPs with biological systems can be better understood through interaction studies of Au with model biomolecules, such as the study of Au NP and Au salt interactions with amino acids. The affinity of amino acids to Au ions has been determined through reduction and bonding studies.⁹³⁻⁹⁵ Reduction of Au salt by a peptide can occur via many electron-donating peptide residues, primarily those with polar or aromatic functional groups. When binding is considered, it is thiol groups which are the primary binding agent (though not the only binding agent).⁹³⁻⁹⁵ These studies support the strong Au-S bonding which occurs between Au and cysteine residues.

While Au nanostructures find use in a variety of applications,²¹ the reasoning for studying these systems in this thesis is based primarily on future biomedical use in orthopaedic implant functionalization. There is a strain on health-care systems with increasing demand for orthopaedic implant surgery, due in part to a younger age demographic requiring implants and a greater population requiring revision surgeries.^{96,97} If the need for revision surgeries, which are typically required every ~10 years, were to be reduced due to longer implant life-times, the result would be beneficial for the health-care system and patient alike. Modification of orthopaedic implant surfaces on the nanoscale can increase adhesion and osseointegration between bone and implant. Functionalizing an implant surface with Au NPs coated in bone morphogenetic protein could potentially stimulate bone growth and adhesion, increasing implant life-times and reducing revision surgeries.⁹⁸

There are a number of mechanisms available for the deposition of metal NPs onto substrate surfaces (*e.g.* electrochemical deposition,⁹⁹ radio-frequency sputtering,^{100,101} chemical vapour deposition,^{102,103} *etc.*). Electroless deposition (discussed in Section 2.1.2) was used due to the simplicity and reproducibility of Au NP coverage, and has been studied previously in the deposition of Pt onto Ti,¹⁰⁴ Au onto a Ge substrate,¹⁰⁵ and Au on Ti.¹⁰⁶ A drawback of electroless deposition, and substrate-supported NP-functionalization in general, is large NP size and polydispersity (50-200 nm).¹⁰⁴ Recently however, significant progress has been made in addressing both these issues, via physical and chemical surface modification.^{107,108}

Ti is of interest due to its biocompatibility, and therefore wide use as a substrate for orthopaedic implants.^{82,109,110} Au is ideal for both functionalizing Ti, and being functionalized with thiol-containing ligands, due to strong Au-S bonding.^{82,106,111–113} Au can also be considered biocompatible and binds strongly to Ti.^{82,106–108} Further functionalization of Ti and Au, such as described in Chapters 3 and 4, is advantageous as Au NPs may bond with beneficial biomolecules through exploitation of Au-thiolate bonding.

1.4.2 Catalysis

Catalytic reactions using Au NPs have been carried out in the past, but lack the reaction lifetimes and low cost of conventional catalysts.^{84,114} New research into understanding the structure and properties of small Au NPs may find application in catalysis.^{42,49,115,116} Au salts are known to be capable of activating O₂, H₂, as well as some carbon sp³, sp², and sp bonds,^{117,118} though it is still under debate whether Au(I) and Au(III) show the same activity, or whether Au(III) is reduced to Au(I) before reacting.^{119,120} In 1987,

Haruta et al. determined that nanoscale Au, contrary to its bulk counterpart, can catalyze reactions such as the hydrochlorination of acetylene and the oxidation of carbon monoxide at room temperature.¹²¹ This discovery is more conceptual than applicable, as catalysis of these reactions requires relatively high loadings of Au NPs, and suffers from poor turn-over numbers (TON, the number of reactions the Au NPs can catalyze per mole).

Due to little progress with improving the performance and cost of Au NPs, industrial applications of Au NP catalysts are not currently in use. Recently however, Oliver-Messeguer *et al.* discovered that extremely small Au NPs, consisting of only ~3-10 atoms, can achieve TON numbers of $\sim 10^7$ with frequencies of $\sim 10^5 \text{ h}^{-1}$, with the concentration of Au in the parts per billion range.¹¹⁵ While these values are for specific reactions, it has certainly renewed interest in Au NPs for industrial catalytic applications.¹²²

Bimetallic NPs are often used for catalysis. Consisting of two different metallic elements, their structural and electronic properties are often quite different than those of the pure elements of which they are composed.^{2,123} The variation of composition and NP size can alter the melting point, structure, and magnetic properties, as well as the catalytic reactivity of the NPs.^{2,123} The organization of bimetallic NPs is also very important, as homogeneous, core@shell, patterned, and cluster-in-cluster organizations can all have drastically different properties.^{2,124-126}

A better understanding of structure and electronic properties in small Au NP samples could aid in determining catalytic pathways and optimization. Furthermore, small changes in the bimetallic composition of these small Au NPs could have significant catalytic benefits. However, in order to study these structural and electronic properties, an appreciation for the difficulty in characterization is required.

1.5 Challenges in Synthesis and Characterization

There are many challenges to the synthesis, characterization, and utilization of Au nanoparticle systems. However, in the context of these structure and bonding studies, the discussion will be limited solely to challenges involving the synthesis of Au-thiolate NPs, as well as the challenges involved with studying Au-S bonding in such systems.

1.5.1 Synthetic Challenges

Monodisperse thiolate-stabilized Au NPs are difficult to synthesize in large quantity, the process typically requiring significant purification of the product to isolate a particular NP size and structure. There are a few Au NPs with enhanced stability, due to ligand-ligand interaction and high-symmetry due to staple-like structures (*e.g.* Au₂₅). These highly stable Au NPs are sometimes called “magic number” NPs, as synthesis of less-stable Au NPs often results in the formation of these stable organizations. During the synthesis of Au NPs, it is possible to force NP formation towards a product based on one of these more stable arrangements. It is through the exploitation of this stability that the Au₂₅,⁵² Au₃₆,⁶⁶ Au₃₈,⁶⁵ and Au₁₀₂²⁸ NP systems were produced. However, it is difficult to scale this synthesis to larger compositionally-precise Au NPs (larger than ~350 Au atoms).

Another problem is obtaining a high purity of the product, which is difficult to achieve while the mechanism for small Au NPs formation has yet to be fully elucidated. These difficulties make obtaining a single crystal structure difficult, due to both the challenges in obtaining a high-purity sample in enough quantity for X-ray structural determination. Furthermore, purification methods such as that used by the Jin Group can only be used for solution-phase products, and are therefore not applicable to supported systems.⁵³

In addition to the widely studied solution-phase Au NPs, another important category of Au nanostructures is substrate-supported Au NPs. Functionalization of substrate surface with Au NPs is important for many technological applications, when function immobilized NPs are needed. When compared to solution-based syntheses, substrate-supported metal NP systems are largely under-developed. As such, reproducing the monodispersity, size, shape, and composition of metal NPs on a substrate remains a significant challenge. The use of electroless deposition for the functionalization of a substrate with Au NPs (section 2.1.2), when coupled with a thiol ligand, can provide more flexibility in the surface and size control of Au NPs, minimizing polydispersity in Au NPs.^{106,107} The research presented in this thesis may provide a promising synthetic strategy for the production of higher quality substrate-supported Au NPs.

1.5.2 Challenges in Characterization

Characterization of thiolated Au NPs can be difficult, and sometimes conventional methods are difficult to employ. One main challenge in directly probing Au-S interactions in Au-thiolate nanostructures is that both S and Au are considered spectroscopically silent. The chemical shift of Au can be analyzed using ¹⁹⁷Au Mossbauer spectroscopy,¹²⁷ but this requires a large sample size, and is outside the realm of what is possible for these studies. As the predominant isotope ³²S lacks nuclear spin, NMR cannot be used to study these systems.¹²⁸ While ³³S have a spin of $I = 3/2$, the 0.76% abundance means that low coordinate systems (*e.g.* thiols) are difficult to observe without isotope enrichment.¹²⁸

The most frequently used characterization tools for Au NPs are electron and scanning probe microscopies. However, when the NP sizes are very small (~1 nm), it becomes

difficult to resolve the atomic structure with sufficient accuracy, and beam damage is often problematic. X-ray diffraction, commonly used for larger NP studies, has difficulty in characterizing small or dilute NP systems due to a lack of long-range order.

X-ray spectroscopy enables element-specific probing of Au and S in these samples, providing information on the local environment, oxidation state, and chemical speciation without the need for long-range order (*e.g.* amorphous materials, solution samples).^{129–131} Furthermore, pairing X-ray studies with *ab initio* calculations provides more insight into the electronic character of Au nanostructures. In addition, special X-ray spectroscopy techniques such as a glancing angle setup, spinning sample holder, and cryogenic cooling can be used to increase the signal-to-noise ratio, increase sampling area, reduce radiation damage, and ensure isotropy in Au NP samples.

1.6 Overview of Thesis

1.6.1 Thesis Motivation

To take advantage of structure and bonding in Au-thiolate nanostructures, a better understanding of structure-property relationships is required. By studying small changes to Au NP systems from both a ligand and metal perspective, it is possible to gain insight into the structural and electronic properties of these systems. Au NP systems can greatly benefit biomedical and catalytic applications (to name a few), and exploitation of their properties may be possible with a greater understanding of their structure and bonding.

By varying the ligand size and concentration, the effects of ligand on the structure and properties of substrate-supported Au NPs can be elucidated. This information provides

insight into the interaction of ligand and Au NPs and their effect on surface modification. By supporting Au NPs, the mechanism of NP formation is studied under the context of biocompatible materials (*i.e.* orthopaedic implants).

Further study of structure and bonding in Au-thiolate NPs was carried out from the metal perspective. The effect of Au NP size and composition can provide insight into the electronic and structural properties of Au NP bonding. By varying the effect of size on a constant surface feature (double staple), electronic structure-properties can explain surface functionalities. Alternately, by changing the composition of the Au NP while maintaining its structure, the effect of small chemical change can be studied in regards to the electronic properties of the Au NP.

Therefore, by studying the structure-property relationships of Au NPs from both a ligand and metallic perspective, it is possible to better understand the nature of structure and bonding in thiolate-coated Au nanostructures.

1.6.2 Structure of Thesis

Following the background presented in Chapter 1, Chapter 2 contains all necessary information pertaining to the experimental methodology and theory required for the following studies. Synthesis of both the solution-based and substrate-based Au NPs is covered in Section 2.1. All samples characterized in this thesis were produced using these methods, including those which make use of the biomolecules discussed in Section 2.2. An in-depth discussion of scanning electron microscopy (SEM) and all Synchrotron-based X-ray spectroscopies is found in Section 2.3. This section discusses both the experimental

techniques which make use of these characterization methods, and the theory necessary to understand the resultant structural and chemical information. Section 2.4 covers the computational programs and methods used to describe and calculate the structure-property relationships discussed within the thesis.

Comparison of Au NPs functionalized by large and small biomolecule ligands (Chapter 3) is studied with regard to ligand size effect on the formation of Au NPs and their subsequent deposition onto a Ti substrate (Section 3.1). The exact synthesis of Au NPs coated with large and small biomolecules, as well as their subsequent deposition onto Ti is discussed in Section 3.2.1. The SEM and X-ray spectroscopy techniques and methods used for the characterization of these samples is covered by Section 3.2.2. Section 3.3 describes and discusses the experimental data regarding the formation, structure, and chemical nature of these Au NPs, as well as similar Ag and Pd NP systems. This data is followed by a summary of pertinent results in Section 3.4.

Chapter 4 is the comparison of Au NPs functionalized by two biomolecule ligands of varying concentrations, where one ligand is only slightly larger than the other (Section 4.1). Section 4.2 explains the synthetic procedures (Section 4.2.1) and characterization techniques (Section 4.2.2) necessary for the study of these substrate-supported systems. In Section 4.3, the results of these ligand size and concentration studies are described. Section 4.4 summarizes the importance of this study and the result of its deviations from the systems of Chapter 3.

Chapter 5 studies the structure and bonding in Au NPs from a metal perspective, examining the similar double-staple structures in two compositionally-precise small Au NPs (Section 5.1). Using X-Ray crystallographic structural information, the surface staple

environments of Au₂₅ and Au₁₀₂ NPs were compared using *ab initio* calculations (Section 5.2). The local structural environment (Section 5.3.1) and electronic character (Section 5.3.2) of the double staple structure were investigated for each Au NP sample. A summary of the findings is presented in Section 5.4.

The final study (Chapter 6) covers the metallic perspective of monoatomic Pt-doping on the structure of the Au₂₅ NP (Section 6.1). The synthesis of Au₂₅ and Au₂₄Pt (6.2.1), as well as their X-ray spectroscopy (Section 6.2.2) and computational (Section 6.2.3) characterizations are presented in Section 6.2. The results of these X-ray spectroscopic and computational studies are covered in Section 6.3, covering location (Section 6.3.1), structure (Section 6.3.2), and electronic properties effects (Section 6.3.3). A summary of these results is discussed in Section 6.4.

Chapter 7 discusses the impact of this research (Section 7.1). A brief description of possible future studies is presented in Section 7.2.

CHAPTER 2 METHODS

2.1 Synthesis

2.1.1 Solution-based Synthesis

Solution-based Au₂₅(SC₂H₄PH)₁₈ (SR = SC₂H₄PH) and Pt-doped Au₂₄Pt(SR)₁₈ Au NP samples were prepared, purified, and characterized using high-resolution MALDI-TOF mass spectrometry by Huifeng Qian from the Jin Research Group, Carnegie Mellon University, Pittsburgh, Pennsylvania.^{49,132}

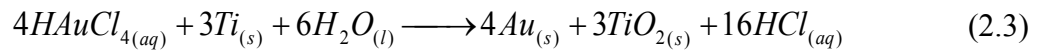
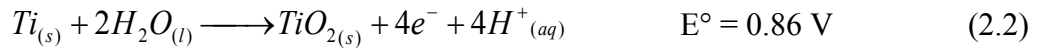
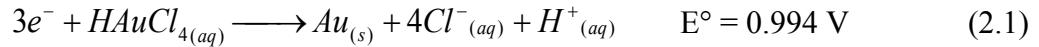
Au₂₅(SR)₁₈ was synthesized using a modified Brust method.¹³³ In this synthesis, 0.157 g of HAuCl₄·3H₂O (>99.99%, Aldrich) and 0.317 g of tetraoctylammonium bromide (TOABr, >98%, Fluka) were dissolved in 15 mL of tetrahydrofuran (THF, HPLC grade, Aldrich). The solution was stirred for 15 minutes, followed by the addition of 0.345 mL of phenylethanethiol (99%, Acros Organics). After ~30 min, 0.190 g of NaBH₄ (99.99%, Aldrich) in 6 mL of cold water was added and left to stir for another 5 h.^{53,134} The resulting product was washed in ethanol (absolute, 100%, Pharmco) and centrifuged repeatedly to remove excess ligand, yielding ~50% product.

The Au₂₄Pt(SR)₁₈ was synthesized using the same modified Brust method previously used for the Au₂₅ sample.¹³³ By addition of 0.0410 g of H₂PtCl₆·xH₂O (99.995%, Aldrich) to the Au₂₅ synthesis, a product containing both Au₂₅ and Au₂₄Pt was synthesized. After washing with ethanol and centrifugation, the product was then dried by rotary evaporator. After drying, the product was then redispersed in dichloromethane (DCM, HPLC grade, 99.9%) and 5 mL of 30% hydrogen peroxide (Fisher Scientific) was added to decompose the less-stable Au₂₅ product. The organic phase was then dried in a rotary evaporator, redispersed

in DCM, and centrifuged to separate the Au₂₅(SR)₁₈ and Au₂₄Pt(SR)₁₈ components from excess ligand and impurities. To further separate these products, size-exclusion chromatography (SEC) was employed using a PLgel column (particle size of 3 μm, 100 Å pore diameter) and DCM as the mobile phase. Mass spectrometric characterization was carried out using matrix-assisted laser-desorption ionization – time of flight (MALDI-TOF) measurements, identifying the Au₂₄Pt(SR)₁₈ elutant. The matrix used for MALDI in these experiments was Trans-2-[3-(4-tert-butylphenyl)-2-methyl-2-propenyldiene] malononitrile. Au₂₄Pt was synthesized as ~5% of the Au₂₅ product.

2.1.2 Substrate-based Synthesis

The deposition of Au NPs onto a Ti substrate was done using an electroless deposition technique. Benefits of the electroless deposition technique are low cost, and reproducibility of prepared samples with relatively high surface coverage and simple lab setup. The deposition occurs due to the differing reduction potentials between titanium and gold.¹⁰⁶ It is proposed that the corresponding redox reaction processes and potentials (E°) are as follows:



It is also hypothesized that the formation of TiO_2 prevents the reaction of $\text{HAuCl}_{4(\text{aq})}$ with $\text{Ti}_{(\text{s})}$, thereby preventing further gold nanoparticle formation and growth.¹⁰⁶ Although this technique has been used previously in the deposition of Ag onto Si_3N_4 ,¹³⁵ Au onto Ge, Cu and Zn,^{105,136} and Pt onto Ti,¹⁰⁴ it has recently been adapted for the deposition of Au onto Ti.^{106,107} Porter *et al.*¹⁰⁵ and Padmos *et al.*¹⁰⁶ determined that the concentration of metal salt used, the duration of Ti etching, and the duration of Ti immersion in metal salt/biomolecule model solution greatly affects the size and surface coverage of the deposited nanoparticles.

Ti discs (~1 cm diameter, ~1 mm thick) were produced using an industrial disc punch equipped with a sharpened Ti bit, at the Mechanical Engineering Department at Dalhousie University. A razor blade was used to mark the discs on one side, so as not to confuse the side to be analyzed (non-marked) with the opposing surface (marked). The Ti discs were cleaned first by sonication in acetone for five minutes, then by sonication for a further five minutes in ethanol, and then sonication again for another five minutes in de-ionized water (18 M Ω). The discs were then placed onto a Teflon ring at the bottom of a 50 mL beaker (see Figure 2-1A). A Teflon stir-bar was placed into the centre of the Teflon ring, and the apparatus was set atop a magnetic stir-plate.

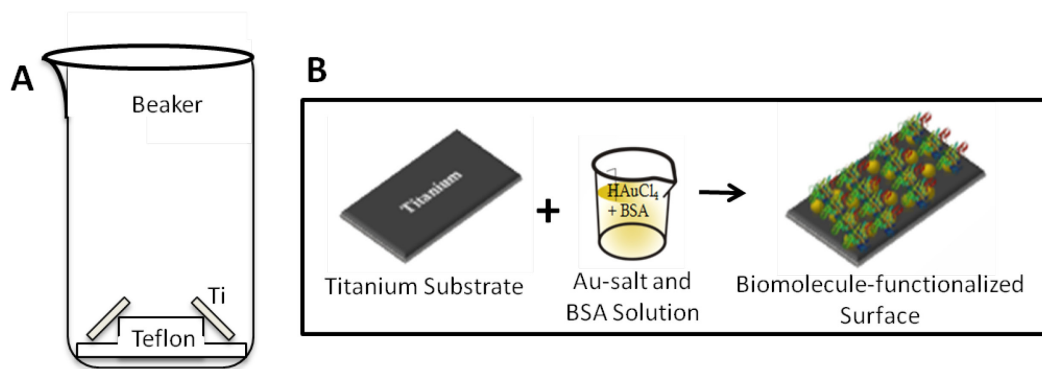
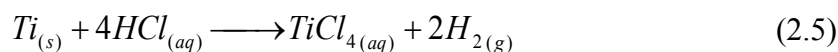
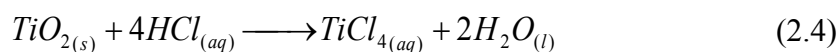


Figure 2-1. Experimental setup for one-step procedure. A) Beaker with Ti substrate and Teflon ring, and B) graphical procedure for deposition of BSA onto Au NP-functionalized Ti surface.

Once the Ti surface was cleaned, 10 mL of concentrated hydrochloric acid (HCl) was added to the beaker, completely submerging the substrate so as to etch the Ti disc, removing the surface oxide layer from the titanium.¹³⁷ A Parafilm[®] cover was placed over the beaker, and the magnetic stirrer was then carefully started so as not to disturb the Ti discs. The solution was left to etch for ~1 h (Figure 2-2). Ti etching was completed when H₂ bubbles reappear on the surface of the Ti within five seconds of being removed by carefully bumping the beaker. The formation of H₂ upon completion of the etching step can be explained by the reaction of TiO₂ and Ti with HCl:



While there are other side reactions and products formed in the reaction of TiO_{2(s)}, Ti_(s) and HCl_(aq),¹³⁸ studies have shown that most oxides and complexes formed in this

reaction will desorb from the surface, allowing fresh $\text{TiO}_{2(s)}$ to react.¹³⁸⁻¹⁴⁰ Etching for an extended period of time results in the removal of too much Ti, leading to a pitted and rough titanium surface (Figure 2-2). The unusual features in Figure 2-2A are not due to AuNPs, but to roughened Ti or TiO_x structures.

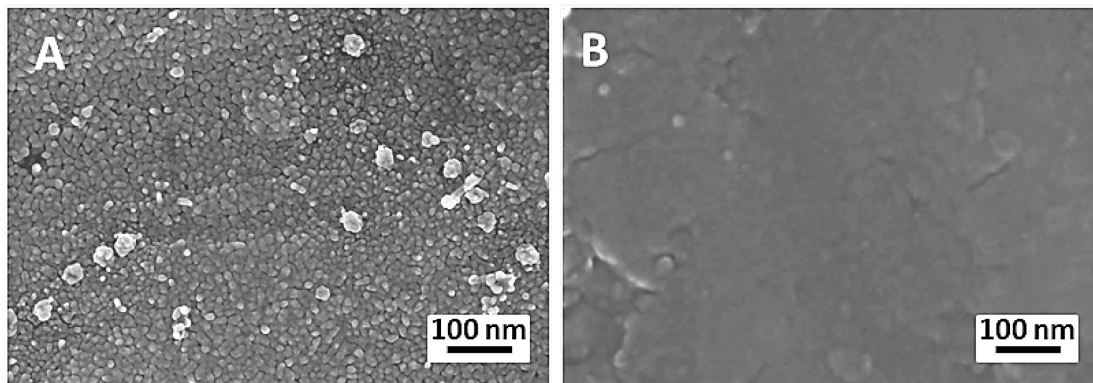


Figure 2-2. SEM micrographs of bare surfaces which have been etched for A) too long (~2 h) and B) an appropriate length of time (~1 h).

This method provides consistent and reproducible etching, as supported by scanning electron microscopy (SEM) imaging, and previous work.^{106,107} The titanium is quickly removed from the hydrochloric acid solution, rinsed briefly with deionized water, and placed into a 10 mL solution of Au salt and a biomolecule ligand in varying concentration (1/2, 1/5, 1/10, and 1/20 equivalents of biomolecule to Au salt). After two minutes the titanium was removed from the Au-salt/biomolecule solution and rinsed again in deionized water to remove any excess material from the system, before being dried under a flow of nitrogen or argon.

2.2 Model Biomolecules

The biomolecule ligands used in Section 2.1.2 were selected based on their solubility in aqueous solution, and their history in Au NP systems (Table 2-1).

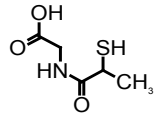
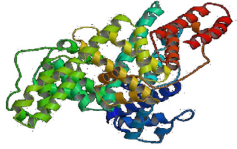
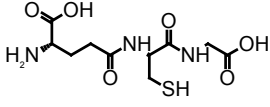
Biomolecule	Structure
Mercaptopropionyl Glycine (MPG)	 <chem>CC(S)C(=O)NCC(=O)O</chem>
Bovine Serum Albumin (BSA)	
Glutathione (GSH)	 <chem>NC(CCC(=O)NCC(S)C(=O)O)C(=O)O</chem>

Table 2-1. Model biomolecules and their structure.

2.2.1 N-(2-mercapto-propionyl) glycine (MPG)

N-(2-mercapto-propionyl) glycine (MPG), also known as tiopronin, contains a thiol group capable of Au-S bonding. It is useful in the treatment of cystinuria, wherein it is used to control cysteine precipitation which can lead to cysteine stones in the bladder and kidneys.¹⁴¹ It is also prescribed to treat Wilson's disease, a build-up of Cu in the body, by chelating the Cu and aiding in its excretion through urine.¹⁴² MPG has been used previously in the deposition of Au on Ti,¹⁰⁷ as well as in a multitude of solution-based Au NPs.^{143–145}

2.2.2 Bovine serum albumin (BSA)

Bovine serum albumin (BSA), also known as Cohn Fraction V, is a relatively bulky protein (64kDa), with a high number of inward-facing thiol groups, and has been crystallized in a number of different orientations.¹⁴⁶ Of the 35 S atoms in the BSA protein, 34 form disulfide bridges, leaving only one free thiol group.¹⁴⁷ BSA has also been used in a variety of NP systems,^{107,146,148,149} and has been used as a model biomolecule for *in vitro* studies.^{150,151}

2.2.3 Glutathione (GSH)

Glutathione is a tri-peptide slightly larger in size than MPG (14.4 Å vs. 7.8 Å, respectively).¹⁵² Glutathione can be created *in vivo* as an antioxidant and is reduced to form GSH. The oxidized dimeric form (GSSG) is created through formation of a disulfide bridge.¹⁵² Due to its being produced *in vivo*, GSH is used in a number of nanoparticle synthesis studies as a model biomolecule.^{58,151,153,154}

2.3 Characterization Techniques

2.3.1 Scanning Electron Microscopy (SEM)

Scanning electron microscopy (SEM) micrographs were acquired for all Ti-supported Au NP samples. SEM characterization experiments were conducted using a Hitachi S-4700 SEM located at the Institute for Research and Materials Facility for Materials Characterization in the Department of Mining and Metallurgical Engineering at Dalhousie University.

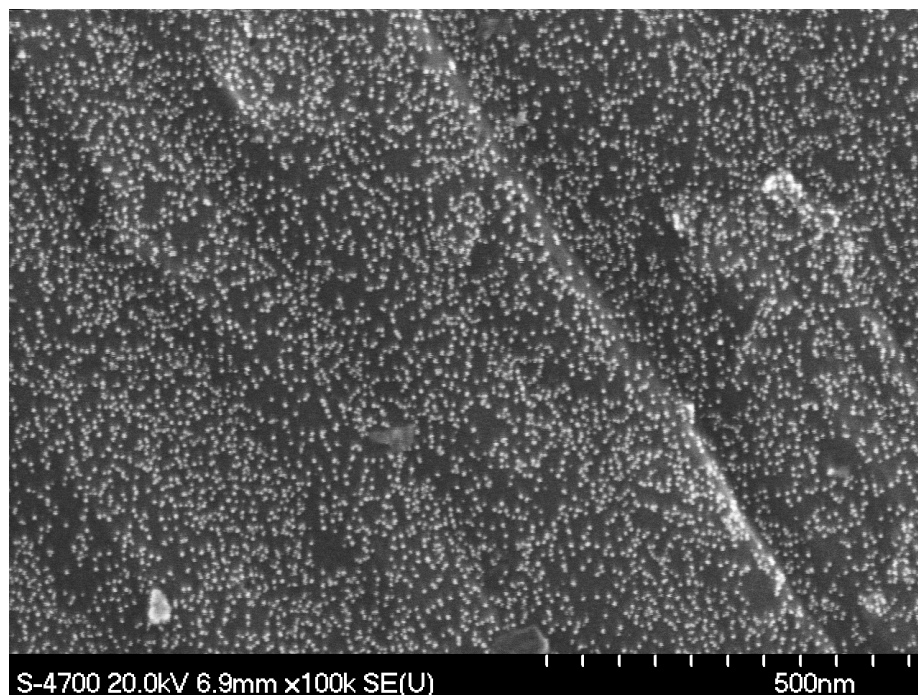


Figure 2-3. SEM micrograph of 20:1 Au:BSA biomolecule-functionalized Au nanoparticles supported on Ti (100,000x magnification at an accelerating voltage of 20 kV).

Samples were typically imaged at 18,000x – 300,000x magnification with an accelerating voltage of 20 kV, an emission current of 10-15 μA , and a working distance of 6-7 mm. Samples were either affixed to an aluminum sample holder using double-sided copper or carbon tape, or mounted into a custom-made aluminum sample holder.¹⁰⁶

The public-domain software ImageJ, modified by McMaster University's Bio-Photonics program, was used for the measurement of nanoparticle size and coverage. Good coverage and high-contrast images are required to achieve good sample sizes for statistical analysis.

2.3.2 Synchrotron Radiation

Synchrotron radiation is generated when relativistic electrons are accelerated (undergoing directional change), resulting in the emission of a narrow cone of photons, the size of which is dependent on the magnitude and frequency of electron acceleration.¹⁵⁵

A typical diagram of a synchrotron facility is shown in Figure 2-4, wherein a linear accelerator produces a large quantity of high-energy electrons which are then further accelerated in a booster ring, and maintained at the desired energy in the storage ring.¹⁵⁵ Beamlines are located at each bending magnet and are the experimental stations where synchrotron radiation is monochromated, focused, and used to acquire data.¹⁵⁵ The storage ring consists of bending magnets to alter the path of the electrons, as well as multiple straight sections.¹⁵⁵ Due to the large quantity of tightly packed electrons within the storage ring, the light produced by acceleration at each bending magnet is extremely bright and collimated, with the spot size being up to several millimetres in diameter.¹⁵⁵ Insertion devices (including wigglers and undulators) are many-magnet assemblies placed in the straight sections between bending magnets, used to create photon beams that are more collimated and exponentially brighter than bending magnet sources.¹⁵⁵

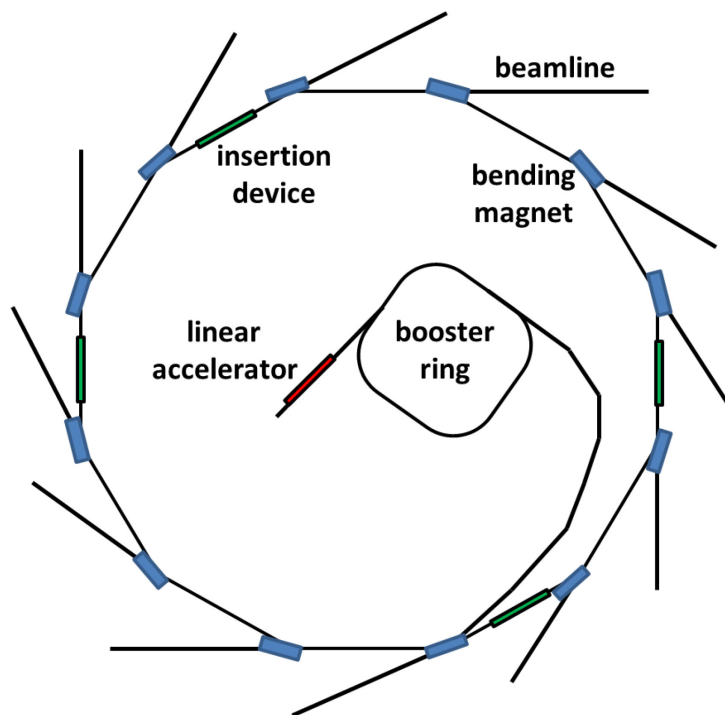


Figure 2-4. General diagram of a synchrotron radiation facility.

The synchrotron radiation facilities used for this research were the Canadian Light Source (CLS), located on the University of Saskatchewan campus in Saskatoon, Saskatchewan, and the Advanced Photon Source (APS), located at Argonne National Labs in Argonne, IL. Beamlines used for data acquisition were:

- the CLS Spherical Grating Monochromator (SGM / 11ID-1) undulator beamline for XPS experiments,¹⁵⁶
- the CLS Soft X-Ray Microcharacterization (SXRMB / 06B1-1) bending-magnet beamline for X-ray absorption near-edge structure (XANES) experiments,¹⁵⁷
- the CLS Hard X-ray MicroAnalysis (HXMA / 06ID-1) wiggler beamline for XANES and EXAFS experiments,¹⁵⁸

- the APS Pacific-Northwest Consortium/X-ray Science Division (PNC/XSD / Sector 20) bending-magnet beamline for XANES and EXAFS experiments.¹⁵⁹

XANES and EXAFS measurements require continuously varying incident photon energies, and XPS requires an ultra-high vacuum environment. These necessities, along with the very high sensitivity needed to study the following samples, make synchrotron radiation facilities a requirement for this research project.

2.3.3 X-Ray Photoelectron Spectroscopy (XPS)

X-ray photoelectron spectroscopy (XPS) operates via the excitation of an electron from a core-level atomic orbital into the continuum using monochromated X-rays.^{129,160,161} Electron emission can be explained as the addition of energy from ionizing radiation and subsequent formation of an ion/photoelectron pair:



where $h\nu$ is the incident photon energy, M an atom, M^+ an atomic ion, and e^- is the photoelectron. The term “photoelectron” denotes an electron which has been emitted via excitation by a photon source. The energy required to eject a core-level electron (*i.e.* binding energy, E_B) is described by the equation:

$$E_B = h\nu - E_K - \phi \quad (2.8)$$

where E_K is the kinetic energy of the electron, and ϕ is the workfunction, representing the energy required to remove an electron from the Fermi level vacuum levels.^{131,160} Figure 2-5 denotes the difference between an electron being emitted from a system (XPS), and an electron being excited into unoccupied orbitals. As no two core-electrons have the same binding energy (elemental specificity), XPS spectroscopy is sensitive to changes in the oxidation state and electronegativity of nearby atoms.^{129,160,161} For this reason, XPS is an ideal tool to probe Au-S bonding of Au NPs and their capping ligands, and Au-metal bonding in Au NPs.

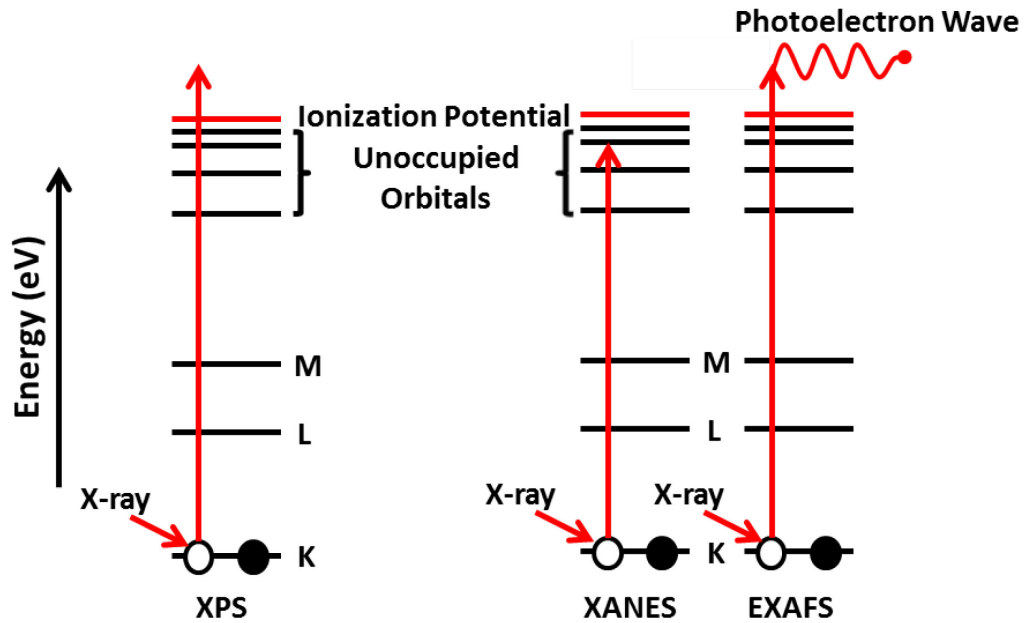


Figure 2-5. Diagram depicting typical mechanisms for X-ray photoemission (XPS) and X-ray absorption (XANES and EXAFS). The orbitals are identified under traditional core-level transition nomenclature (e.g. K = 1s, L = 2s, 2p).

2.3.4 X-Ray Absorption Spectroscopy (XAS)

X-ray absorption spectroscopy (XAS) measures the quantity of X-ray absorption by a sample as a function of incident photon energy.^{130,131,162} This, in turn, can tell us much about the local structure and electronic properties of the probed element without the common requirement of long-range order necessary for X-ray crystallography experiments (*e.g.* amorphous systems may be readily analyzed).^{131,162} Although there are many processes involved, XAS refers to spectroscopy experiments wherein the energy of an X-ray photon is absorbed by the sample, and the subsequent changes in that sample are measured.^{129,130,160} XAS is particularly useful for samples which require element-specific study, as the high energies of the incident X-rays excite core electrons, which are element specific. It is for this reason that XAS is used for the Au and S in the nanoparticle systems studied herein.

When a core-level electron is excited by an X-ray photon with an energy equal to or greater than its binding energy, it is either promoted to an unoccupied atomic or molecular orbital, or into the continuum (Figure 2-5).^{129-131,160} These two processes can be used to divide the XAS spectrum down into two distinct regions, generally referred to as the near-edge and post-edge regions (Figure 2-6).^{130,155} While “edge” refers to the X-ray absorption edge, the near-edge region consists of any features arising due to the excitation of core-level electrons into unoccupied atomic (or molecular) orbitals.¹³¹ Spectral features present in the pre-edge and edge regions of the XAS spectrum are referred to as X-ray absorption near-edge structure (XANES).¹³¹ XANES is discussed further in section 2.3.5.

The absorption edge is the point at which an electron is photo-ejected from the system with a kinetic energy of 0 eV (also referred to as the “white line” for historic reasons), and is equivalent to the core-level electron binding energy.¹²⁹⁻¹³¹ Due to unique electron

binding energies for all elements, absorption edges are an element-specific source of information.^{129–131,160} The degree of photon absorption by the sample is referred to as the X-ray absorption coefficient, $\mu(E)$, and can be described as a function of incident photon energy in fluorescence measurements by the equation:

$$\mu(E) = \frac{I}{I_0} \quad (2.9)$$

where I_0 and I are the intensities of the incident photon beam before and after passing through a sample. Oscillating features in the post-edge region, also referred to as the extended region, are due to constructive and destructive interference of outgoing and back-scattered photoelectron waves.¹³⁰ As such, extended X-ray absorption fine-structure (EXAFS) spectroscopy analyses these oscillations and yields information regarding atoms in the area surrounding the element of interest. A more in-depth discussion of EXAFS is presented in section 2.3.6.

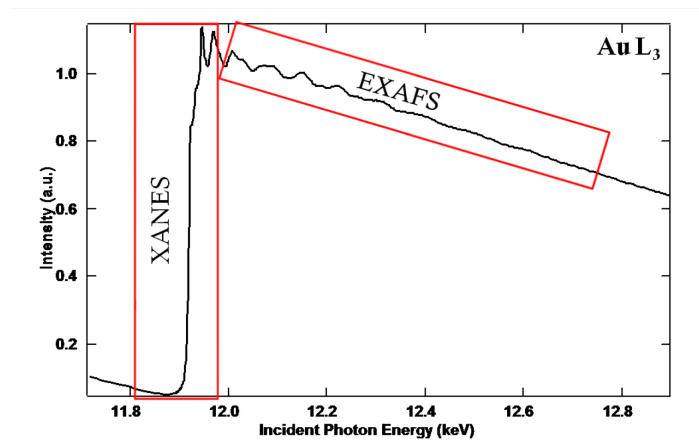


Figure 2-6. Au L₃-Edge (2p_{3/2}) XAS spectrum showing near-edge (XANES), and extended post-edge (EXAFS) regions.

2.3.5 X-Ray Absorption Near-Edge Structure (XANES) Spectroscopy

X-ray absorption near-edge structure (XANES) spectra are absorption features occurring in the region between ~ 30 eV before above the X-ray absorption edge.¹³¹ XANES spectroscopy records the relative number of electrons excited from a core-level orbital into unoccupied atomic (or molecular) orbitals as a function of change in the incident photon energy.¹³¹ Near-edge X-ray absorption fine-structure (NEXAFS) is commonly used when describing the same spectroscopic technique as XANES, but it is usually reserved for experiments conducted with energies below ~ 2500 eV (*i.e.* sulfur K-edge and below). NEXAFS is therefore commonly used to describe experiments involving lighter elements, including organic samples.¹³¹

When atoms interact with one another, the electron withdrawing or donating nature of atoms attached to the probed element can have an effect on the binding energies of core-level electrons, as can bonding and conformational changes within the sample.¹³¹ These changes in binding energy can create fine-structure in the XANES region, making XANES chemically sensitive in this regard. The more electronegative (and therefore electron withdrawing) the attached atoms are, the greater the incident photon energy that is required to overcome the binding energy of the core-level electron.¹³¹ To use the sulfur K-edge NEXAFS of common functional groups as an example, electron binding energies would be ordered by increasing electronegativity (*e.g.* thiol < sulfoxide < sulfate).¹²⁸

XANES spectra can be acquired in many ways, the more popular methods for lower X-ray energies being the total electron yield (TEY) and fluorescence yield (FLY) detection techniques.^{130,131} As stated previously, there are many processes which accompany X-ray ionization of atoms. As a sample is ionized, it loses electrons to the continuum.^{129–131,160} The

TEY technique simply measures the drain current required to replenish the electrical charge in the sample. It is therefore important that the sample undergoing irradiation be conductive.^{131,155} While the multiple processes contributing to electron loss can be convoluted in elements with many electrons (high-Z elements), photoemission and Auger processes dominate in the lower-Z range.^{131,155} An added benefit of TEY measurements is that since they are photon-in/electron-out processes, they are surface sensitive due to mean-free path energy-loss limitations.^{131,161} This surface sensitivity makes TEY an ideal tool for use in surface science. Fluorescence is a photon-in/photon-out effect,^{130,131} meaning that FLY detection does not have the same mean-free path length constraints that electron-measuring techniques do.^{130,131,155} Although it remains a useful technique, the benefit of a less-convoluted fluorescence spectrum is diminished by the poor fluorescence signal of low-Z elements and the loss of surface sensitivity.^{130,131,155}

2.3.6 Extended X-Ray Absorption Fine-Structure (EXAFS) Spectroscopy

Extended X-ray absorption fine-structure (EXAFS) results from the interference of outgoing and incoming photoelectron waves, and is responsible for much of the structural information extracted from XAS experiments.^{130,162} When photoelectrons are ejected into the continuum (Figure 2-7, solid lines), they backscatter from the electron density of neighbouring atoms, creating backscattered photoelectron waves (Figure 2-7, dashed lines) whose phase and amplitude are functions of the atomic number of the scattering atom and the energy of the incident photon.¹³⁰

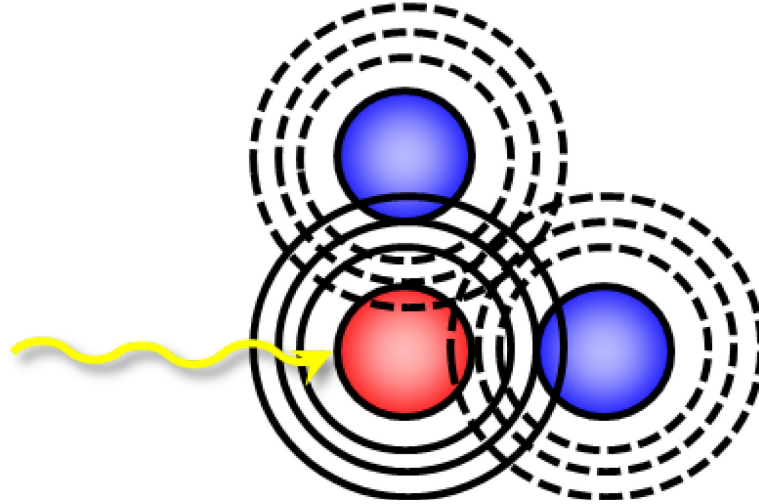


Figure 2-7. Incident photon (yellow) exciting photoelectron wave from an atom (red) and interference caused by neighbouring atoms (blue).

Constructive and destructive interference amongst backscattered photoelectron waves appears create oscillations in the extended (post-edge) region of the X-ray absorption spectrum.^{130,162} Fine-structure, χ , can be obtained using:

$$\chi(E) = \frac{\mu(E) - \mu_0(E)}{\Delta\mu_0(E)} \quad (2.10)$$

where the difference between the X-ray absorption coefficient (μ) and a background function (μ_0), divided by the absorption edge intensity ($\Delta\mu_0$). A typical EXAFS spectrum is a superposition of all scattering paths, whose fine-structure is described by:

$$\chi(k) = S_0^2 \sum_i \frac{N_j e^{-ik^2 \sigma_j^2} e^{-\frac{2R_j}{\lambda(k)}} f_j(k)}{k R_j^2} \sin(2kR_j + \delta_j(k)) \quad (2.11)$$

where, S_0^2 is the amplitude reduction factor (accounting for gradual loss of intensity in the X-ray absorption spectrum), N_j is the coordination number for a given shell (j), R is the bond distance, σ^2 is the root mean-squared displacement, $f(k)$ is the amplitude of the scattering atom, $\delta(k)$ is the phase shift of the scattering atom, and k is the wavenumber of the exciting photon, given by:^{130,162}

$$k = \sqrt{\frac{2m(E-E_0)}{\hbar^2}} \quad (2.12)$$

In Equation 2.2, m is the electron mass, \hbar is the reduced Planck constant, and E and E_0 are the incident photon and core level electron binding energies respectively. The $\chi(k)$ value can be weighted to produce a more uniform k -space spectrum, if desired, as incident energy and atomic number of the scattering atom affect the amplitude of backscattered photoelectron waves. Finally, the EXAFS equation for each individual path can then be described by:^{130,162}

$$\chi(k) = \frac{N e^{-ik^2 \sigma^2} e^{-\frac{2R}{\lambda(k)}} f(k)}{kR^2} \sin(2kR + \delta(k)) \quad (2.13)$$

Finally, oscillations in the extended region of the X-ray absorption spectrum are fit to a weighted spline curve using analysis software, yielding k -space spectra (see Figure 2-8).¹³⁰ When Fourier-transformed this signal is converted into a function of radial (R) space, which is then fitted with scattering paths determined using *ab initio* simulations (Section 2.4.1).¹³⁰

Using this method, it is possible to obtain useful structural information (*i.e.* bond length and coordination values).

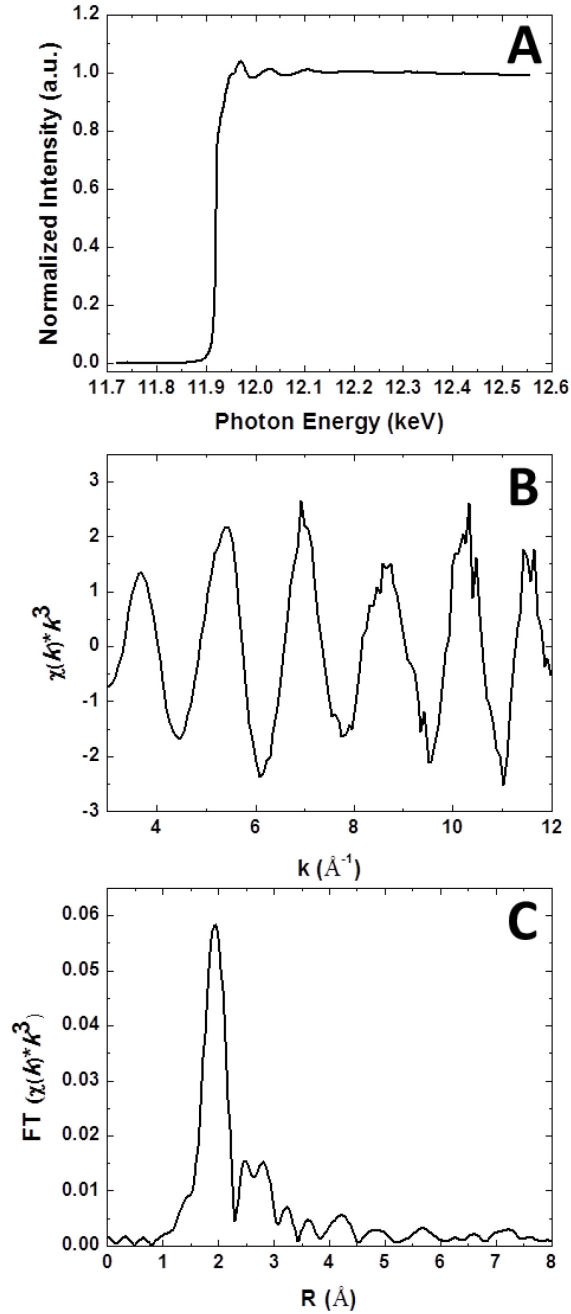


Figure 2-8. Processing of an EXAFS spectrum, depicting the corresponding A) extended region of the X-ray absorption spectrum, B) k -space spectrum, and C) R -space spectrum.

WinXAS[®] 3.1 was used for EXAFS fitting and data analysis.^{163–166} The uncertainty values for each fitting parameter determined using WinXAS were much lower than the same fits conducted using Artemis, EXAFS fitting software developed for the open-source IFEFFIT project.¹⁶⁷ The discrepancy may be due to WinXAS setting the number of free parameters at $n + 2$, while this value is $n + 1$ in Artemis. To calculate uncertainty with WinXAS[®], an application (Analyzer 0.1), developed by Paul Duchesne of the Zhang Group, was used to convert the uncertainty values given by WinXAS[®] into more reasonable values using the same method employed by Artemis.¹⁶⁷

2.4 Computational Studies

Computational techniques are ideal for studying samples or behaviour that is difficult or currently untenable by means of lab-based experimentation. The goal of this research was to better understand structure and bonding in Au nanostructures; including the reactivity of Au NPs with model biomolecules and the effect on coordination and bond length, as well as size and compositional effects on Au NPs, with changes in size, structure, coordination, and composition. Using computational methods, it was possible to access information regarding coordination and bonding with EXAFS simulations, as well as electronic character via *l*-DOS, charge transfer, and Fermi-level energy calculations.

In order to perform site-specific calculations on these samples, it was first necessary to know with accuracy the spatial coordination of all atoms in the system, or in a similar coordination environment as is the case for the Au NP samples. Fortunately, due to the recent accessibility of X-ray crystallographic coordination data for the Au₂₅⁻ and Au₁₀₂ nanoparticles,^{28,52} it was possible to study both the local environments and local electronic

character of these Au nanosystems, permitting insight into the organization, bonding, and electronic character of these samples.

2.4.1 FEFF Calculations

Electronic state calculations, such as *I*-DOS, charge transfer, and Fermi-level energy corrections are useful to better understand the nature of the Au bonding. Using FEFF (version 8.2), an *ab initio* self-consistent multiple-scattering code which uses Green's functions to reduce computational cost, it was possible to efficiently simulate the fine-structure present in XAS spectra and *I*-DOS of complex structures (*e.g.* Au nanosystems).¹⁶⁸ Although mostly used for XAS simulations, *I*-DOS is useful in the determination of electron orbital occupation and electronic state information, making FEFF useful in studying site-specific electronic interactions. EXAFS scattering path calculations are important, as they yield geometric information about bonding environments. Calculated EXAFS spectra can then be averaged and compared with experimental data.

Due to the high computational cost, calculations were carried out using the Atlantic Computational Excellence Network (ACEnet). ACEnet operates several high performance computing clusters at various universities across Atlantic Canada. The ability to access ACEnet remotely, as well as run multiple FEFF calculations in parallel, make ACEnet essential for these studies.

2.4.2 Crystal and Molecule Modeling Software

CrystalMaker® is a crystal and molecular modeling program capable of visualizing complex molecules and systems, and was used to import the X-ray crystallographic

coordinates of the Au₂₅⁻ and Au₁₀₂ systems.^{28,52} Allowing translation of the molecules, CrystalMaker® software was used primarily for the visualization of surface organization, calculation of bond lengths and aurophilic distances, and atomic coordinates for use in the FEFF-based calculations.

CHAPTER 3 LIGAND EFFECT (PART 1)

Reproduced in part with permission from:
Christensen, S. L.; Chatt, A.; Zhang, P. "Biomolecule-Coated Metal Nanoparticles on Titanium" *Langmuir*, **2012**, 28 (5), 2979-2985.
Copyright 2012 American Chemical Society.

3.0 Motivation

Understanding both the ligand effect and the metal effect when studying Au NP-ligand interactions is very important. In order to study the ligand effect, this chapter deals with the comparison of large and small ligand molecules. By monitoring changes to surface-functionalized Au NP size and structure, it is possible to determine the effect of ligand size on Au NP deposition. The study aims to understand the mechanism of particle growth with biocompatible ligands of different size. Due to the interest in Ti-supported Au NPs for orthopaedic implant systems, this chapter is introduced from a biomedical standpoint, before presenting the specific results.

3.1 Introduction

Ti and its alloys are the most widely used materials in tissue engineering, finding use in hip, knee, and joint replacement prostheses, as well as dental and load bearing implants.¹⁶⁹⁻¹⁷² The variety of biological applications available today is due in large part to their excellent bio-compatibility properties.^{173,174} In order to provide new functionality to Ti-based bio-materials, immobilization of functional materials onto a Ti surface is considered a promising approach.^{100,175,176} With the rapid advancement of nanoscience and nanotechnology, significant progress has been made in the past two decades to link nanoscale

functional materials to the surfaces of functional substrates.^{101,177,178} The introduction of inorganic nanoparticles (NPs) to Ti surface has shown useful application in adding anti-cancer and bactericidal capability to Ti-based biomaterials.^{179–181} Meanwhile, immobilization of small bioactive molecules and proteins were also found efficient in improving the performance of Ti-based orthopaedic implants.^{182–184}

While fully understanding the modification of Ti substrates is a worthy goal, the purpose of this research is to gain a better understanding into the interaction of small metal NPs with thiolate-based biomolecule ligand systems, in order to emulate eventual in-vivo systems. Building on a previously reported one-step procedure¹⁰⁶, we present a simple and efficient wet-chemical method to simultaneously immobilize inorganic nanoparticles and biomolecules, by coating a Ti surface with biomolecule-functionalized metal NPs. The bio-coated metal nanoparticles are formed by galvanic reduction of pre-mixed metal compounds and sulfur-containing biomolecules with refreshed Ti surface, leading to the deposition of bio-functionalized nanoparticles on Ti substrates.¹⁰⁶ We show that a series of Au NP-Ti samples with varied size and coverage, metal composition (Au, Ag, Pd), as well as biomolecule coatings (MPG and BSA), can be prepared using this method.¹⁰⁶ By performing element-specific X-ray experiments including extended X-ray absorption fine structure (EXAFS), X-ray absorption near edge structure (XANES) and X-ray photoelectron spectroscopy (XPS), a detailed picture of the atomic structure and AuNP-biomolecule bonding is presented. Ag and Pd biomolecule-coated NPs were also prepared in order to observe changes in systems where only the metal NP composition differs. This analysis of bio-functionalized nanoparticles on Ti substrates provides insight on a useful prototype

surface model, describing the structure and bonding of bio-coated metal nanoparticles, expediting their future application in orthopedic and biomedical fields.

3.2 Experimental

3.2.1 Synthesis

High purity Bovine Serum Albumin (BSA) and N-(2-mercapto-propionyl) glycine (MPG) were purchased from Sigma Aldrich and were used without further purification. 99.5% pure annealed titanium was purchased from Alfa Aesar, and was punched into 1 cm discs using the industrial hole-punch of the Mechanical Engineering Department at Dalhousie University. The discs were then sonicated for five minutes in acetone, five minutes in ethanol, and five minutes in de-ionized water (18.2 M Ω •cm, Barnstead Nanopure[®] Diamond[™] UV purification system). Prior to use, the titanium discs were etched in concentrated HCl (36-38%, ACS Grade, Caledon) for 1 hour.

To prepare the Au:BSA and Au:MPG systems, the appropriate ratios of HAuCl₄•3H₂O (99.99%, Alfa Aesar) to BSA and MPG were used, keeping the concentration of Au salt constant while varying the ligand system concentration. The solutions were prepared separately, and all solutions used de-ionized water as solvent. The Ag and Pd systems were prepared using the same procedure, using AgNO₃ (99.9%, Alfa Aesar) and KPdCl₄ (98%, Sigma Aldrich), respectively, as starting components. The metal salt and ligand solutions were then stirred together and left for two minutes. When ready, the reduced Ti discs were rinsed of any remaining HCl with de-ionized water, and placed on a cleaned Teflon disc in the metal:ligand solution so as not to interfere with the stirring rod.¹⁰⁶ After

two minutes, discs were removed, rinsed in de-ionized water, and dried under argon gas. The discs were then placed in vials under argon.

Every effort was made to keep the samples free from contamination and oxidization, and overall they remain quite stable. SEM images of the AuNP-based systems, of primary concern in this study, were acquired months after deposition, and no noticeable structural changes were evident. It should be noted that all samples were prepared days before experimentation, and were kept under argon gas until they are analyzed.

3.2.2 Characterization

Morphology of nanoparticles was determined using the Hitachi S-4700 FEG Scanning Electron Microscope of the Institute for Research in Materials at Dalhousie University. The images were captured with an accelerating voltage of 20 kV and emission current of 10 μA , with a working distance of 6-7 mm. ImageJ software was used to determine surface coverage and nanoparticle size, using the Ferret's diameter (diameter of particle at widest point) and subsequent areas of the nanoparticle systems.

Ag and Pd K-edge X-ray absorption near-edge structure (XANES) and all X-ray photoelectron spectroscopy (XPS) experiments were conducted at the Canadian Lightsource (CLS) in Saskatoon, SK, Canada, while the Extended X-ray Absorption Fine-Structure (EXAFS) experiments and Au L₃-edge XANES were conducted at the Advanced Photon Source (APS) in Argonne, IL, USA.

The XANES experiments for Ag, Pd and S were performed on the Soft X-ray Microcharacterization Beamline (SXRMB – 06B1-1). The beamline uses a bending magnet source, and experiments were run in Total Electron Yield (TEY) mode due to extreme noise

in the fluorescence yield (FLY) mode spectra. Samples were affixed to the sample holder with minimal carbon tape. Au L₃-edge XANES spectra were collected in order to compare white line intensity as well as qualitative structural information.

The XPS experiments were performed on the High-Resolution Spherical Grating Monochromator beamline (SGM – 11ID-1). The beamline uses an undulator source, and experiments were run at the temperature of liquid nitrogen (83 K) in order to minimize photo-degradation of the samples.¹⁸⁵ The samples were affixed to the sample holder with minimal carbon tape, and sample position was tuned for maximum signal. Measurements were taken at excitation energies of 700 eV and 1000 eV, so as to remove any Auger peak convolution.¹⁴⁷ Binding energy calibration was conducted by setting the carbon 1s peak to 285.00 eV.¹⁴⁷ The Ti discs were mounted onto sample holders using small amounts of carbon tape. Powdered standards were applied directly to carbon tape mounted on the sample holder, and all excess powder was removed. The powder samples were mounted before the Ti discs in order to reduce cross-contamination. XPS peak areas and relative sensitivity factor (R.S.F.) values were in order to calculate metal:S ratios.¹⁸⁶

Au L₃-edge EXAFS experiments were performed on the PNC/XSD beamline (Sector 20). The beamline uses a bending magnet source, and experiments were run in Fluorescence Yield (FLY) at glancing angle incidence, with the samples affixed by double-sided tape to a flat Teflon grid. The EXAFS spectra were normalized and converted to *k*-space EXAFS, which were then Fourier Transformed to R-space EXAFS without correlating phase shifts. All data processing¹⁶⁴ and EXAFS fitting¹⁶⁵ were done using the WinXAS program.^{163,166} The scattering path phase shifts and amplitude used to fit the EXAFS data were generated using the FEFF8.2 program.¹⁶⁸ The structural model of a 25 Au atom thiolate-protected

cluster with known X-ray crystallographic coordinates was used to fit the first shell Au-Au and Au-S bond (although the Au-S path was later removed).¹⁶⁵ The use of the 25 Au atom cluster was used as a good approximation for fitting the first shell, though both this system and bulk gold have been used in the literature to achieve similar results.^{149,165}

3.3 Results and Discussion

Figure 3-1 shows the typical SEM images of Au NPs coated with protein (BSA) and small biomolecules (MPG). The molar ratio of Au:biomolecule is 20:1, and the two samples are abbreviated as 20AuBSA and 20AuMPG for the 20:1 Au:BSA and 20:1 Au:MPG systems, respectively. Although the 20AuMPG NPs are smaller size and greater in numbers (Figure 3-1c), the percentage of surface coverage determined by SEM for both the 20AuBSA and 20AuMPG systems are similar (21.6% and 22.1%, respectively). The greater number of Au-S interactions in the 20AuMPG system is afforded by the smaller size and less bulky MPG ligand, resulting in a higher cumulative Au-S surface interaction area.¹⁴³ When comparing the size of the particles imaged by SEM, it is determined that the size of the 20AuBSA nanoparticles is 9.6 ± 2.3 nm (Figure 3-1a and 3-1b), while the 20AuMPG nanoparticles are 4.7 ± 2.0 nm in size (Figure 3-1c and 3-1d). The distribution statistics are based on thousands of particles from multiple SEM images of the same samples. However, due to the limited resolution of SEM, it is unclear whether or not each “particle” visualized in Figure 3-1 is a single piece of Au nanoparticle or an assembly of more than one nanoparticle linked by biomolecules. Element-specific XAS and XPS measurements have been shown useful in providing information on the atomic structure and bonding of Au-thiolate

nanoparticles.¹⁸⁷ We next turn to the XAS and XPS data of these two samples to further investigate their structure and properties.

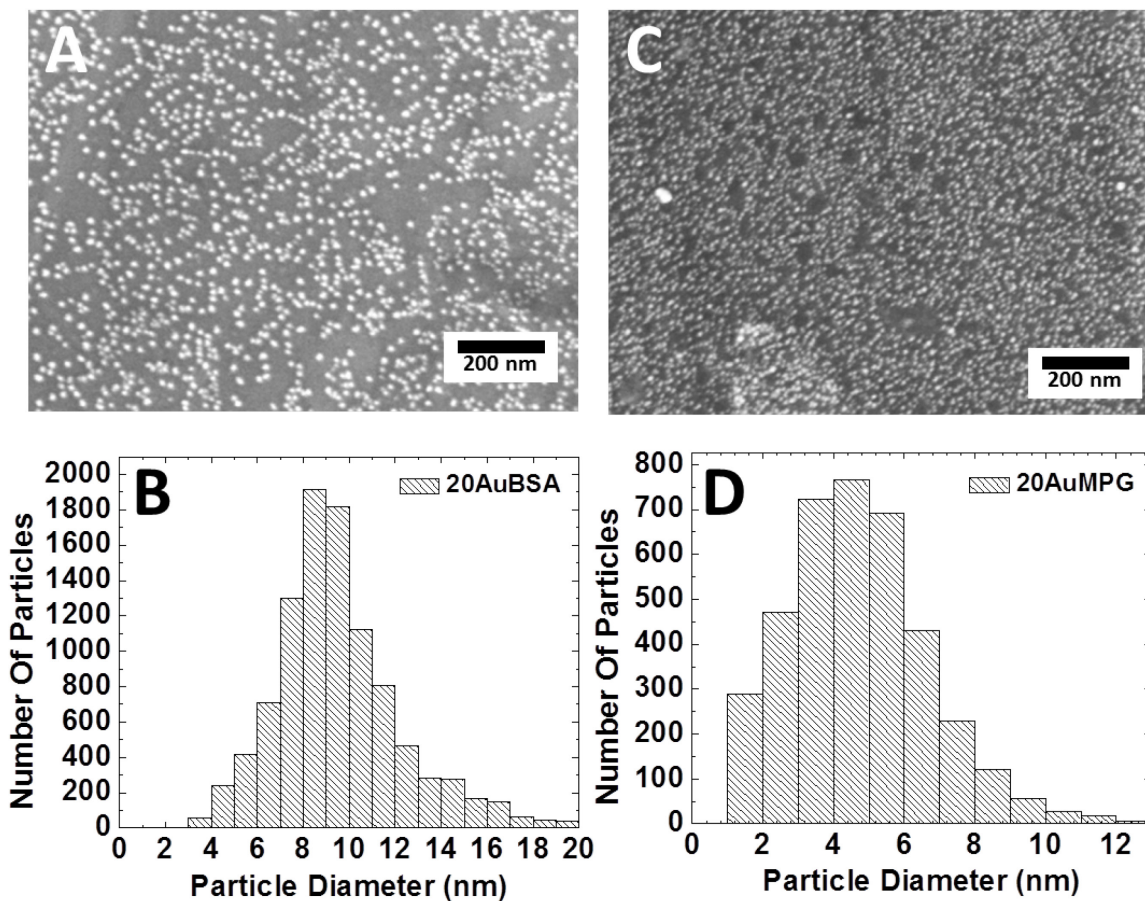


Figure 3-1. Scanning electron micrographs of bio-functionalized Au nanoparticles on Ti substrate. (A) 20:1 Au:BSA micrograph and (B) histogram, and (C) 20:1 Au:MPG micrograph and (D) histogram.

Figure 3-2 shows the Au L₃-edge XANES of 20AuBSA and 20AuMPG. There is little difference in the spectra of the 20AuBSA and 20AuMPG systems, and both show the similar face-centered cubic (FCC) resonances of bulk Au foil. The similarity of the first-resonance (the white line) following the edge jump indicates the three systems have essentially the same d-electron densities.¹⁸⁸ The third resonance feature centered at around 11947 eV is an indication of nanoparticle size, as the greater intensity in the Au foil spectrum is due to its long-range order.¹⁸⁷

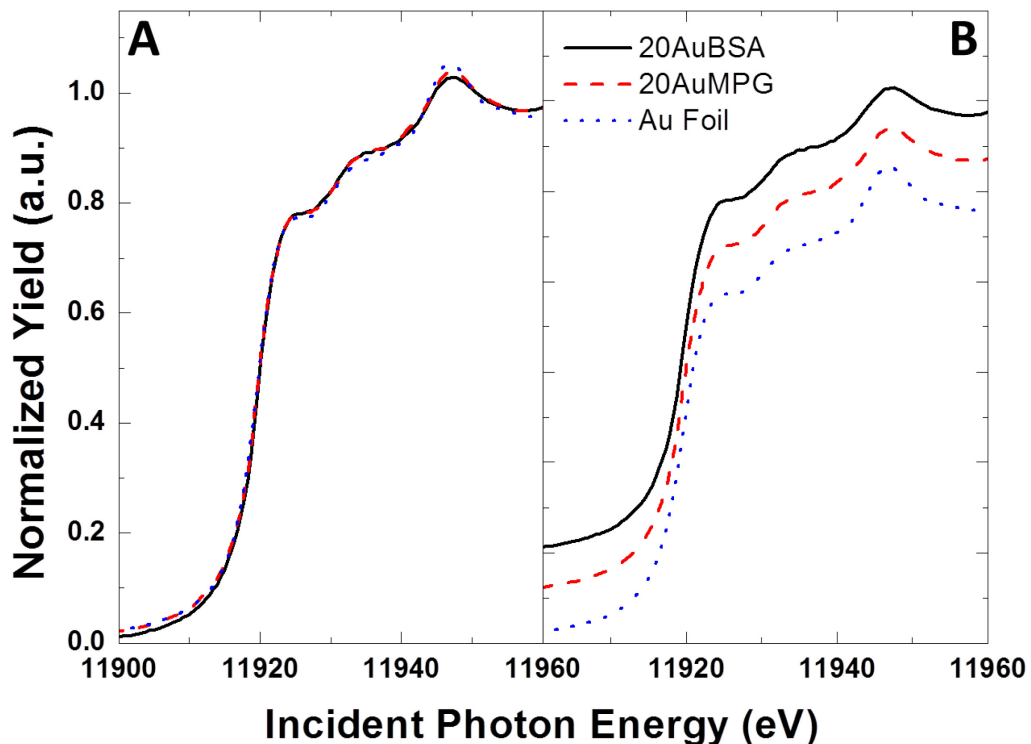


Figure 3-2. (A) Overlain and (B) staggered Au L₃-edge XANES of 20AuBSA (black solid) and 20AuMPG (red dash) systems, with Au foil (blue dot) for feature comparison.

Figure 3-3 is the Au L₃-edge k-space EXAFS for the 20AuBSA and 20AuMPG systems and bulk Au foil for comparison. Consistent with the XANES spectra, the oscillation

patterns are similar and denote an FCC structure. Being consistent with Figure 3-2 data, the EXAFS oscillation intensity for the 20AuBSA system ($N=7.8$) is noticeably lower than that of the 20AuMPG system ($N=10.2$), describing the smaller averaged coordination number of 20AuBSA.

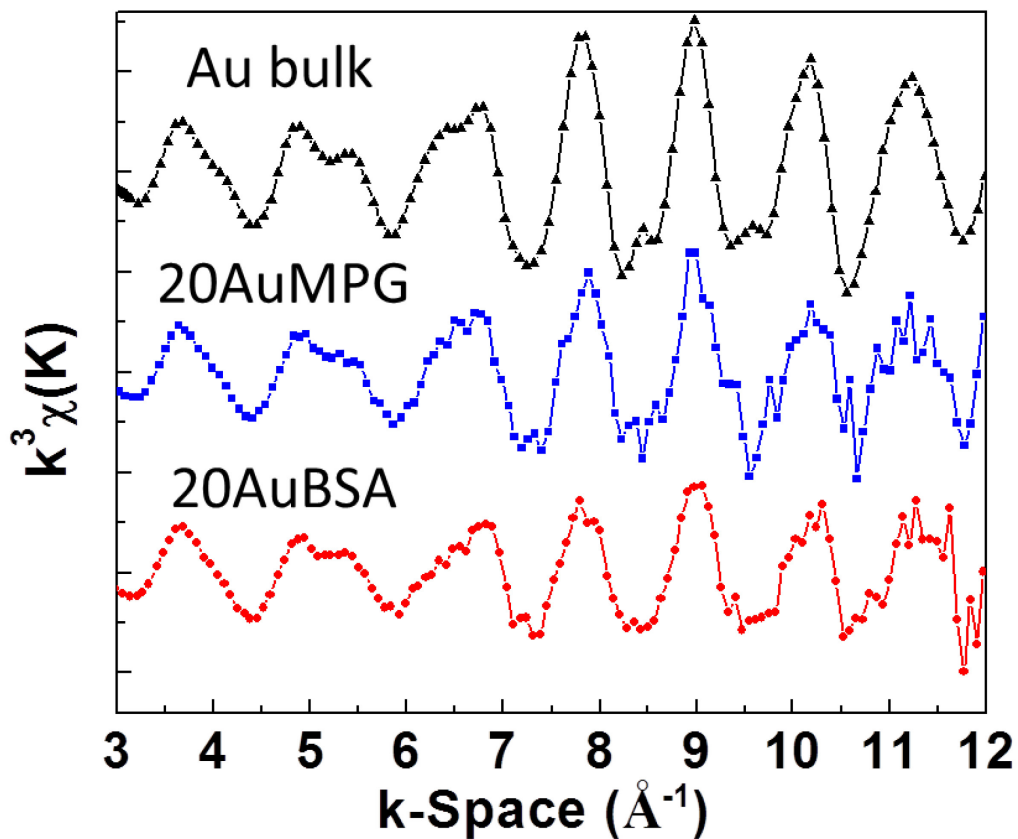


Figure 3-3. Au L_3 -edge k-space EXAFS of 20AuBSA (red circle), 20AuMPG (blue square), and bulk Au foil (black triangle) systems.

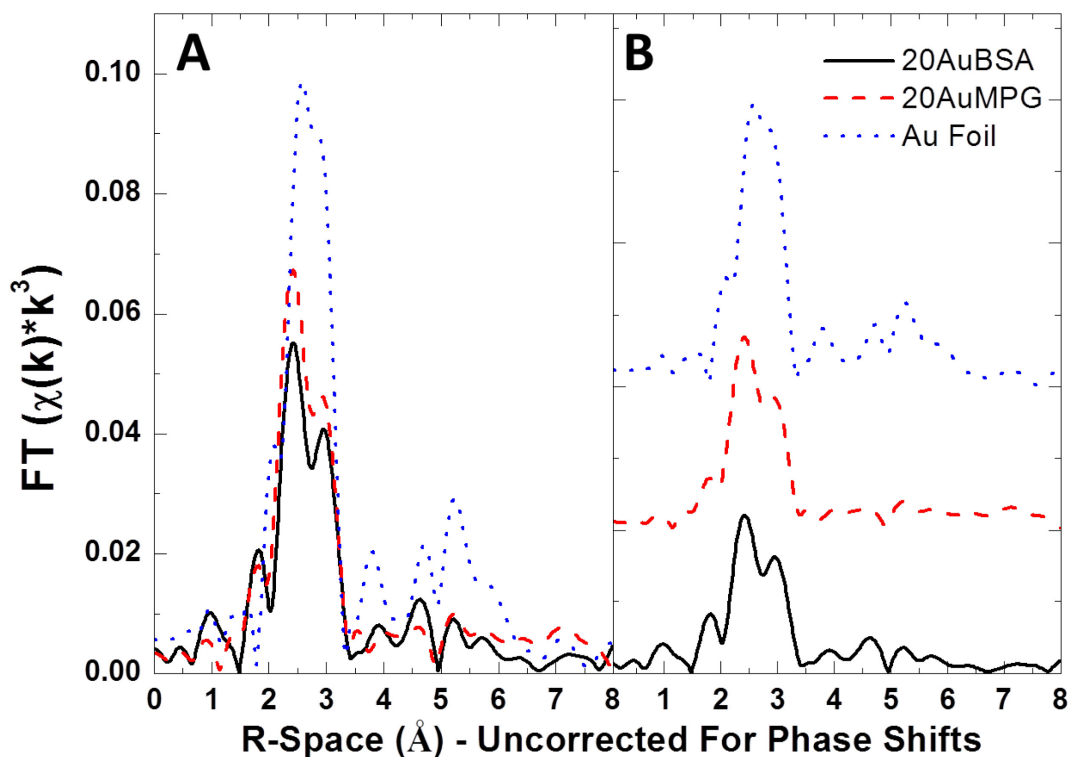


Figure 3-4. (A) Overlain and (B) staggered Au L₃-edge R-space EXAFS of 20AuBSA (black solid), 20AuMPG (red dash) systems, with bulk Au foil (blue dot) for comparison.

The k -space EXAFS from Figure 3-3 are Fourier-transformed, and the resultant FT-EXAFS of the two Au NPs and Au foil are shown in Figure 3-4. The most intense FT-EXAFS feature (uncorrected for phase shift) in the region of 2-3 Å is due to the first-shell Au-Au interaction. The intensity of this feature is determined by the average Au-Au coordination number.¹⁸⁵ The lower intensity of the first shell Au-Au feature of the 20AuBSA system (0.055), when compared with that of the 20AuMPG system (0.069), supports the indication from XANES that the 20AuBSA system should have the lower coordination number.

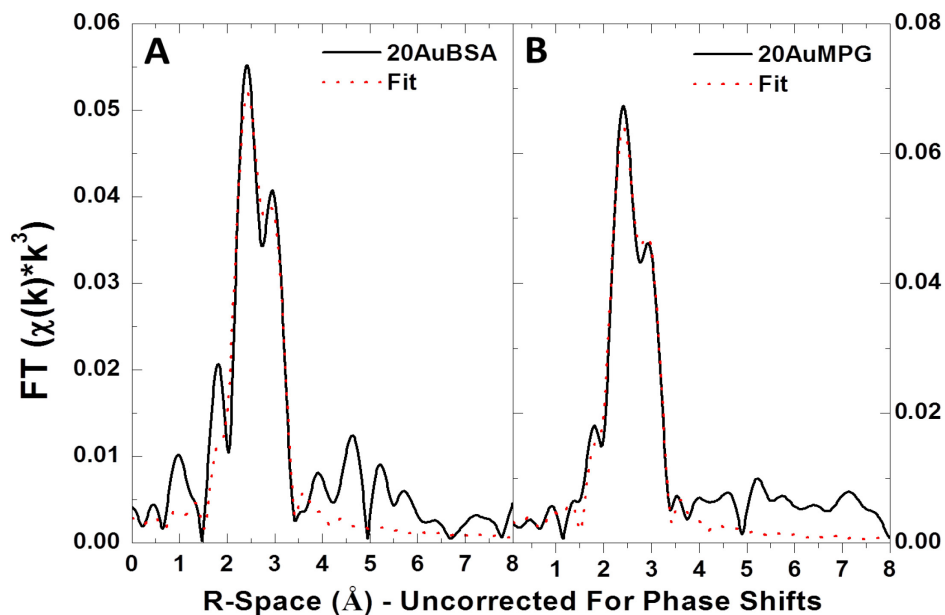


Figure 3-5. Au L_3 -edge R-space EXAFS (black solid) and fits (red dash) of (A) 20AuBSA and (B) 20AuMPG systems. Spectra are not corrected for phase. Fits are one-shell Au-Au path and do not include features outside of a 1.6 to 3.3 Å window.

The Au L_3 -edge R-space EXAFS spectra were fitted using first-shell scattering paths calculated with FEFF 8.2 code and WinXAS 3.1 software. Figure 3-5 represents the best fittings for the 20AuBSA and 20AuMPG systems. Two-shell fits, involving both the Au-Au and Au-S paths were initially attempted, but due to the low contribution of the Au-S shell no reliable two-shell fits could be obtained for these systems.

Table 3-1. Au L_3 -edge R-Space EXAFS Fitting Results for 20AuBSA and 20AuMPG systems, as well as Au foil for comparison ^a

Sample	Path	Coordination Number (N)	Bond Length (Å)	Debye-Waller Factor	E_0 Shift
20AuBSA	Au-Au	7.8 ± 1.7	2.85 ± 0.03	0.0083 ± 0.0029	-0.5
20AuMPG	Au-Au	10.2 ± 1.5	2.84 ± 0.01	0.0091 ± 0.0014	-0.4
Au Foil	Au-Au	11.6 ± 0.8	2.86 ± 0.02	0.0075 ± 0.0014	0.1

^a Highest quality fit was obtained with $S_0^2 = 0.9$.

Only one-shell fitting results are presented in Table 3-1. In regards to the coordination number (N) values in Table 3-1, the Au-MPG systems show a greater N value than the 20AuBSA system, while the Au foil is very near that of bulk FCC Au (Table 3-1). The difference in N demonstrates a greater number of Au-Au interactions for the 20AuMPG system when compared to that of Au-BSA.

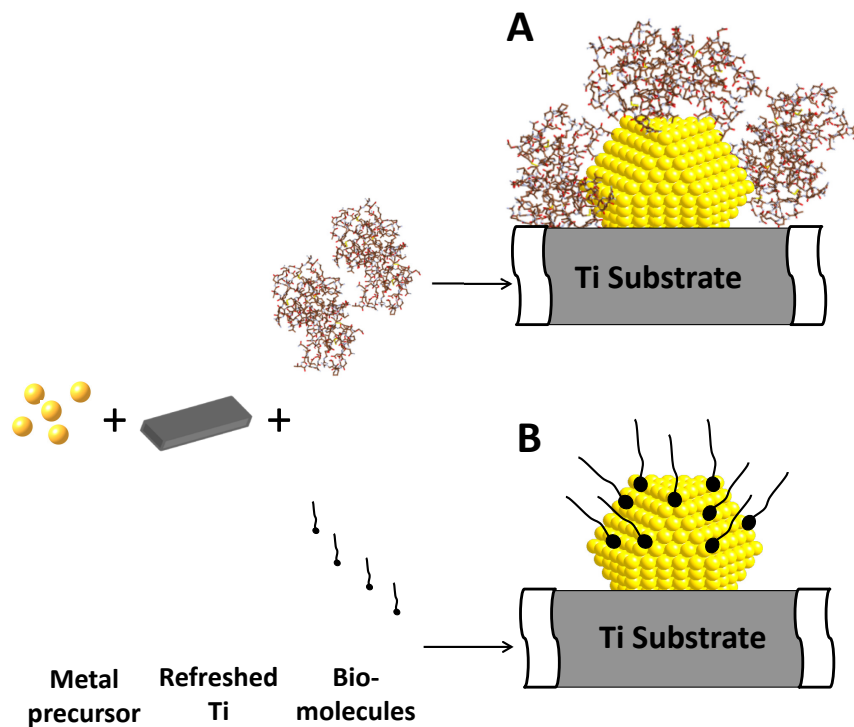


Figure 3-6. Schematic illustration of biomolecule functionalized Au nanoparticle deposition for (A) protein functionalized Au nanoparticles on a Ti substrate, and (B) small model-biomolecule functionalized Au nanoparticles on a Ti substrate.

In Figure 3-6, different interaction mechanisms are depicted for large and small biomolecule coated systems. For small biomolecules, such as MPG, the Au exists in solution with the ligand, before reduction to metallic Au. Once fresh Ti reduces the Au-thiol solution, Au nanoparticles can be quickly formed. For the larger biomolecule (protein) Au synthesis¹⁸⁹, Au is first dispersed in each protein, where it is then partially reduced. Following this step, larger Au nanoparticles are formed at the interface of multiple protein aggregates.

Au-ligand bonding of the two nanoparticle systems (20AuBSA and 20AuMPG) was closely compared using XPS of the Au 4f_{7/2} data (Figure 3-7). Au 4f XPS is sensitive for probing metal-ligand interaction, as line-position and shape of features are superior to Au L₃-edge XANES. While the energy resolution for the higher-energy Au L₃-edge is ~1 eV, XPS experiments have much higher energy resolution (~0.1 eV).¹⁴⁷ In Figure 3-7, we see a positive shift of 0.1 eV in the 20AuMPG system, while there is a broadening on the high-energy side. Broadening of Au 4f on the high-energy side is due to the contribution of Au-S bonding.^{147,187} These two observations simultaneously indicate that in the 20AuMPG system there is a higher density of Au-S bonds. A higher density of Au-S bonds can be explained by the greater accessible Au surface area provided in the Au:MPG system. Figure 3-8 are XPS survey scan spectra, which were used to determine metal:S ratios. The magnitude of the metal:sulfur ratio above 1 is a testament to nanoparticle size, while a value near parity is indicative of a monolayer-type system (Table 3-2). For the 20AuMPG system, the MPG-thiolate groups stabilize the surface Au atoms. However, in the 20AuBSA system, each Au nanoparticle interacts with the protein surface in a non-thiolate weakly-bonding interaction, as there are fewer sulfur sites on the exterior of the BSA protein.¹⁴⁶

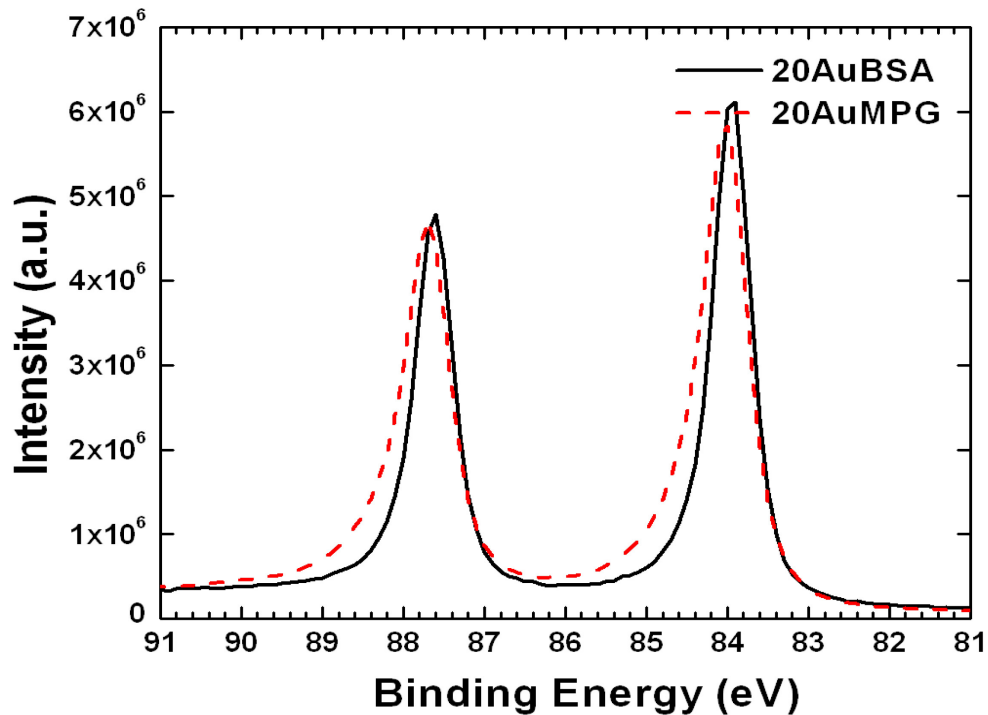


Figure 3-7. Au 4f_{7/2} XPS spectra of 20AuBSA (black solid) and 20AuMPG (red dash) systems, denoting broadening and shift to higher binding energy in the 20AuMPG system.

Table 3-2. Metal:S ratios from XPS survey scan spectra.

System	Metal R.S.F.*	Metal Peak Area	Sulfur R.S.F.	Sulfur Peak Area	Metal:S Ratio
20AuBSA	4.95	120408	0.54	5889	2.23
2AuBSA	4.95	116961	0.54	5892	2.17
20AuMPG	4.95	485553	0.54	22477	2.36
2AuMPG	4.95	139517	0.54	18615	0.82
20AgBSA	5.20	21603	0.54	367	6.11
20AgMPG	5.20	4580	0.54	350	1.36
20PdBSA	4.60	11581	0.54	376	3.62
20PdMPG	4.60	4066	0.54	526	0.91

* Relative Sensitivity Factor ²²

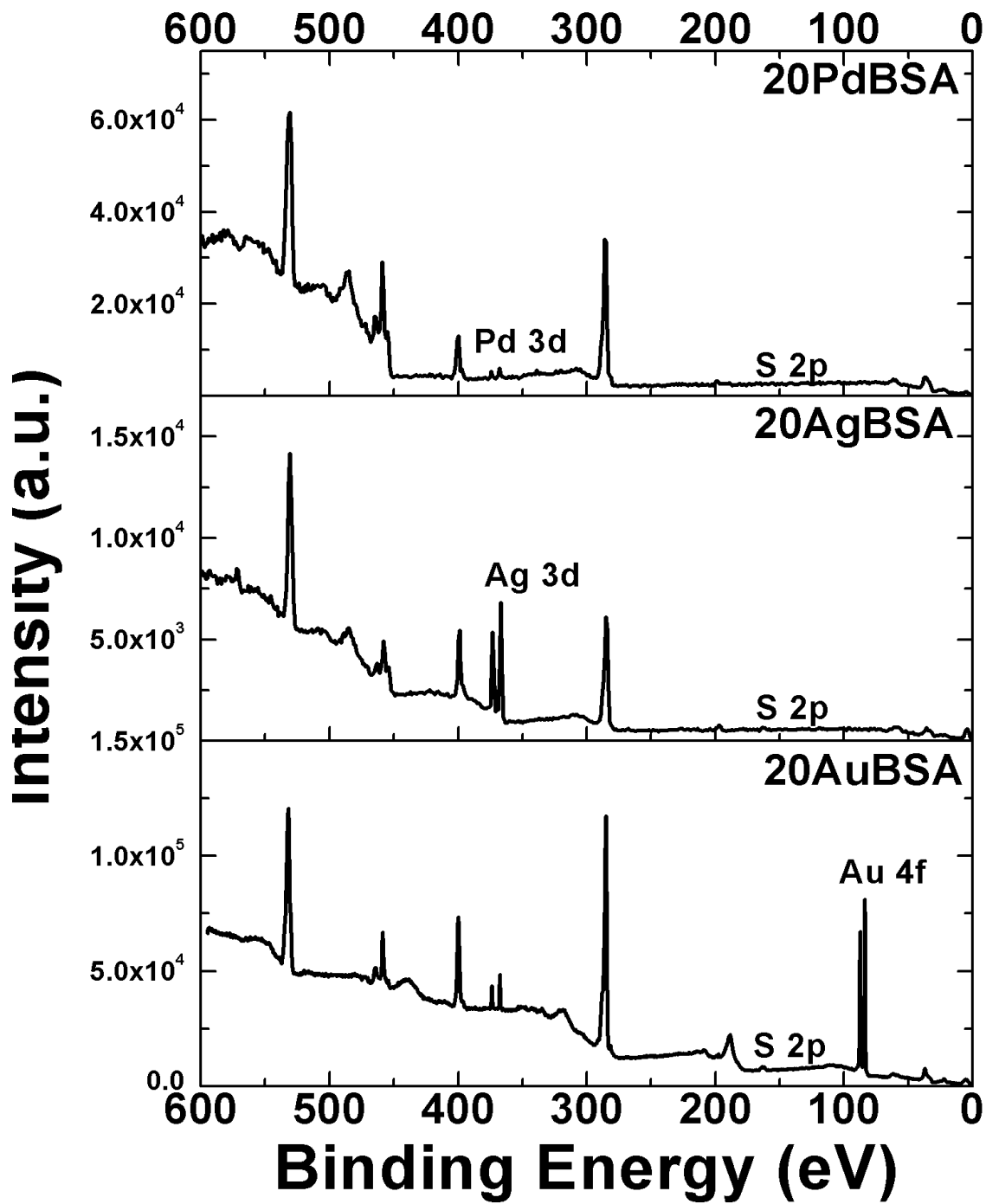


Figure 3-8. XPS survey scan spectra of the 20AuBSA, 20AgBSA, and 20PdBSA systems.

Ligand concentration is also of interest, and trends developed by altering the Au/biomolecule ratio can provide valuable insight into the mechanics of nanoparticle bio-functionalization. Figure 3-9 shows a comparison of the Au L₃-edge XANES for the Au-BSA and Au-MPG systems. For the 20:1, 5:1, and 2:1 ratios of Au:BSA, the systems are essentially identical, meaning that as the concentration of BSA increases, the Au-Au coordination number remains unchanged. This is understandable, as the BSA protein will effectively protect the Au salt even at low concentrations due to the extremely large size of the protein relative to the Au atoms. However, the Au L₃-edge XANES for the 20:1, 5:1, and 2:1 ratios of Au:MPG in Figure 3-9c show interesting deviations from each other. As the concentration of MPG in the system increases, the white line intensity increases as well, indicating more Au-S charge transfer. This observation suggests that Au-Au coordination in the nanoparticles decreases with increasing MPG concentration. As a result, there is a higher concentration of Au-S bonding. The result of concentration effect on the Au nanoparticle structure indicates Au nanoparticle Au-Au coordination and surface bonding is more sensitive to changes in the concentration of the smaller biomolecule MPG than to larger protein BSA. SEM images corroborate these observations, and can be seen in Figure 3-10.

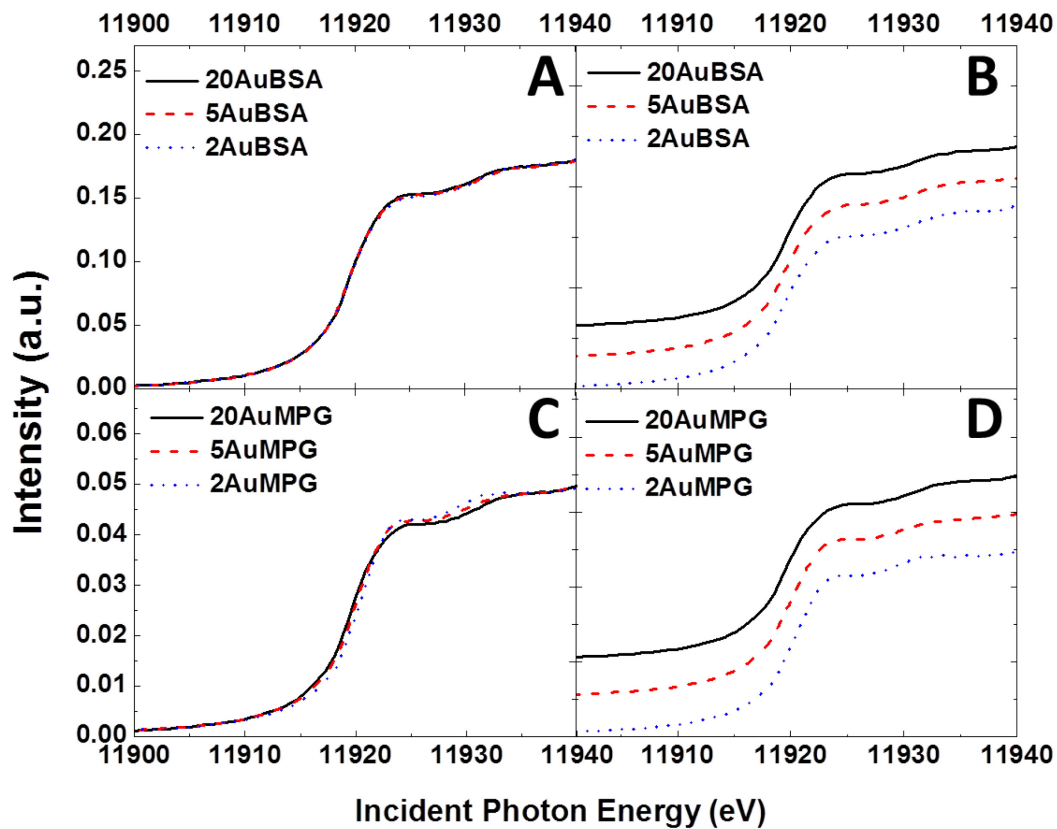


Figure 3-9. Au L₃-edge XANES spectra of AuBSA and AuMPG systems, comparing differences in concentration of ligand systems. (A) Overlain and (B) staggered Au L₃-edge XANES spectra of 20:1, 5:1, and 2:1 Au:BSA systems. (C) Overlain and (D) staggered Au L₃-edge XANES spectra of 20:1, 5:1, and 2:1 Au:MPG systems.

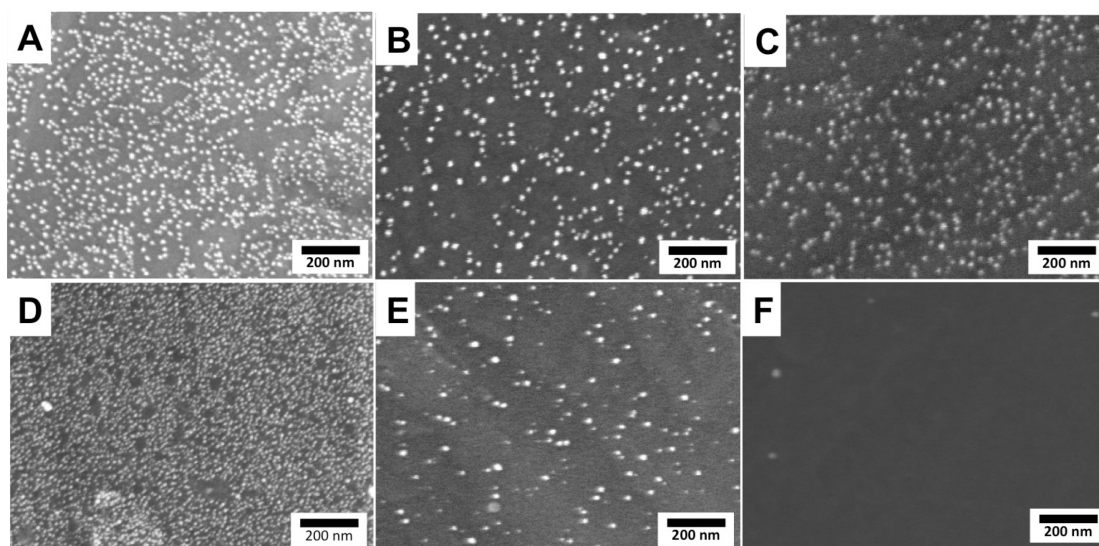


Figure 3-10. Scanning electron micrographs of bio-functionalized Au nanoparticles on Ti substrate. (A) 20:1 Au:BSA, (B) 5:1 Au:BSA, (C) 2:1 Au:BSA, (D) 20:1 Au:MPG, (E) 5:1 Au:MPG, and (F) 2:1 Au:MPG.

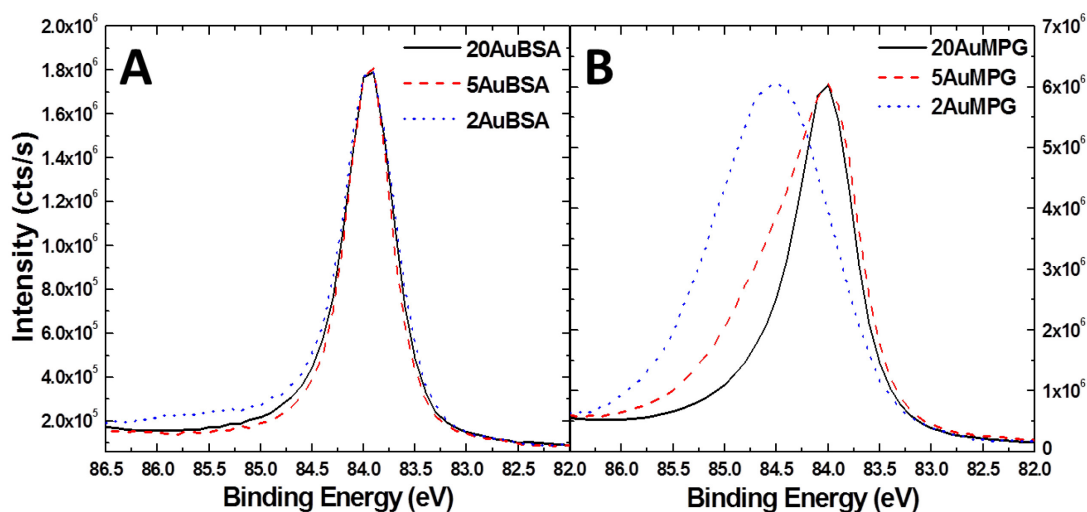


Figure 3-11. (A) Overlain Au $4f_{7/2}$ XPS spectra of 20AuBSA (black solid), 5AuBSA (red dash), and 2AuBSA (blue dot) systems, and (B) overlain Au $4f_{7/2}$ XPS spectra of 20AuMPG (black solid), 5AuMPG (red dash), and 2AuMPG (blue dot) systems, denoting a broadening occurring with greater concentration of the MPG ligand system, as well as a shift to higher binding energy.

The Au $4f_{7/2}$ XPS spectra for the 20:1, 5:1, and 2:1 Au:BSA system are presented in Figure 3-11a. There is little difference in peak-width as the concentration of the ligand changes, which supports the Au-protein formation model and is consistent with the XANES results in Figure 3-9a, as the Au-Au coordination of the nanoparticles does not change with concentration of BSA. Figure 3-11b is the Au $4f_{7/2}$ XPS spectrum of the 20:1, 5:1, and 2:1 Au:MPG system, and demonstrates that there is a large difference in particle Au-Au coordination as concentration of MPG is varied. The Au $4f_{7/2}$ peak broadens with increasing concentration of MPG as well as shifting to increased binding energy with more Au-S interaction, indicating smaller particles were generated, consistent with the XANES results in Figure 3-9c. In the 20AuMPG system, there is a greater concentration of core gold with respect to the surface Au-thiolate bonds. In the 5AuMPG system, the relative ratio of core Au to surface Au-thiolate decreases, leading to peak broadening and the development of a shoulder at higher binding energy. Finally, in the 2AuMPG system, the Au-S coordination is small enough that the number of Au-thiolate interactions outweighs the amount of core Au, and there is even more broadening and a significant shift toward higher binding energy. This is consistent with the fact that few particles were visible under SEM of the 2AuMPG system (Figure 3-10 and Table 3-2).

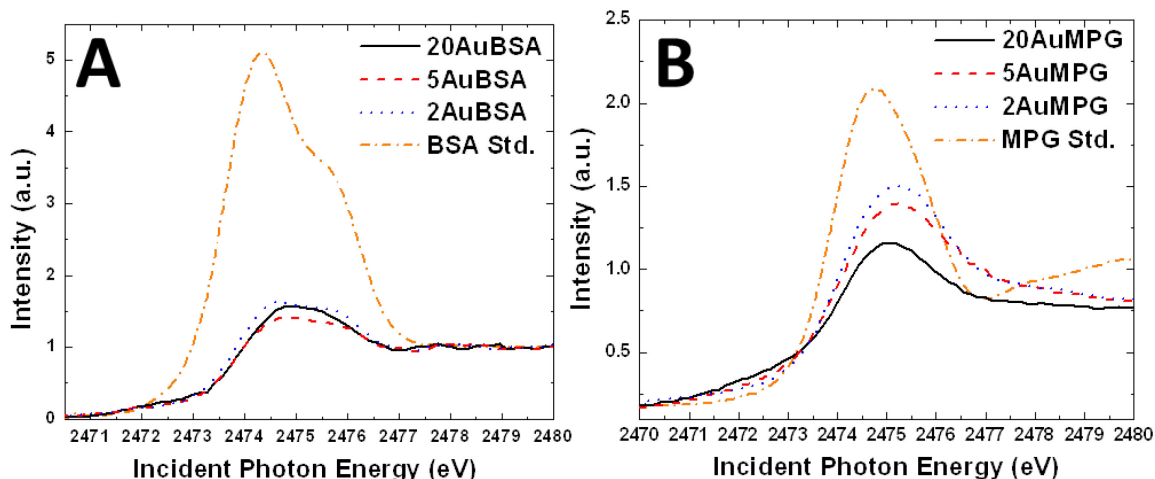


Figure 3-12. (A) S K-edge XANES spectra of 20AuBSA (black solid), 5AuBSA (red dash), and 2AuBSA (blue dot) systems, in comparison with BSA standard (orange dash-dot), denoting the disappearance of the 2474.3 eV and 2475.7 eV disulfide bridge peaks. (B) S K-edge XANES spectra of 20AuMPG (black solid), 5AuMPG (red dash), and 2AuMPG (blue dot) systems, in comparison with MPG standard (orange dash-dot), denoting a shift toward higher incident photon energies (higher binding energies) with increases in Au-thiolate bonding.

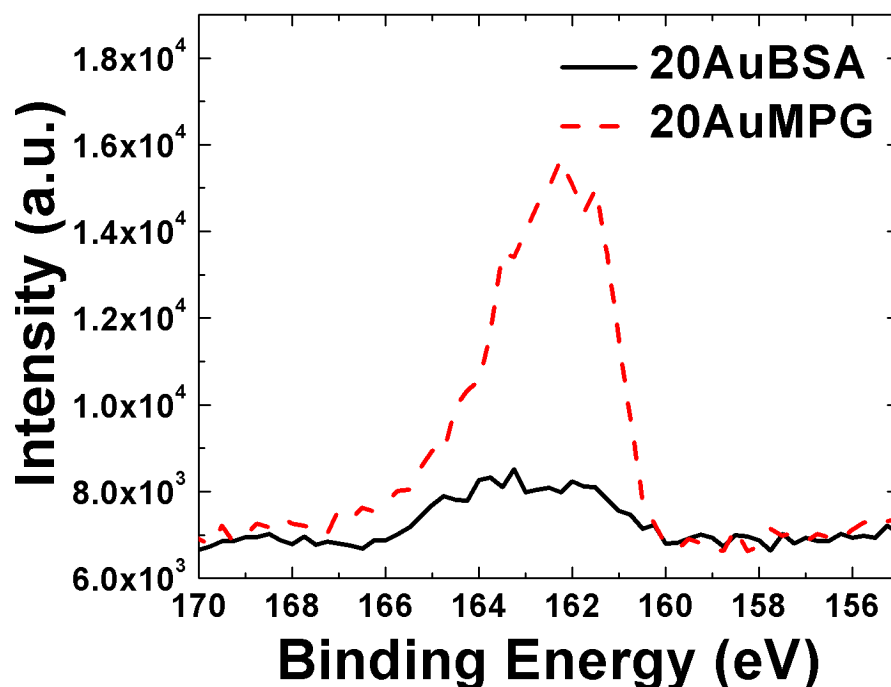


Figure 3-13. S 2p XPS spectra of 20AuBSA (black solid) and 20AuMPG (red dash) systems.

To further investigate the Au-thiolate bonding in these systems, S K-edge XANES (Figure 3-12) and S 2p XPS (Figure 3-13) measurements were conducted. As S K-edge XANES provided better resolution spectra, the discussion will focus on these experiments. A comparison of the AuBSA system to BSA standard shows a reduction in intensity of both the 2474.3 eV feature and its shoulder at 2475.7 eV (Figure 3-12a). These two features are indicative of S-S bonds, of which each BSA protein has 17 (34 disulfide-bridged S atoms).¹⁴⁷ Therefore, the reduction or disappearance of this feature indicates the formation of Au-S bonds, replacing some of the S-S bonds. Figure 3-12b is the S K-edge XANES of the AuMPG system in comparison with an MPG standard spectrum. There is a shift of 0.3 to 0.5 eV toward higher-energy for the AuMPG systems, due to Au-S bond formation. The S K-edge XANES spectrum for the 20:1, 5:1, and 2:1 Au:MPG systems also shift relative to each other, as more Au-S bonds will increase the binding energy, and in turn the energy required to excite an electron from the S 1s orbital. This is corroborated by the Au 4f_{7/2} XPS spectra in Figure 3-11b. The increase in the 2475 eV feature intensity is likely due to the increased number of Au-S interactions as the Au surface area increases.

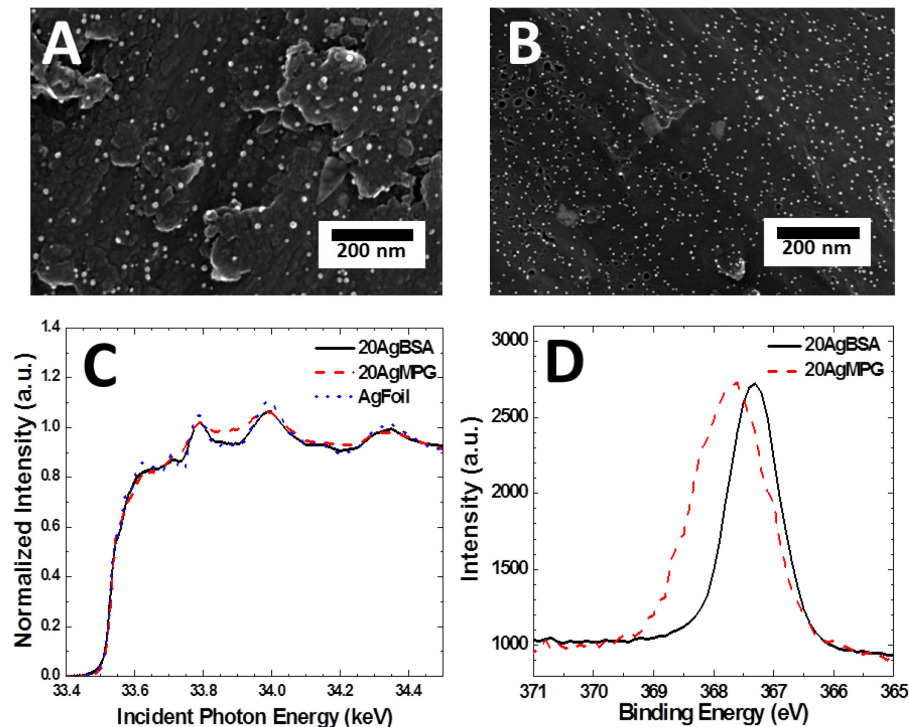


Figure 3-14. Scanning electron micrographs of bio-functionalized Ag nanoparticles on Ti substrate of (A) 20:1 Ag:BSA and (B) 20:1 Ag:MPG systems. Ag L_3 -edge XANES spectra (C) are shown of the 20AgBSA and 20AgMPG systems, as well as Ag foil for comparison. The Ag $3d_{5/2}$ XPS spectrum (D) denotes shift and broadening in the 20AgMPG system.

This study was then extended to the preparation of other metal nanoparticle systems. Ag was selected due to its well-known antibacterial properties¹⁹⁰, while palladium was chosen due to its promising application in self-assembled monolayer-based nanotechnology.¹⁸⁷ Figure 3-14 shows the SEM and XANES of bio-coated nanoparticles. The particle size is 13.4 ± 6.2 nm for the 20AgBSA system and covers 21.6% of the surface, while the particle size is 9.9 ± 3.4 nm for the 20AgMPG system with 22.1% surface coverage. Long range Ag L_3 -edge XANES show both nanoparticle systems to have similar features, indicating both are metallic with FCC structure. However, upon close inspection of the Ag $3d_{5/2}$ XPS in Figure 3-14d, we see the 20AgMPG sample shows a positive shift of 0.4

eV to a higher binding energy, accompanied by broadening on the high-energy side. Both of these observations indicate that there is a higher density of Ag-S bond in the 20AgMPG sample. The results in Figure 3-14d are consistent with the data in Figure 3-14c, where the 20AgMPG system shows lower oscillation intensity in the post-edge region, indicating the nanoparticle size of 20AgMPG nanoparticles to be smaller. Considering the surface bonding of MPG-stabilized Ag is mainly Ag-thiolate, it is understandable that the thiolate removes d-electron density from the Ag, resulting in a positive shift in Ag 3d XPS binding energy. On the other hand, the surface bonding of BSA-stabilized Ag is similar to that of the 20AuBSA system, in that only weakly bonding metal-protein bonding exists.

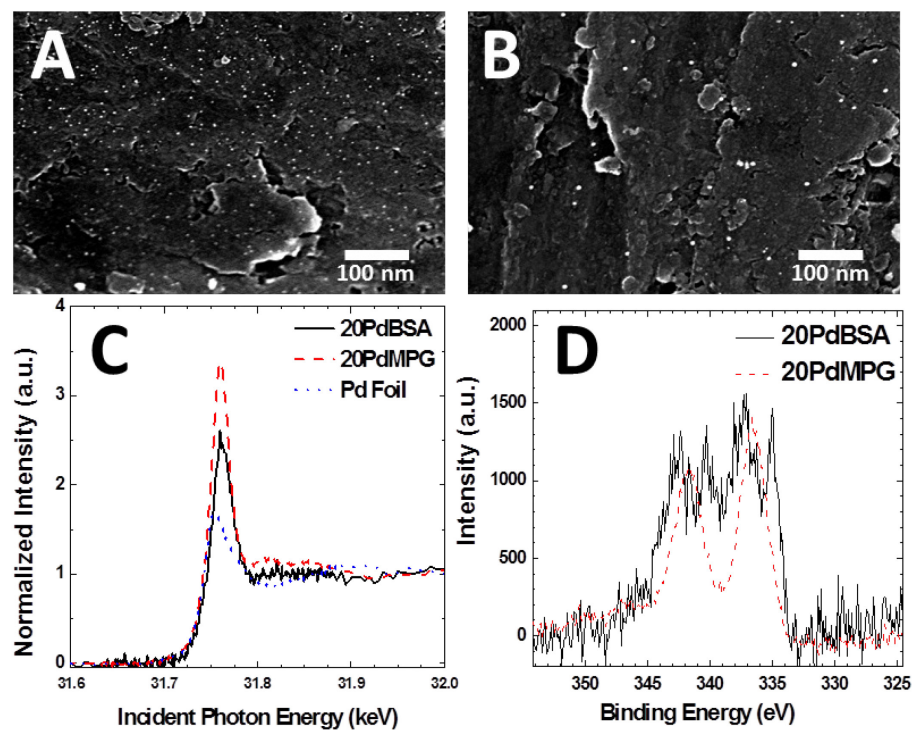


Figure 3-15. Scanning electron micrographs of bio-functionalized Pd nanoparticles on Ti substrate of (A) 20:1 Pd:BSA and (B) 20:1 Pd:MPG systems. Pd L_3 -edge XANES spectra (C) are shown of the 20PdBSA and 20PdMPG systems, as well as Pd foil for comparison. The Pd 3d XPS spectrum (D) denotes surface protection from oxidation in the 20PdBSA system.

A third system, Pd, was also determined to deposit NPs (Figure 3-15a and Figure 3-15b). The particle size is 8.5 ± 3.4 nm for the 20PdBSA system, and covers 1.9% of the surface, while the particle size is 10.0 ± 4.9 nm for the 20PdMPG system with 0.6% coverage. The low coverage may be explained by the difficulty in reducing Pd relative to Au and Ag. The white line intensities of both 20PdBSA and 20PdMPG nanoparticle systems are much larger than that of the bulk Pd foil, indicating a greater contribution of d-hole states (Figure 3-15c). When comparing both Pd NP systems, the white line of the 20PdMPG system is greater than that of the 20PdBSA system. This can be explained by Figure 3-15d, where the Pd 3d XPS of the 20PdBSA system shows Pd nanoparticles to consist of both oxidized and metallic Pd, while the XPS of the 20PdMPG shows only oxidized Pd. As the BSA-protein is more efficient at protecting the nanoparticle surface, it is reasonable to see a contribution of metallic Pd in the 20PdBSA XPS spectrum.

3.4 Summary

In this work, multi-element, multi-core X-ray spectroscopy methods were used to provide physical information of the atomic structure of metal NPs and the chemical interaction between NPs and biomolecules. A deposition procedure was improved to electrolessly amass and functionalize Au NPs nanoparticles with model biomolecules on the surface of a Ti substrate. Ag and Pd biomolecule-coated NPs were also prepared to observe differences due to changing metal composition. The biocompatible nature of Au NPs, and the anti-bacterial properties of Ag NPs, are essential properties for technologies in orthopaedic and bio-medical fields, hence requiring a better understanding. It is anticipated that the immobilization of bio-functionalized Au NPs onto Ti will be useful to improve

osseointegration of Ti-based implants in orthopedics; whereas the introduction of Ag NPs will add anti-bacterial functionality to Ti.^{107,191,192} These bio-coated metal NPs, immobilized on Ti, are therefore promising candidates for medical application.

CHAPTER 4 LIGAND EFFECT (PART 2)

Reproduced in part with permission from:
Christensen, S.L.; Chatt, A.; Zhang, P. "Peptide-Directed Preparation and X-ray Structural Study of Au Nanoparticles on Titanium Surfaces" *Langmuir*, **2013**, 29 (15), 4894-4900.
Copyright 2013 American Chemical Society.

4.0 Motivation

While the study described in Chapter 3 determined the difference in Au NP formation primarily based on ligand size, this study aims to compare ligand systems closer in size. Much was learned from the comparison of Au-BSA and Au-MPG systems, allowing us to better understand the formation and deposition of Au nanoparticles directed by both large and small ligands. Alternatively, the effect of ligands with very similar size, such as MPG and glutathione (GSH), an only slightly larger tri-peptide system, would provide insight into the effects of small changes in ligand size on supported Au NP formation. In order to observe such small changes in NP size and structure, a modified EXAFS technique was needed to maximize the signal-to-noise ratio.

4.1 Introduction

Au nanoparticles (NPs) functionalized with biomolecular ligands (DNA, peptides, proteins, etc.) have attracted much interest in the last decade, due to their promising applications in biosensing,⁸⁵ imaging,⁸⁶ photothermal therapy,⁸⁹ and drug delivery.⁹² For many technological applications, it is desirable to directly prepare functionalized NPs on the surface of a functional substrate.¹⁶⁹ However, techniques for the direct preparation of substrate-supported Au NPs are largely underdeveloped in comparison with their solution-phase counterparts,²¹ which allows for the precise tailoring of Au NP structure,

ranging from larger NPs of various shapes¹⁹³ to nanoclusters of precisely controlled compositions.²⁵ One reason for this under-development is that substrate-directed NP preparation is not as flexible as solution-phase chemistry. While NP structure can be efficiently controlled through NP-ligand interaction in solution-phase reactions, similar control is more difficult to achieve through NP-substrate interaction.

We have recently reported an electroless (galvanic) deposition method, whereby NP-ligand interactions are exploited as an extra means to produce structure-controlled metal NPs on a biocompatible substrate (Ti).¹⁰⁷ Ti is an ideal surface for studies of nanoparticle formation and deposition, as reduced Ti will readily reduce Au⁺ in solution, forming Au⁰ on the Ti surface.^{106,194} While there are other methods available for the functionalization of Ti surfaces with Au NPs (*e.g.* radio-frequency sputtering,^{100,101} chemical vapour deposition,^{102,103} *etc.*), the simultaneous formation of Au NPs coated with biomolecule systems (*e.g.* peptides) is a very attractive alternative to future biological application.^{106,107} Using Ti as a reducing agent has the added benefit of less solvent waste, providing a “greener” chemical approach for NP preparation than wet-chemical methods. Previously, Au NP samples functionalized with large biomolecules (bovine serum albumin) as well as a smaller system (N-(2-mercapto-propionyl) glycine, MPG), were deposited onto Ti substrates.¹⁰⁷ Due to the difficulty involved in acquiring Au L₃-edge EXAFS of low concentration systems, only determination of the coordination values and bond information for the 20:1 samples was possible. To further our studies, we present herein the peptide-directed synthesis of Ti-supported Au NPs, and their subsequent analysis using a improved surface-sensitive EXAFS technique. Using the tripeptide glutathione (GSH) and the pseudo-dipeptide MPG in a wide range of

metal:ligand molar ratios (20:1, 10:1, 5:1, and 2:1), eight Au NP samples were prepared. Moreover, using glancing-angle Extended X-ray Absorption Fine-Structure (EXAFS) spectroscopy with a rotating-stage setup, it was possible to resolve structural differences between these Au NPs that was not achievable in the previous study. The X-ray results show that by adjusting ligand concentration, Au NP structure in both systems can be controlled, generating larger NPs, nanoclusters, and Au-thiolate polymer, which is unique for substrate-supported NP synthesis.

4.2 Experimental

4.2.1 Synthesis

Reduced glutathione (GSH, 98%) was purchased from Fisher Scientific and N-(2-mercapto-propionyl) glycine (MPG, $\geq 98\%$) was purchased from Sigma Aldrich; both were used without further purification. 99.5% pure annealed titanium was purchased from Alfa Aesar, and was punched into 1 cm discs using the industrial hole-punch of the Mechanical Engineering Department at Dalhousie University. The discs were sonicated for ~ 5 minutes in acetone, sonicated in ethanol for another ~ 5 minutes, and finally sonicated once more for ~ 5 minutes in de-ionized water ($18.2 \text{ M}\Omega \text{ cm}^{-1}$, Barnstead NANOpure[®] DIamond[™] UV purification system). Concentrated HCl (36-38%, ACS Grade, Caledon)¹⁰⁷ was used to etch/refresh the Ti discs, removing the surface oxide layer.

Au:GSH and Au:MPG systems were prepared by combining the appropriate molar ratios of GSH and MPG with 10^{-4} M $\text{HAuCl}_4 \cdot 3\text{H}_2\text{O}$ (99.99%, Alfa Aesar). The Au-salt concentration remained constant across all samples, and the peptide (GSH or

MPG) concentration was varied. Solutions used for Au:GSH or Au:MPG samples were prepared in Au:peptide ratios of 1:0.05, 1:0.1, 1:0.2, and 1:0.5, or 20:1, 10:1, 5:1, and 2:1 samples, respectively. Samples were allowed to stir for two minutes,¹⁰⁷ at which time the etched titanium was rinsed with de-ionized water, and placed in the Au-salt/peptide solution. The Ti discs were removed from the salt/ligand solution, rinsed in de-ionized water, then dried and stored under argon gas. The details of this synthesis have previously been published.¹⁰⁷

The Au-thiolate polymer reference was prepared by reacting one equivalent of HAuCl₄ in tetrahydrofuran (THF) with two equivalents of dodecanethiol (~98%, Sigma) following a procedure presented in literature.¹⁹⁵ After precipitation, the polymer was collected and washed with ethanol.

4.2.2 Characterization

Nanoparticle morphology was determined using a Hitachi S-4700 FEG Scanning Electron Microscope at the Institute for Research in Materials at Dalhousie University. The images were captured with an accelerating voltage of 20 kV and emission current of 10 μ A, with a working distance of 6-7 mm.

The Au L₃-edge EXAFS (11919 eV) of the bare Au NP samples were acquired at the Canadian Light Source (CLS) in Saskatoon, SK, CA, using the Hard X-ray MicroAnalysis (HXMA – 06ID-1) beamline, using a wiggler insertion device as the incident photon source. The Au L₃-edge EXAFS of all other systems were acquired at the APS in Argonne, IL, USA using the PNC/XSD beamline (Sector 20), which uses a bending magnet as the incident photon source. All experiments were run in Fluorescence

Yield (FLY) mode at room temperature, at an incident glancing angle of $\sim 3^\circ$, with the samples attached to a rotating stage (~ 20 Hz) to ensure isotropic conditions, reduce damage, increase sampling area, and negate glancing-angle shadowing effects.

The EXAFS spectra were normalized and converted to k-space EXAFS, then Fourier Transformed to R-space EXAFS. All data processing¹⁶⁴ and EXAFS fitting¹⁶⁵ were done using the WinXAS program.^{163,166} The scattering path phase shifts and amplitude used to fit the EXAFS data were generated using the FEFF8.2 program.¹⁶⁸ The structural model of a 25 Au atom thiolate-protected cluster with known X-ray crystallographic coordinates was used to fit the first shell Au-Au and Au-S coordination shells.¹⁶⁵ It should be noted that only a selected EXAFS R-range was fit ($R = 1.5 - 3.3$), as this region pertains to the Au-S and Au-Au first shells. The 25 Au atom cluster was used as a good approximation for fitting the first shell Au-Au and Au-S features, though both this system and bulk gold have been used in the literature to achieve similar results.^{149,165}

4.3 Results and discussion

Figure 4-1 shows SEM images of the Au-GSH and Au-MPG systems, as well as a bare Au NP reference and plain Ti substrate. To simplify the naming convention, samples of varying composition and concentration will be referred to as nAuX, where n is the ratio value of Au to X is the peptide system (*e.g.* 20:1 Au-GSH is denoted 20AuGSH).

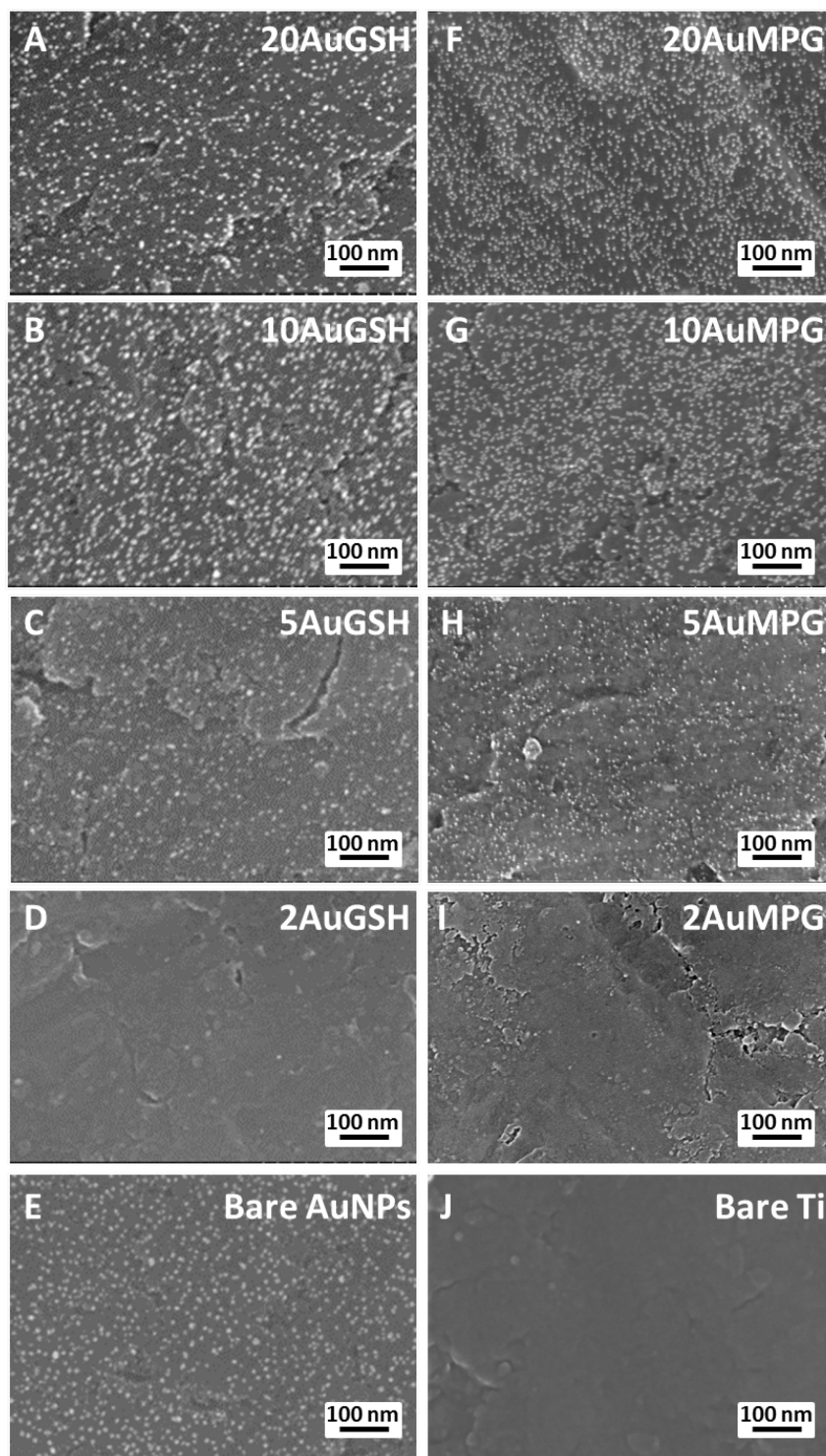


Figure 4-1. Scanning electron micrographs of the bio-functionalized AuGSH systems (A-D), AuMPG systems (F-I), and bare Au nanoparticles (E) on Ti substrate (100,000x magnification @ 20 kV). HCl-etched bare Ti (J) shown for comparative purposes.

As seen in Figure 4-1, the formation of Au NPs is clearly visible for the 20:1, 10:1, and 5:1 Au:ligand ratios for both the AuGSH and AuMPG systems. Generally, the surface coverage of nanoparticles is seen to decrease as the relative concentration of ligand in solution increases. In both AuGSH and AuMPG, the 2:1 Au:ligand ratio samples resulted in a lack of visible nanoparticle formation, most likely due to generation of very small nanoparticles. However, due to the limited resolution of SEM, no reliable information can be obtained on the size distribution of individual NPs, as the possible formation of aggregates convolutes data. Therefore, the NP structure will be studied using more reliable Au L₃-edge EXAFS measurements.

Figure 4-2A illustrates the modified EXAFS technique used to improve the signal-to-noise ratio of low concentration Au NPs. Glancing-angle Au L₃-edge EXAFS measurements allow a greater area of the Ti support to be sampled, as the shallow angle (~3°) effectively increasing the vertical spot size of the incident photon beam on the sample surface.^{196,197} By mounting the samples on a rotating stage, the EXAFS signal was averaged over a greater distribution of Au NPs, forcing isotropy, and minimizing damage.

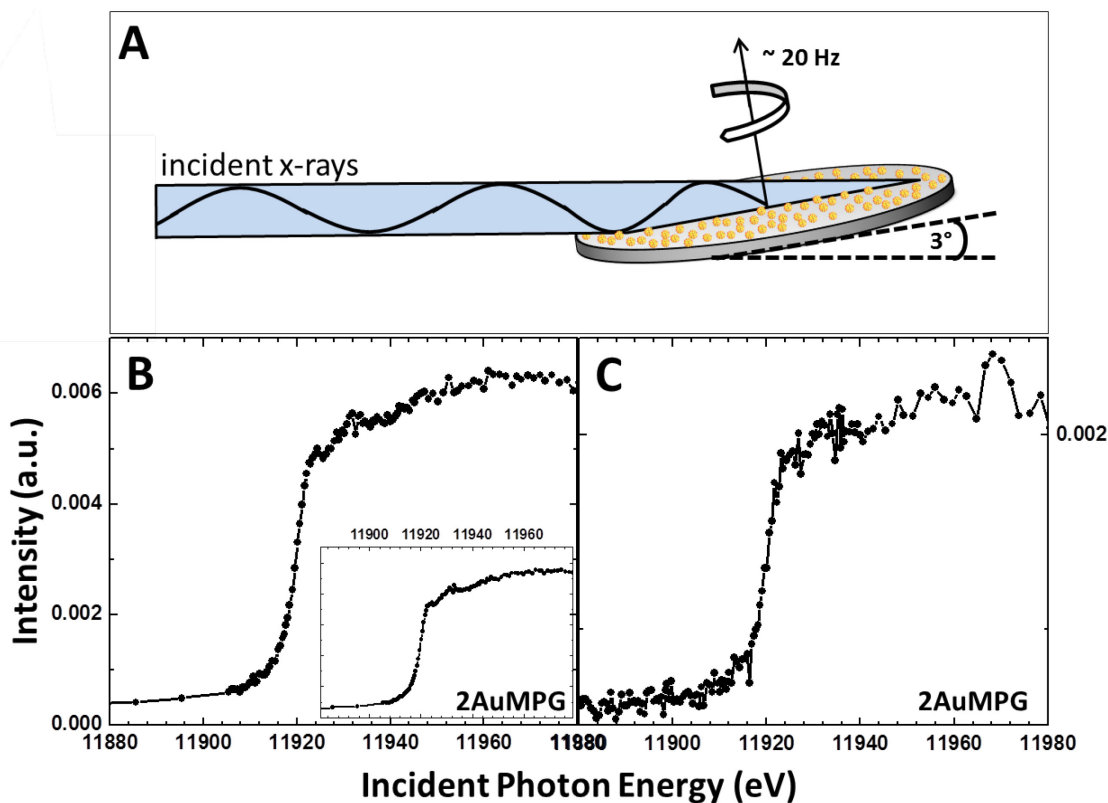


Figure 4-2. (A) Schematic detailing rotating sample plate setup used for glancing angle fluorescence EXAFS measurements, (B) Au L₃-edge XANES spectrum of 2AuMPG using spin method and (C) Au L₃-edge XANES spectrum of 2AuMPG without spinning the sample. Inset in (B) denotes signal after averaging several spectra. (Graphs are scaled for better comparison)

Figure 4-2B is a single scan of the Au L₃-edge X-ray absorption spectrum for the 2AuMPG system collected using this modified EXAFS technique (inset is averaged spectrum of multiple scans used for EXAFS fitting). In comparison, Figure 4-2C is the same sample and same glancing angle, without sample stage rotation. While the signal is low for both samples due to the low concentration of Au NPs on the Ti surface, it is evident that glancing-angle EXAFS with a rotating sample stage can greatly increase signal-to-noise ratio.

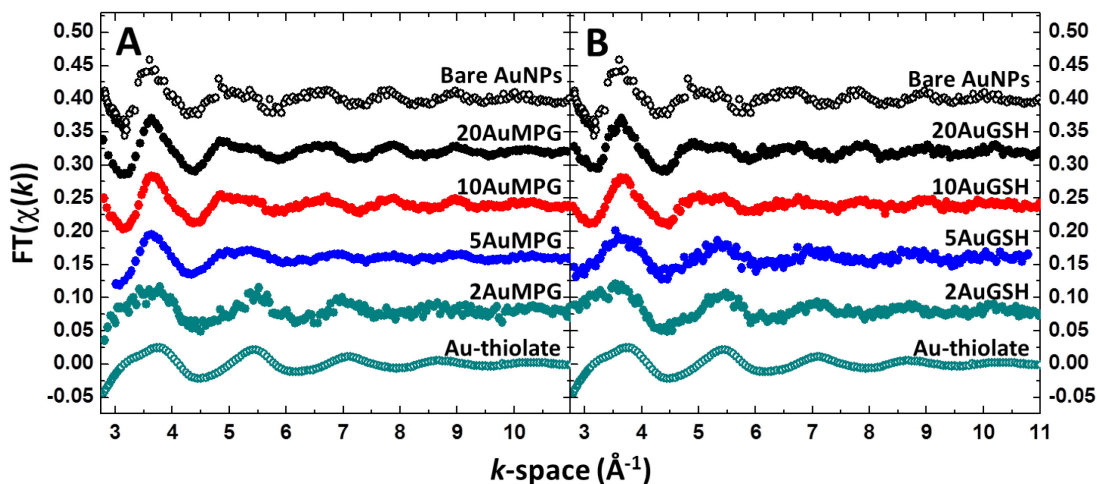


Figure 4-3. Experimental Au L_3 -edge k -space EXAFS spectra of the (A) AuMPG and (B) AuGSH systems, compared with bare Au NPs and Au-thiolate polymer samples.

Figure 4-3 shows the k -space EXAFS of the two series of Au-peptide NPs together with the reference samples (*i.e.* bare Au NPs and Au-thiolate reference). In Figure 4-3A, the k -space EXAFS oscillation patterns of both 20AuMPG and 10AuMPG samples are very similar to that of bare Au NPs, indicating they are FCC-structured. In contrast, the EXAFS of 2AuMPG sample follows the oscillation pattern of the Au-thiolate reference, suggesting the composition of this sample is mainly Au-thiolate polymer. Interestingly, the EXAFS oscillation pattern of 5AuMPG sample seems to be somewhere in between that of the bare Au NPs and the Au-thiolate reference. This observation implies that the 5AuMPG sample corresponds to small Au-thiolate nanoclusters, representing an intermediate stage of structural transition from FCC-nanoparticles (20AuMPG and 10AuMPG) to Au-thiolate polymer (2AuMPG).

In Figure 4-3B, it can be seen that the EXAFS oscillations of 20AuGSH and 10 AuGSH samples are also similar to that of bare Au NPs (like the 20:1 and 10:1 AuMPG samples). What is different for the 5:1 and 2:1 AuGSH samples, in comparison with their

AuMPG counterparts, is that neither of them shows EXAFS characteristic of an intermediate stage of structural transition (like 5AuMPG in Figure 4-3A). Instead, the EXAFS of both of these two samples are similar to that of the Au-thiolate reference.

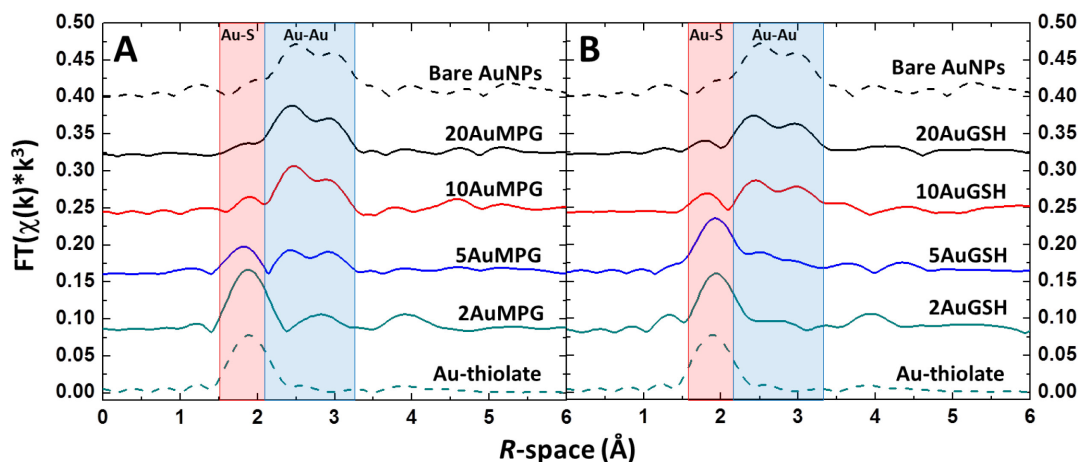


Figure 4-4. Experimental Au L_3 -edge R -space EXAFS spectra of the (A) AuMPG and (B) AuGSH systems, compared with bare Au NPs and Au-thiolate polymer samples. Red box denotes region of Au-S coordination shell, blue box denotes region of Au-Au coordination shell.

The Fourier-transformed Au L_3 -edge EXAFS of the AuMPG system with varying metal:ligand ratios are compared with those of bare Au NPs and the Au-thiolate reference (Figure 4-4A). The EXAFS feature in the region of ~ 1.5 - 2.3 Å represents the Au-S shell, while the feature in the ~ 2.2 - 3.3 Å region corresponds to the nearest Au-Au shell. When comparing the relative intensities of the Au-S shell amongst AuMPG samples, the intensity increases gradually with increasing ligand concentration, revealing a trend of 2AuMPG (0.087) > 5AuMPG (0.038) > 10AuMPG (0.025) > 20AuMPG (0.018). Simultaneously, the Au-Au shell decreases in intensity following the same trend (2AuMPG (0.004) < 5AuMPG (0.033) < 10AuMPG (0.067) < 20AuMPG (0.069)). When

we compare the spectra of AuMPG samples to those of the bulk Au NPs and Au-thiolate reference, we see that similar to Figure 4-3A, the 20AuMPG and 10AuMPG samples exhibit similarities to bare Au NPs, while the 2AuMPG sample is primarily of Au-S character, and therefore more similar to the Au-thiolate reference. The 5AuMPG sample exhibits moderate amounts of both Au-Au and Au-S features, denoting a very small particle with significantly more Au-S interaction than the larger 20AuMPG and 10AuMPG NPs.

As with the AuMPG system, Fourier-transformed Au L₃-edge EXAFS (Figure 4-4B) of AuGSH samples with varying metal:ligand ratios were also compared with bare Au NPs and the Au-thiolate reference. The Au-S shell becomes more intense in general with increasing ligand concentration (2AuGSH (0.081) > 5AuGSH (0.078) > 10AuGSH (0.030) > 20AuGSH (0.021)), with a simultaneous decrease in Au-Au shell contribution (2AuGSH (0.017) < 5AuGSH (0.030) < 10AuGSH (0.047) < 20AuGSH (0.055)). It is noted that the Au-S shell intensities for both the 5AuGSH and 2AuGSH samples are both very high, comparable to that of the Au-thiolate reference. The large Au-Au shell features of the 20AuGSH and 10AuGSH samples exhibit strong similarity to bare Au NPs. In comparison, due to the broad nature of the Au-Au shell, the Au-Au contribution is barely visible in the 5AuGSH and 2AuGSH samples. These observations are consistent with the findings presented in Figure 4-3.

It is worthwhile to qualitatively compare the EXAFS of the AuGSH and AuMPG systems, as any differences are due solely to the peptide-structure effect. The Au-Au shell of each AuGSH sample, when compared to the Au-Au shell of the corresponding AuMPG sample, is slightly reduced in intensity. This reduction means the AuGSH NPs

are smaller for each Au:ligand ratio than the equivalent ratio AuMPG NPs. Kinetically, due to the greater size of the GSH ligand, when compared to MPG (Figure 4-5),¹⁴³ further growth of the Au NPs is sterically hindered by Au-S bonded GSH, leading to smaller particles. In a similar fashion, the ligand concentration-dependent formation of Au NPs can be understood. When the ligand concentration is low (*e.g.* samples with 20:1 and 10:1 Au-ligand ratios), the peptide cannot efficiently prevent NP growth, resulting in the formation of large Au nanoparticles. Likewise, when the ligand concentration is increased, NP formation is governed by peptide structural differences. Therefore the 5AuMPG sample shows a moderate Au-Au shell, whereas that of the 5AuGSH sample is minimal. When the ligand concentration is even higher (2:1 Au-ligand ratio), the highly concentrated peptides can efficiently prevent the growth of even small Au clusters, which results in a surface consisting primarily of Au-thiolate polymer. These findings demonstrate that both ligand concentration and peptide-structure contribute significantly to the size and morphology of Au NPs formed on Ti surfaces.

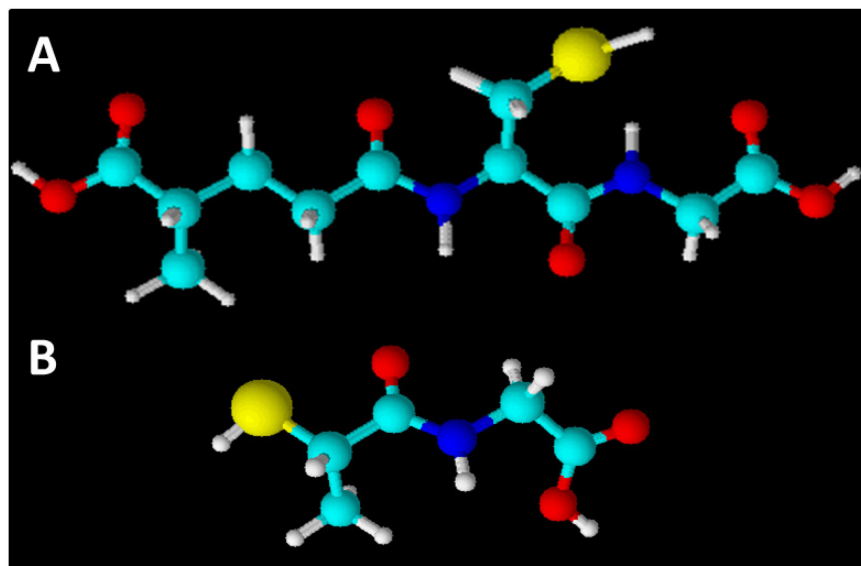


Figure 4-5. Molecular models of A) reduced glutathione (GSH) and B) N-(2-mercapto-propionyl) glycine (MPG) (yellow: sulfur, cyan: carbon, blue: nitrogen, red: oxygen, white: hydrogen)

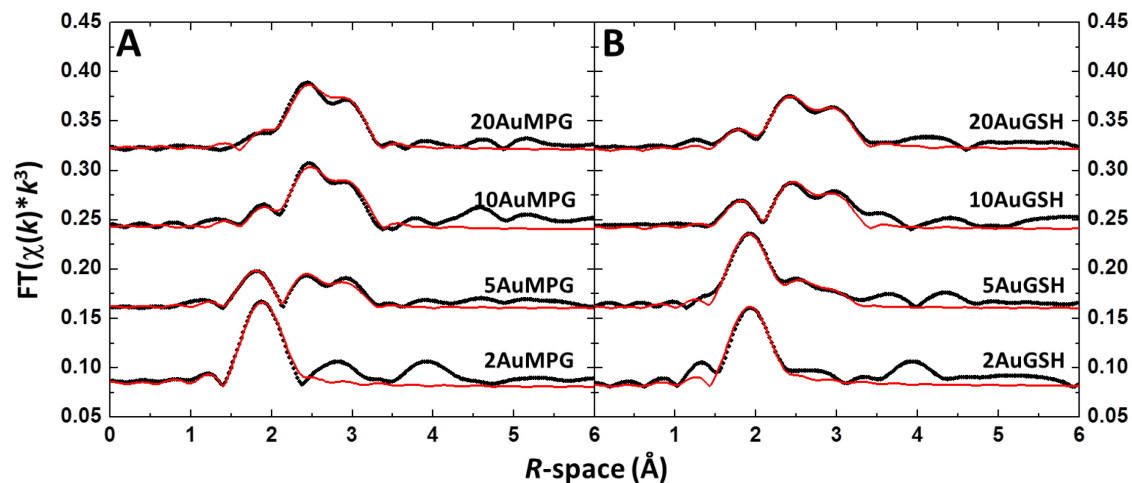


Figure 4-6. Experimental Au L₃-edge EXAFS spectra and fitting of the Au-S and Au-Au coordination shells for the (A) AuMPG and (B) AuGSH systems. (black: experimental data, red: best fit envelope)

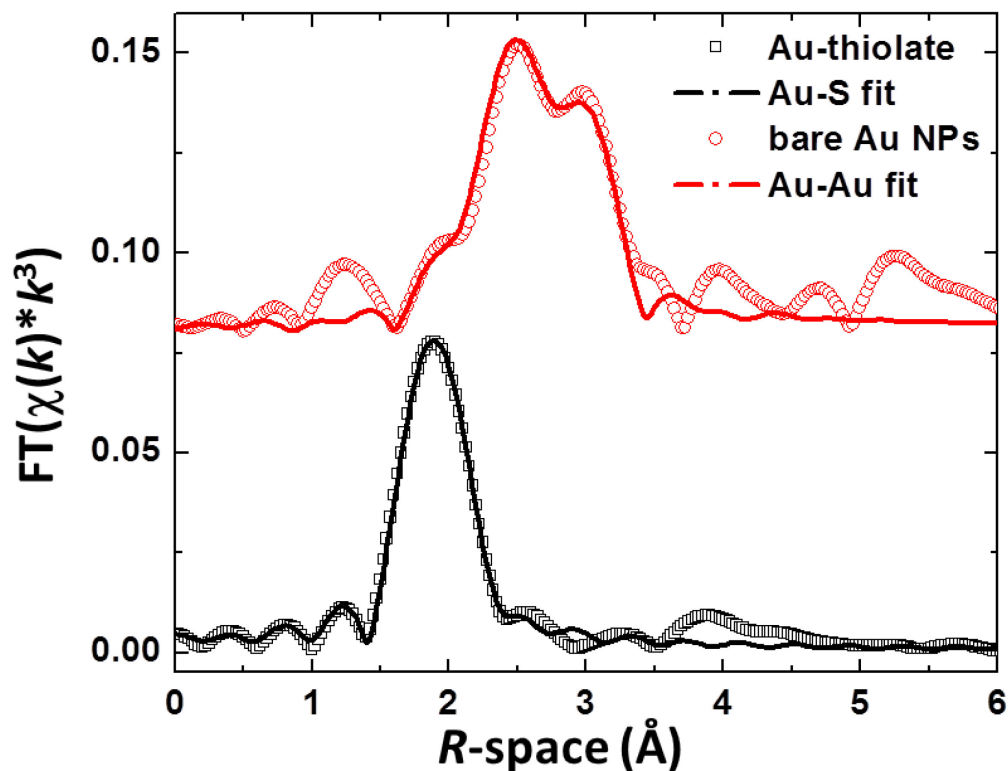


Figure 4-7. Experimental Au L₃-edge EXAFS spectra and fitting of the Au-S and Au-Au coordination shells for the bulk Au NP and Au-thiolate oligomer systems. (black: experimental data, red: best fit envelope)

In order to more quantitatively observe changes in coordination environment, the Au L₃-edge EXAFS Au-S and Au-Au shells for both AuMPG and AuGSH systems were fit. The best fits (R-factors < 0.03) are shown in Figure 4-6, while the resultant fit values are provided in Table 4-1.

Table 4-1. Au L₃-Edge EXAFS Fit Results for AuMPG, AuGSH, bare Au Nanoparticles, and Au-Thiolate Polymer Systems^{ab}

System	Path	CN	R / Å	$\sigma^2 / \text{Å}^2$	$\Delta E_0 / \text{eV}$
20AuMPG	Au-Au	11(1)	2.84(1)	0.009(1)	-1(1)
10AuMPG	Au-Au	10(2)	2.85(1)	0.010(2)	1(1)
5AuMPG	Au-Au	5(2)	2.83(1)	0.009(3)	-1(2)
	Au-S	0.9(5)	2.29(1)	0.002(5)	-1(2)
2AuMPG	Au-S	2.2(3)	2.30(1)	0.003(1)	-1(3)
20AuGSH	Au-Au	10(3)	2.85(1)	0.009(3)	-1(1)
	Au-S	0.4(7)	2.30(5)	0.004(3)	-1(1)
10AuGSH	Au-Au	7(1)	2.84(1)	0.007(1)	-1(2)
	Au-S	0.9(3)	2.31(2)	0.006(4)	3(4)
5AuGSH	Au-Au	1(1)	2.88(2)	0.0070(1)	-1(1)
	Au-S	1.9(4)	2.30(1)	0.002(2)	-1(1)
2AuGSH	Au-S	2.1(3)	2.32(1)	0.003(2)	1(1)
Bare Au NPs	Au-Au	11(1)	2.87(1)	0.009(1)	1(1)
Au-Thiolate	Au-S	1.9(1)	2.306(3)	0.002(1)	1(1)

^a S_0^2 fixed at 0.9, ^b brackets denote error

When comparing Au-S bonding across both systems, the Au-S bond lengths remain identical within the uncertainty (2.29 - 2.32 Å), consistent with our recent EXAFS results on Au-thiolate nanoclusters, such as Au₁₄₄ (2.34 Å),¹⁸⁵ Au₃₈ (2.32 Å),¹⁹⁸ Au₂₅ (2.32 Å),¹⁶⁵ Au₂₄Pt (2.32 Å),¹³² and Au₁₉ (2.32 Å).¹⁹⁹ When comparing Au-Au bond lengths, the larger 20:1 and 10:1 AuMPG and AuGSH systems are identical (2.84 - 2.85 Å), slightly shorter than that of bulk Au (2.88 Å). The shorter bond distance for these Au NPs can be attributed to lattice contraction commonly observed in small particles.¹⁸⁷ The Au-Au bond distance for the 5AuMPG sample is the shortest (2.83 Å) among these Au-peptide NPs. This value is the same as that of the Au₁₄₄ nanocluster, suggesting an even

smaller Au NP core size.²⁰⁰ Finally, the Au-Au bond distance in the 5AuGSH system is notably longer (2.88 Å) than other Au-peptide NPs (2.83 – 2.85 Å). This finding implies the Au-Au shell in this extremely small NP sample (Au-Au CN = 1), should consist of a large fraction of aurophilic Au-Au bonds (longer than metallic Au-Au distance), prevalent in Au-thiolate polymer systems. As for the 2AuMPG and 2AuGSH samples, no reliable Au-Au shell fit could be obtained due to its negligible intensity.

When comparing the Au-S and Au-Au CN values (Table 4-1), the fit data corroborate the qualitative observations, as there is an increase in the Au-S coordination contribution with a simultaneous decrease in the Au-Au coordination with increasing ligand concentration. In order to clearly demonstrate the overall trend in CN evolution, the Au-Au CN values of the two Au NP systems are shown in Figure 4-8.

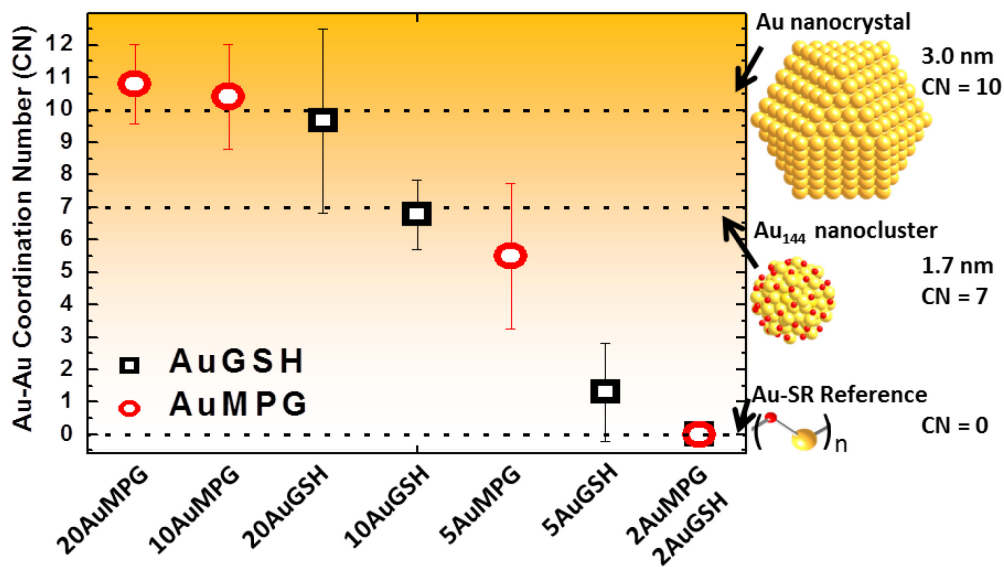


Figure 4-8. Plot of EXAFS-fitted Au-Au CN of AuGSH and AuMPG peptide-Au NPs. CN values for representative reference systems (Au FCC nanoparticles, Au₁₄₄ nanocluster, Au-SR Reference) are denoted by dotted lines.

It is evident that the size of the Au NPs range from larger Au NPs to nanoclusters to Au-thiolate polymer. Specifically, the 20AuMPG, 10AuMPG, and 20AuGSH all show apparent nanocrystalline structure, with the order of crystalline size being 20AuMPG > 10AuMPG > 20AuGSH. The 10AuGSH and 5AuMPG samples show Au-Au CN values similar to that of the Au₁₄₄ nanocluster^{200,201} and can be considered as nanocluster systems, with the size of 10AuGSH being greater than that of 5AuMPG. The 5AuGSH, 2AuGSH, and 2AuMPG samples exhibit a Au-thiolate polymer-like structure, although there may be a small amount of nanoclusters co-existing (for example 5AuGSH). The trend in CN values presented in Figure 4-8 clearly shows the correlation between ligand concentration and peptide structure with resultant nanoparticle size. These results also demonstrate the capability of the peptide-directed method, in conjunction with Ti-based electroless deposition, in producing Au NPs with a wide range of sizes. We have also preliminarily tested Au NPs adhesion to Ti surfaces, determining that the NP-substrate interaction is sufficiently strong to survive sonication (20 minutes).

It should be noted that the control of composition and monodispersity of Au NPs prepared in this work, while promising for substrate-supported NP systems, is not as comparable as the very high precision in the composition control of Au-thiolate NPs synthesized in solution phase (e.g. nearly 100% compositional purity for Au₁₄₄).⁶¹ Possible approaches could be used for future experiments to further improve the structure control of these substrate-supported Au-peptide NPs, such as using a larger selection of peptides with desired structure, or slowing the reduction of Au salt onto the Ti surface by control of temperature and solvent.

4.4 Summary

In conclusion, we have presented a facile preparation of Au-peptide NPs on Ti surfaces, and used a modified surface-sensitive EXAFS technique to study the structure and bonding of the NPs. Using a rotating-stage glancing-angle EXAFS technique, it was possible to gain structure and bonding information of supported Au NPs with low coverage. Due to this modification, the signal-to-noise ratio was improved enough to enable the fitting of Au-Au and Au-S shells for even the most low coverage samples, something unattainable in our previous study. Furthermore, the study elucidated the effects of peptide concentration and molecular structure on the reaction kinetics of NP formation, as the interplay between concentration and peptide bulk are key to particle formation and growth. Finally, functionalization of Ti surfaces was accomplished with peptide-Au NPs of a variety of sizes, including larger NPs, nanoclusters, and Au-thiolate polymer. These peptide-Au functionalized Ti surfaces may find possible applications in biotechnologies due to the biocompatible nature of Au NPs, peptides, and Ti substrates.

CHAPTER 5 METAL EFFECT (PART 1)

5.0 Motivation

Having studied the ligand effect in Au NP-ligand interactions, it was then undertaken to study these systems from the perspective of the metal effect. For these studies, well-defined models of the Au₁₀₂ and Au₂₅ systems were compared, both of whose structures have previously been crystallographically determined. A site-specific comparison of Au NP-ligand structure, local environment, and electronic changes with varying NP size are carried out using ab initio calculations. In this chapter, very small Au NPs with precise compositions (i.e. Au₂₅ and Au₁₀₂) were referred to as Au nanoclusters (Au NCs).

5.1 Introduction

Small gold-thiolate nanocluster samples (< 2 nm in diameter), of interest due to recent discoveries regarding interactions between surface gold atoms and their surrounding ligand-contributed thiol groups.^{28,52,64,202} The electronic properties of such nanoclusters are dependent on the size, elemental composition, structure, and supporting ligand system.^{21,28,149,202–205} Unlike larger nanoparticles, these nanoclusters exhibit unusual electronic properties and surface functionalization.^{52,72,149,203} While the mechanism of nanocluster thiolate-protection was previously thought to resemble that of larger nanoparticles (> 2 nm),²¹ recent DFT calculations and crystal structures suggest the incorporation of ligand-sulfur into the Au nanocluster by the Au nanocluster surface

atoms, conversely distancing the bound Au atoms from the surface in a $-\text{SR}-(\text{Au-SR})_x-$ “staple”-like arrangement, where $x = 1, 2,$ or 3 (Figure 5-1).^{28,52,64}

Au nanoclusters exhibit interesting optical^{64,72,205,206} and electronic properties,^{21,149,203,204} leading to uses in catalysis^{84,207} and drug delivery,^{90,208} among many others. Though the stoichiometries of many gold nanoclusters have been determined by mass spectrometry,^{61,63,73,153,209,210} it is only recently that the structures of a few systems have been determined using X-ray crystallography.^{28,52,65} Two of these crystallographically determined systems, the phenylethanethiol-capped $\text{Au}_{25}(\text{SCH}_2\text{CH}_2\text{Ph})_{18}^-$ system (referred to as Au_{25}^-),⁵² and the mercaptobenzoic acid-capped $\text{Au}_{102}(\text{MBA})_{44}$ (referred to as Au_{102}),²⁸ exhibit similar surface organization (Figure 5-1). In the Au_{25}^- system, the phenylethanethiol ligands bind to surface gold atoms and form six “double-staples” surrounding a 13-atom icosahedral core, stabilizing the cluster.⁵² The Au_{102} system is more complex, using the MBA ligand to form single-staples, double-staples, and double-anchor staples.²⁸ As the double-staples are common to both models, their study presents an opportunity to compare the effect of size on ligand-surface organization and its subsequent electronic properties.

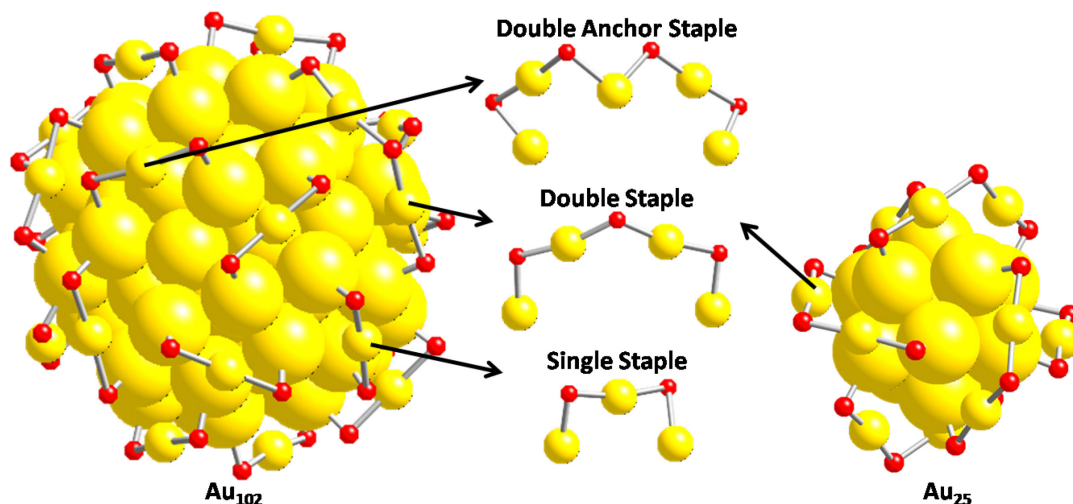


Figure 5-1. Au₁₀₂ and Au₂₅⁻ models showing the double anchor, double staple, and single staple bonding motifs.

To better understand the electronic properties of these double-staple systems, it is important to understand both the surface effect and the effect of the aurophilic interaction (a long-distance interaction between surface Au and staple Au atoms).^{29,34,37-39} By performing *ab initio* calculations¹⁶⁸ using the internal coordinates of the crystal structures for the Au₂₅⁻ and Au₁₀₂ systems, the double-staple bonding motif can be examined on a site-specific basis, a task not previously possible. The *ab initio* code (FEFF 8.2) is capable of calculating the theoretical local densities of states (*l*-DOS) and EXAFS of these staple structures, allowing for the site-specific calculation of charge transfer, orbital electron occupation, and local coordination environment.¹⁶⁸

In this work, charge transfer and the orbital electron occupancy are used to calculate differences in the electronic properties of the Au₂₅⁻ and Au₁₀₂ double-staple structures. These differences are then related to aurophilic interactions and electronic

character. A better understanding of the bonding and local environment in such nanoclusters may lead to more accurate predictions of ligand-surface organization, electronic character, and structure in nanoclusters which prove difficult to crystallize.

5.2 Experimental

FEFF 8.2 is an *ab initio* self-consistent multiple-scattering code, used to simulate the fine-structure present in XAS spectra and electronic properties. Calculations of *l*-DOS were performed in order to compute the energy distribution of electrons and holes in the Au₂₅⁻ and Au₁₀₂ nanoclusters. All *l*-DOS calculations were normalized to a calculated Fermi level energy for the corresponding sample. Bond lengths and aurophilic distances were determined using the CrystalMaker® modelling software package. The crystal structures of the Au₁₀₂ and Au₂₅⁻ nanoclusters were used to determine the nearest-neighbouring coordination environments.

Au L₃-edge EXAFS calculations on the Au₁₀₂ double-staple structure were carried out using the crystallographic coordinates of Au₁₀₂ provided by the Kornberg group.²⁸ Au₁₀₂ consists of a seventy nine Au atom core, with decahedral symmetry, surrounded by twenty three capping Au atoms. The thiol groups of 44 para-mercaptobenzoic acid (MBA) ligands are incorporated into staple-like structures, resulting in the surface Au atoms being distanced from the cluster. The staple structures alternate S and Au atoms, forming single-staples, double-staples, and double anchor staples (Figure 5-1).²⁸ Due to the lower symmetry of these models the electronic environments of all double-staples on the Au NPs are not equivalent. Thus, it was necessary to simulate and average the Au L₃-edge EXAFS k-space spectra for each site, prior to Fourier-transformation.

Computational Au L₃-edge EXAFS calculations were also carried out on the Au₂₅⁻ cluster. The internal coordinates used for the site-specific calculations were provided by the Jin group, having been previously determined via X-ray crystallography.⁶⁹ The staples are formed through the incorporation of thiol groups from the eighteen phenylethanethiolate (SCH₂CH₂Ph) capping ligands into the staple structure (Figure 5-1). The EXAFS calculations included all Au and S atoms, as well as including the S-bound C atom from each ligand.

Averaged sulfur K-edge R-space EXAFS were Fourier-transformed over a k-range of 3 to 8 Å⁻¹. As Au-S coordination in the double-staples of both the Au₂₅⁻ and Au₁₀₂ nanoclusters is 2, change in the EXAFS spectra can be considered a function of relative inter-atomic distances. The k-space EXAFS spectra in this study are non-phase corrected, therefore after Fourier-transformation the resultant spectra are plotted in terms of their pseudo-radial function (R-space).

5.3 Results and Discussion

5.3.1 Local Coordination Environment

Simulated EXAFS is useful, as it illustrates the difference of local environment in the context of interaction between the probed atom and its nearest neighbours.

Furthermore, simulated EXAFS provides a guideline for further experimental EXAFS studies of local structure in Au-thiolate nanostructures.

The range chosen for Fourier transformation of EXAFS k-space spectrum largely dictates feature resolution in the resultant R-space spectrum, as well as intensity-weighting of the nearest-neighbouring shells. When shorter ranges of the k-space

spectrum are chosen for Fourier-transformation, the signal is biased towards the nearest-neighbouring shell, overemphasizing the signal from those atoms nearest to the site of interest (*i.e.* the photoelectron emitter). Longer k-ranges tend to under-emphasize the signal from the smaller bond length nearest-neighbouring atoms, thus misrepresenting the feature intensity of more long-range atom interactions.

Figure 5-2 depicts the Au L₃-edge EXAFS R-space spectra of Au₁₀₂ after Fourier-transformation of the k-space spectrum over different ranges. The k-weight of the FT is fixed at k³ for the Au L₃-edge EXAFS of these samples. As the quality of the experimental data dictates the useable k-range, a k-range maximum of 16 Å⁻¹ was used for all computational work as it provided better feature resolution than $\Delta k = 2.5\text{-}12 \text{ \AA}^{-1}$, while reducing the signal contribution from the more distant neighbors and multiple scattering contributions brought on by higher k-values.

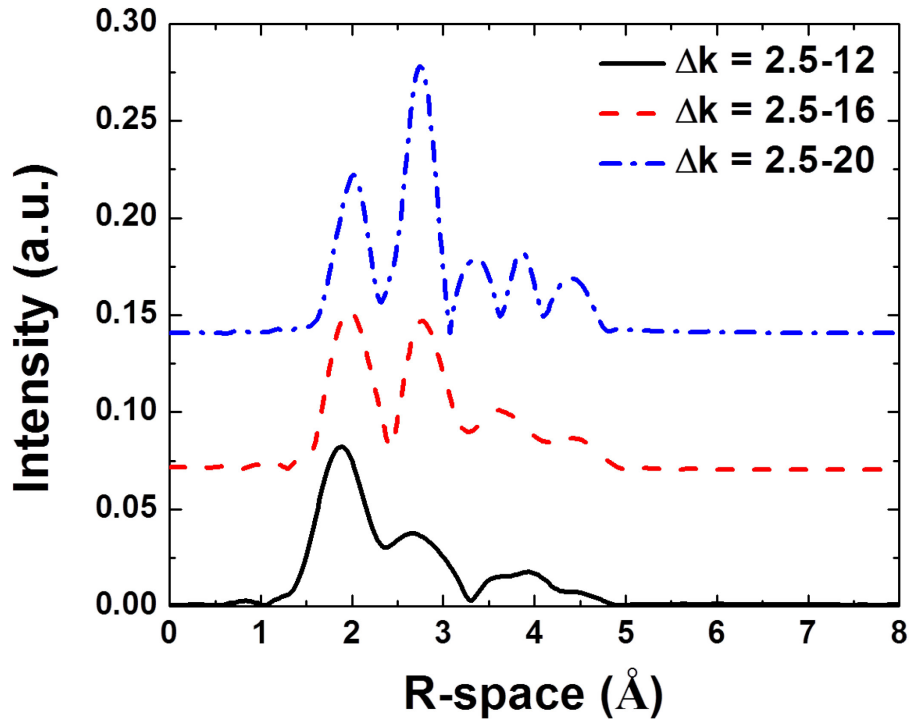


Figure 5-2. Averaged Au L₃-edge EXAFS of Au₁₀₂ after Fourier transformation over different ranges in k-space. Spectra were normalized to Au-S peak at ~1.9 Å for comparison.

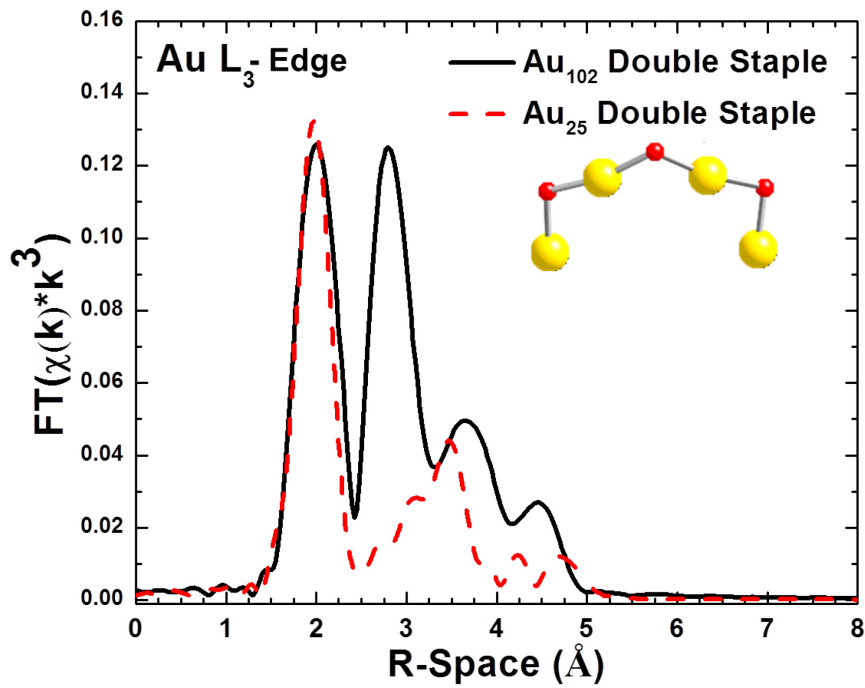


Figure 5-3. Comparison of averaged Fourier-transformed Au L₃-edge EXAFS of Au atoms in Au₁₀₂ and Au₂₅⁻ double-staple motif.

Comparing the Au L₃-edge EXAFS R-space spectra of the local double-staple environments on the Au₁₀₂ and Au₂₅⁻ nanoclusters, there is a similarity in the structure of the double-staple, indicated by the comparable Au-S features seen at 2 Å in Figure 5-3. This similarity is expected, as the bent double-staple geometry has also been observed in other Au nanocluster species, and is of a similar orientation.^{28,52,64,65,78} The aurophilic interaction seen in Figure 5-3 (Au-Au at 3-4 Å) is the bonding of staple-bound Au atoms to their nearest surface gold neighbours. As is evident in Figure 5-3, the degree of Au-Au bonding in the Au₁₀₂ and Au₂₅⁻ species differs remarkably. The large peak at 2.75 Å in the Au L₃-edge EXAFS R-space spectrum occurs at the averaged aurophilic distance between the four Au atoms in the Au₁₀₂ double-staples and their nearest-neighbour surface Au atoms. In comparison, there are three distinct peaks for the double-staple structures of the Au₂₅⁻ system, as small TOA⁺-induced symmetry differences lead to three different aurophilic interaction peaks at 2.7 Å, 3.0 Å, and 3.4 Å. This is further supported by X-ray crystallographic results, which show Au₂₅⁻ to be slightly oblong in shape. The features at 3.75 Å and above are due to multiple scattering effects and longer range interactions, and are not pertinent to this analysis.

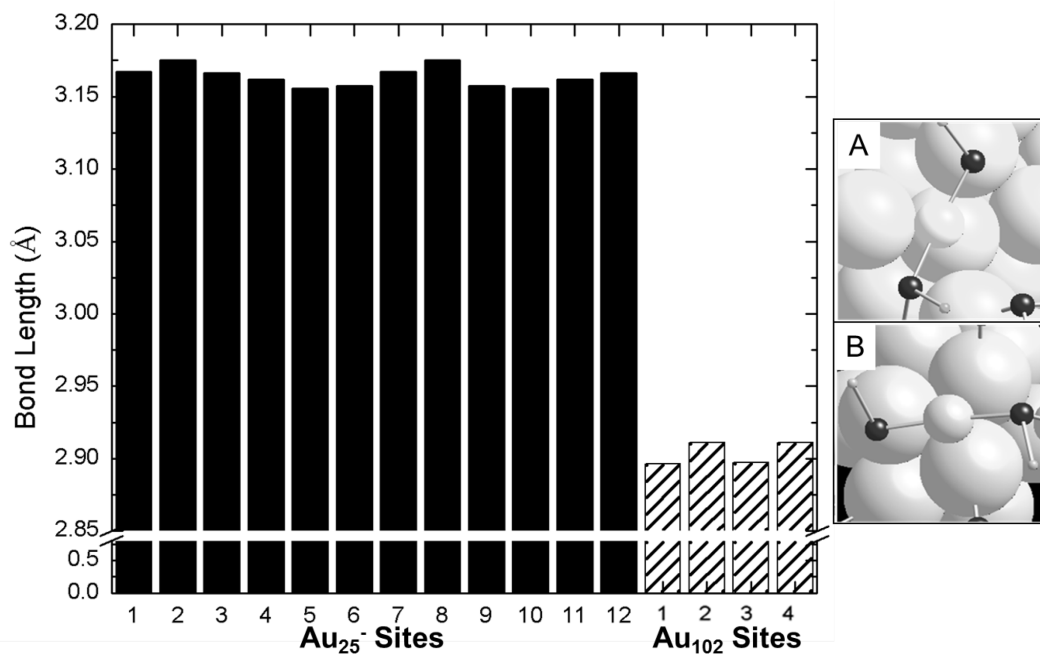


Figure 5-4. Nearest three Au-Au aurophilic interactions and their average for the A) Au₁₀₂ and B) Au₂₅⁻ systems.

Figure 5-4 depicts the analysis of aurophilic interaction distances measured using the Au₁₀₂ and Au₂₅⁻ crystal structure coordinates. The differences within the three nearest-neighbouring Au-Au interaction distances is due to the symmetry of the nanoclusters, and it is for this reason they were averaged. The average distance of aurophilic interactions are ~ 3.16 Å in the Au₂₅⁻ nanoclusters, and ~ 3.04 Å for the Au₁₀₂ nanoclusters, meaning that the Au₂₅⁻ double-staple systems are further from the cluster surface than those of the Au₁₀₂ nanocluster.

5.3.2 Electronic Properties

When comparing the staple structures, it is important to understand the relation between aurophilic distances, local environment of the staple structure, and electronic properties of the Au NC. Calculations of *l*-DOS were performed on the staple Au atoms from Au₁₀₂ and Au₂₅⁻ double-staple systems. The s-electron counts were calculated and averaged over all double staple Au atoms in each cluster, and were determined to be 0.92 in both cases, suggesting that the s-electron interactions are similar.

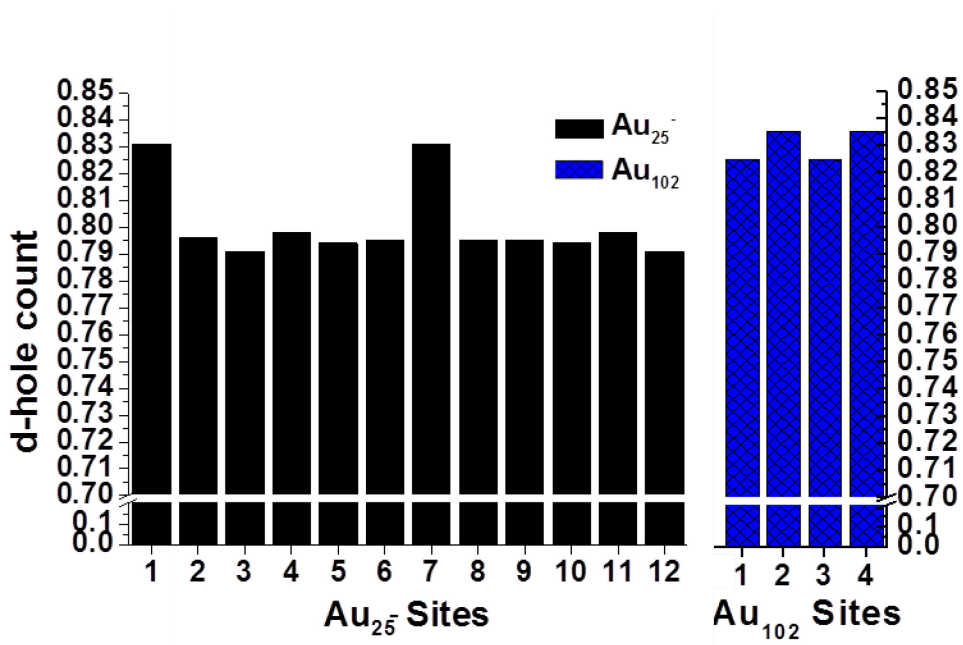


Figure 5-5. Graph of d-hole counts for the staple Au centres in Au₂₅⁻ and Au₁₀₂.

Figure 5-5 depicts the number of d-orbital electron holes (d-holes). The higher number of d-holes in the Au₁₀₂ nanocluster, when compared to that of Au₂₅⁻, suggests charge transfer of d-electron density from the double-staple to the surface. The two Au₂₅⁻ sites with large d-hole counts (denoted as site 1 and site 7) are the sites closest to the TOA⁺ ammonium cation used to mediate crystallization (Figure 5-6). These TOA⁺ groups are also responsible for the distortion of the Au₂₅⁻ nanocluster. The p-electron count calculated for staple Au atoms in the Au₂₅⁻ species averages to 0.67, and 0.74 in the Au₁₀₂ species. The average d-electron counts for the double-staple Au in the Au₂₅⁻ and Au₁₀₂ species were calculated to be 9.20 and 9.17, respectively. The differences seen in the p and d-electron counts are most likely due to electron re-arrangement, as a decrease in p-electron density correlates with an increase in d-electron density for the Au₂₅⁻ system, while the opposite is true in the Au₁₀₂ system. The greater d-electron count in the Au₂₅⁻ system suggests a significant difference in electronic character relative to the Au₁₀₂ system, which is consistent with increasing nanoparticle size.²¹ This is of interest as it is not clear to what degree the staple-structure of small nanoparticles affects their overall electronic character, as their atomic packing is quite different from that of bulk gold or even larger nanoparticles.^{21,211}

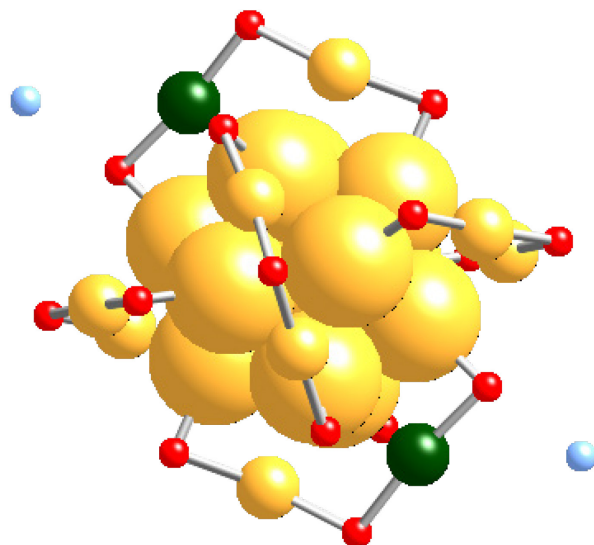


Figure 5-6. Crystal structure of Au_{25}^- nanocluster. Yellow atoms are Au, red are sulfur (additional ligand atoms are removed for clarity), blue are N (from TOA^+), and green are the two staple-Au sites most strongly affected by TOA^+ .

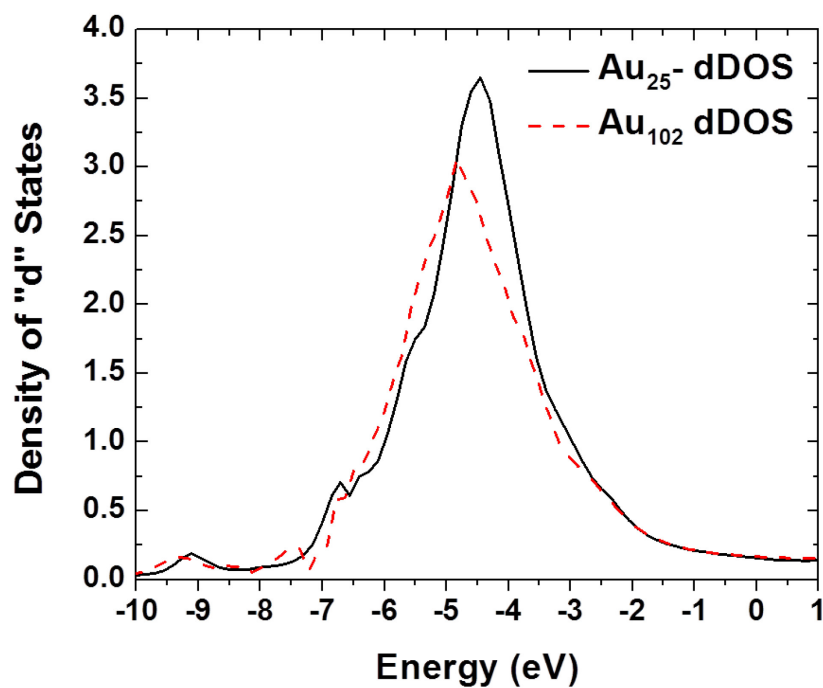


Figure 5-7. Distributions of averaged d-electron density of states (d -DOS), for double-staple Au in the Au_{102} and Au_{25}^- nanoclusters. The Au_{102} d -DOS was 3-point smoothed to facilitate the comparison.

The d-electron density of states (*d*-DOS) was calculated in order to compare the distribution of d-electron states of Au in the Au₂₅⁻ and Au₁₀₂ systems. As is evident in Figure 5-7, there is a slight shift towards lower energies for the d-states in the Au₁₀₂ system. This shift is due in part to charge transfer and a shorter Au-Au aurophilic distance. This shorter distance results in the reduction of charge transfer seen in metal-metal interactions, which leads to a negative shift in energy of the *d*-DOS distribution.

Bond length and charge-transfer calculations were carried out in order to test the previously determined *l*-DOS results. The charge transfer from the ligand carbon to sulfur was found to be negative, indicating it is electron withdrawing. The bond length between the staple sulfur and the ligand carbon averaged 1.84 Å for the apex sulfur atom in the Au₂₅⁻ double-staple and 1.80 Å for the Au₁₀₂ apex sulfur atom, while the charge transfer to sulfur was 0.14 and 0.09 respectively. The average of the double-staple corner sulfurs for the Au₂₅⁻ and Au₁₀₂ were 1.83 Å and 1.80 Å, respectively. Charge-transfer from the double-staple gold atoms was calculated to average 0.21e⁻ in Au₂₅⁻, and 0.17 e⁻ in Au₁₀₂. The smaller charge transfer for the Au₁₀₂ double-staple system, along with the longer Au-S bonds, suggest overall that the double-staple system in the Au₁₀₂ nanocluster is capable of carrying more electron density than that of Au₂₅⁻, and confirm the conclusions determined from *l*-DOS calculations.

5.4 Summary

Using the X-ray crystallographic coordinates of the Au₁₀₂ and Au₂₅⁻ nanoclusters, site specific Au L₃-edge EXAFS and *d*-DOS calculations were used to compare and

contrast their local coordination environments and electronic properties. The comparison of staple system bonding in both Au₁₀₂ and Au₂₅⁻ suggests the staple structures to be very similar, while the differences in the Au-Au interaction geometry exhibits unique local coordination environments.

Charge transfer and *I*-DOS calculations show the differences between the two systems, suggesting that size effects may play a role in the electronic character of the Au₁₀₂ and Au₂₅⁻ systems and confirming local coordination environment and electronic character to be contributing factors. There is also evidence that charge redistribution in the p and d-orbitals is responsible for the changes seen in the charge transfer calculations. As more nanocluster structures are crystallographically determined, site-specific calculations of electronic character and local coordination environment will aid in understanding these systems, and determining what causes staple formation to cease in larger nanoparticles. A better understanding of the staple structure may lead to better predictions of structures for Au-thiolate nanoclusters which have yet to be determined.

CHAPTER 6 METAL EFFECT (PART 2)

Reproduced in part with permission from:
Christensen, S.L.; MacDonald, M.A.; Chatt, A.; Zhang, P.; Qian, H.; Jin, R. “Dopant Location, Local Structure and Electronic Properties of Au₂₄Pt(SR)₁₈ Nanoclusters” *The Journal of Physical Chemistry C*, **2012**, *116* (51), 26932-26937.
Copyright 2012 American Chemical Society.

6.0 Motivation

Finally, a comparison of metal effect on Au NP-ligand bonding is studied by varying the composition of the Au₂₅ structure by single-atom Pt-doping. Using EXAFS, the location of Pt in the Au₂₅ structure can be established, and used to study the effect of heteroatom-doping on the Au₂₅ NP. As with Chapter 5, Au NPs less than 2 nm (i.e. Au₂₅ and Au₂₄Pt), will be referred to as Au NCs.

6.1 Introduction

Au nanocluster systems are of great interest, due their unique structures and high surface area-to-bulk ratio.^{11,21,203} These nanoscale systems, being less than ~2 nm, exhibit unique properties due to quantum-confinement of their electrons, leading to quantized energy levels.^{11,21,203} Unlike their bulk metal counterparts, the high ratio of reactionary surface-to-bulk, as well as the molecular-like character of these metal systems, allows for interesting catalytic,^{21,42,70,84,194,207} optical,^{21,72,206,212} and magnetic properties.⁴⁸

For Au nanocluster systems passivated by thiol-containing ligands, sulfur atoms are incorporated into the nanocluster, distancing surface Au atoms from the core, creating a “staple-like” protecting layer.^{52,64,165} In systems such as Au₂₅(SR)₁₈, henceforth referred to as Au₂₅, three coordination environments are formed; a center Au site, twelve surface

Au sites, and twelve Au atoms in the staple sites.^{52,64,149,165,202} Having a high quasi- D_{2h} symmetry, the Au_{25} nanocluster systems are more stable than pure Au nanoclusters of similar size.²¹³ It can therefore be synthesized with relatively high purity and quantity, as synthetic procedures have been continuously optimized.^{53,69,78}

While the Au_{25} nanocluster system is indeed interesting, doping the system with a heteroatom metal provides an exciting opportunity to fine-tune the properties of these nanocluster systems.^{49,77,81,116,214–219} Previous studies by Fields-Zinna *et al.*²¹⁶ have determined that, when doping Au_{25} with Pd, the resultant system will be $Au_{24}Pd(SC_2H_4Ph)_{18}$, regardless of the ratio of Au to Pd used in the synthesis. Furthermore, Negishi *et al.*⁷⁷ have managed to successfully isolate $Au_{24}Pd(SC_2H_4Ph)_{18}$, and Qian *et al.* have now managed to do the same with Pt, creating $Au_{24}Pt(SC_2H_4Ph)_{18}$, henceforth referred to as $Au_{24}Pt$.⁴⁹ As there is currently no crystal structure available for these doped nanoclusters, there remains a challenge in determining the exact location of the dopant atom, as well as their structure-property relationship.

The elemental specificity of EXAFS spectroscopy makes it an ideal tool for the study of local structure in bimetallic nano-systems.^{50,220} Using EXAFS spectroscopy, it is possible to determine the location of the Pt-dopant, via determination of the dopant coordination number (CN).^{165,221} Moreover, it can provide insight into changes in local bonding environment by accurate analysis of bond distance (R).⁵⁰ Combined use of EXAFS with X-ray photoelectron spectroscopy (XPS) enables us to further understand the Pt-atom doping effect on the structure and electronic properties of Au_{25} .^{149,160} Herein, we report our results regarding dopant location, local structure, and electronic properties of the $Au_{24}Pt$ nanocluster obtained from EXAFS, XPS, and *ab initio* calculations.

6.2 Experimental

6.2.1 Synthesis and Mass Spectroscopy Characterization

Details of the synthesis have been recently published.⁴⁹ The as-prepared $\text{Au}_{24}\text{Pt}(\text{SCH}_2\text{CH}_2\text{Ph})_{18}$ clusters were characterized by positive mode matrix-assisted laser desorption (MALDI) mass spectrometry to ensure the product composition.

6.2.2 X-ray Spectroscopy and Calculations

X-ray photoelectron spectroscopy (XPS) was conducted using the Spherical Grating Monochromator (SGM) beamline at the Canadian Light Source, Saskatoon, SK. Both Au_{24}Pt and Au_{25} systems were re-dissolved in toluene, and drop cast onto carbon tape. Nickel mesh was placed over the sample to prevent charging under X-ray irradiation. Samples were mounted on the same sample holder, along with a Au foil, so as to ensure identical experimental conditions. All experiments were acquired with an incident photon energy of 700 eV, and were carried-out at low temperature (60-70 K) so as to reduce damage to the samples. The binding energies were all calibrated by the Au $4f_{7/2}$ peak of Au foil. Fitting of the XPS spectra was carried out using CasaXPS v2.3. The Au_{24}Pt system XPS survey scan was acquired with an incident photon energy of 1000 eV.

Au and Pt L_3 -edge EXAFS measurements of the Au_{25} and Au_{24}Pt systems were conducted using the PNC/XSD bending magnet beamline at the Advanced Photon Source, Argonne National Laboratories, Argonne, IL, using a Si (111) crystal monochromator. The Au_{25} sample was dissolved in toluene, drop-cast onto polyimide (Kapton[®]) tape, dried, and were folded until an optimal transmission signal strength was

achieved ($\Delta\mu_0 \approx 0.5-1.1$). The Au and Pt L₃-edge EXAFS spectrum of Au₂₄Pt was acquired in fluorescence-yield mode (FLY) using a 12-channel fluorescence detector.

Using the previously determined crystalline structure of Au₂₅ (Figure 6-2)^{52,64}, the ab-initio code FEFF8.2 was used to calculate the EXAFS phase and amplitude data, as well as angular momentum and local density of states (*I*-DOS).^{149,168} The IFEFFIT software suite,¹⁶⁷ designed for XAS data analysis and fit refinement, was used to fit the experimental spectra with the simulated shell data using a standard procedure.^{165,185}

Au L₃-edge EXAFS spectra were refined, and a Fourier transform of $\chi(k)\cdot k^3$ was carried out on the resultant k-space spectra, over a k-range of 3-12 Å⁻¹. Refinements of the Au₂₅ and Au₂₄Pt Au L₃-edge EXAFS R-space spectra were carried out over an R-range window of 1.55–3.1 Å, and included the Au-S and one Au-Au coordination shells. The spectra were fit with an S_0^2 of 0.9 obtained from bulk Au foil, yielding values for bond length (R), Debye-Waller factor (σ^2), and energy shift values (ΔE_0 - correlated).

For the Pt L₃-edge EXAFS spectrum of the Au₂₄Pt system, a Fourier transform of $\chi(k)\cdot k^2$ and the subsequent data refinement, were carried out over a k-range of 3-8.8 Å⁻¹, with an S_0^2 value of 0.915 obtained from bulk Pt foil. Refinements of the Pt-S and Pt-Au coordination shells were carried out with an R-range window of 1.2 –3.1 Å, in order to determine bond length (R), Debye-Waller factor (σ^2), and energy shift values (ΔE_0).

6.2.3 Calculations

Calculations of s, p, and d-electron counts were carried out using the FEFF8.2 computational software suite. FEFF is an *ab initio* self-consistent multiple-scattering code,

employing Green's functions to reduce the computational cost involved in the calculation of electronic structure and X-ray absorption fine-structure (XAFS) spectra. A series of model systems were used, including Au₂₅, Au₂₄Pt (central Au replaced with Pt) and Au₂₄ (without central Au atom), using the crystal structure of Au₂₅ in contracted (1%) and non-contracted conformations (Figure 6-8).^{52,64}

6.3 Results and discussion

6.3.1 Dopant Location

In order to determine the location of the Pt dopant, it is necessary to verify the molecular formula of the Pt-doped Au nanocluster. Mass spectrometry has been shown to be a powerful tool in resolving and verifying the production of these small cluster systems.⁴⁹ The composition of the as-synthesized Au₂₄Pt(SR)₁₈ (R = CH₂CH₂Ph) nanoclusters was first checked by MALDI mass spectrometry (Figure 6-1). The intact cluster peak was observed at 7392 Da, in agreement with the calculated formula weight (7391.88 g mol⁻¹).

In theory Pt L₃-edge EXAFS is an ideal tool to identify the location of Pt in Au₂₄Pt by analyzing the CN of Pt (Figure 6-2).²²² However, in order to reliably analyze the Pt dopant location, it is important to first take into account any other Pt species existing in the system. Figure 6-3 shows the XPS compositional analysis, enabling the comparison of relative elemental distribution in the sample system. Normalization of X-ray photoemission peaks by their relative elemental sensitivity factors yielded an average composition of Au_{24.0}Pt_{2.2}S_{19.1}(Table 6-1). As mass spectrometry data indicate contribution from only one Pt atom per nanocluster, the XPS-derived values of 2.2 for Pt

and 19.1 for S indicate another Pt-S species in roughly a 1:1 ratio (Pt:S = 1.2:1.1).

Considering the composition of starting materials, it is most likely the extra Pt in the system is due to unreacted Pt-thiolate oligomer that was below the limit of detection for mass spectrometry.

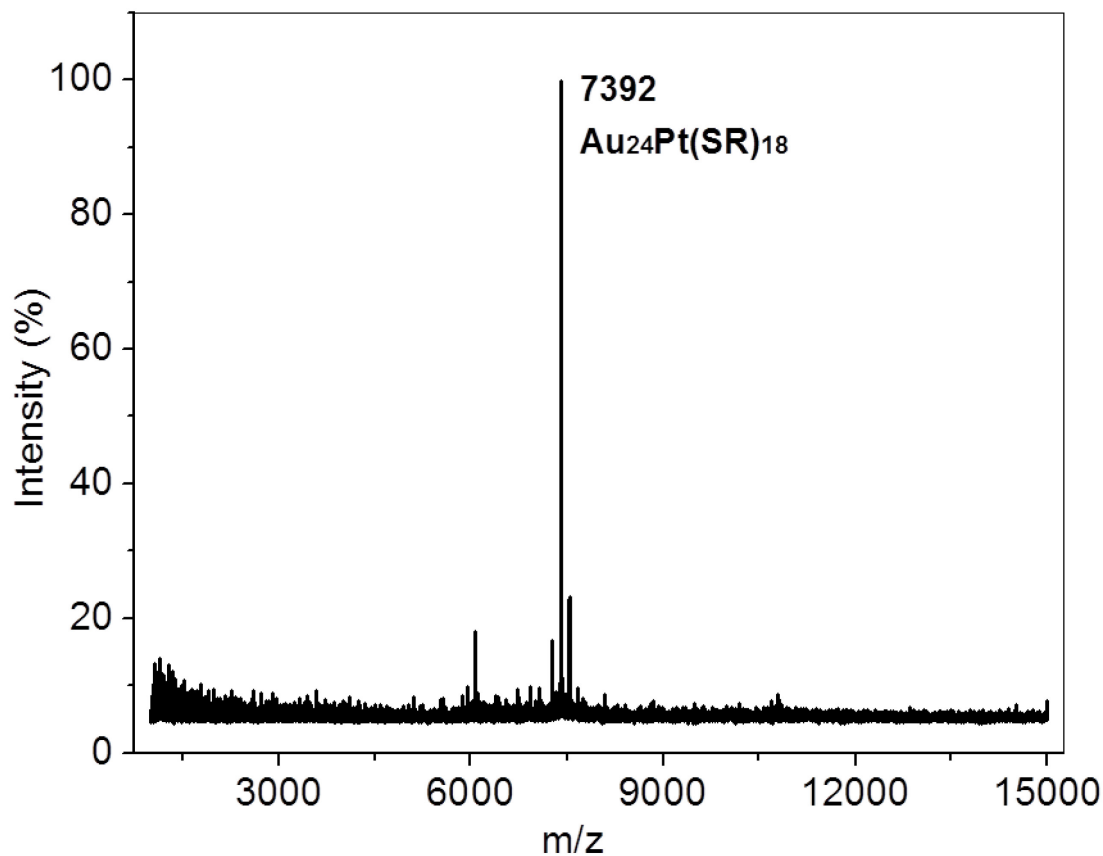


Figure 6-1. Positive mode matrix-assisted laser desorption ionization (MALDI) mass spectrum of Au₂₄Pt(SCH₂CH₂Ph)₁₈ nanoclusters.

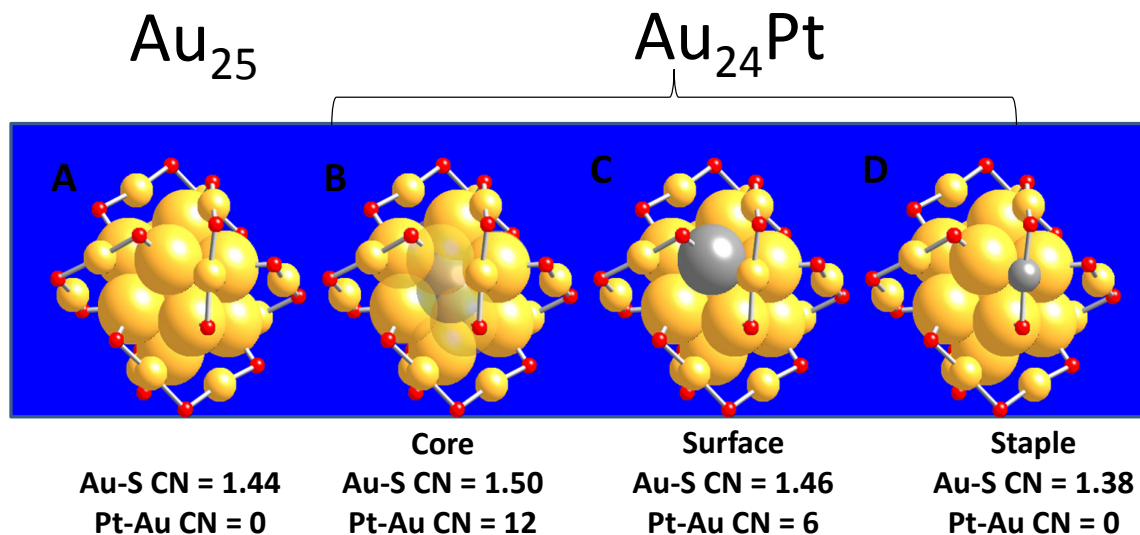


Figure 6-2. Schematic representations and theoretical coordination numbers for averaged Au-S and Pt-Au bonding in A) Au_{25} , B) $Au_{24}Pt$ with Pt in core position, C) $Au_{24}Pt$ with Pt in surface position, and D) $Au_{24}Pt$ with Pt in staple position.

Table 6-1. XPS Compositional analysis data of the $Au_{24}Pt$ sample.

Elements	Binding Energy(eV)	Full Width Half Max (FWHM)	Area	Atomic Percentage (%)
Pt	75.0	2.188	870.63	4.9
Au	87.0	2.036	10578.54	53.0
S	162.5	2.408	1175.79	42.1

*Au:Pt:S = 24.0: 2.2: 19.1

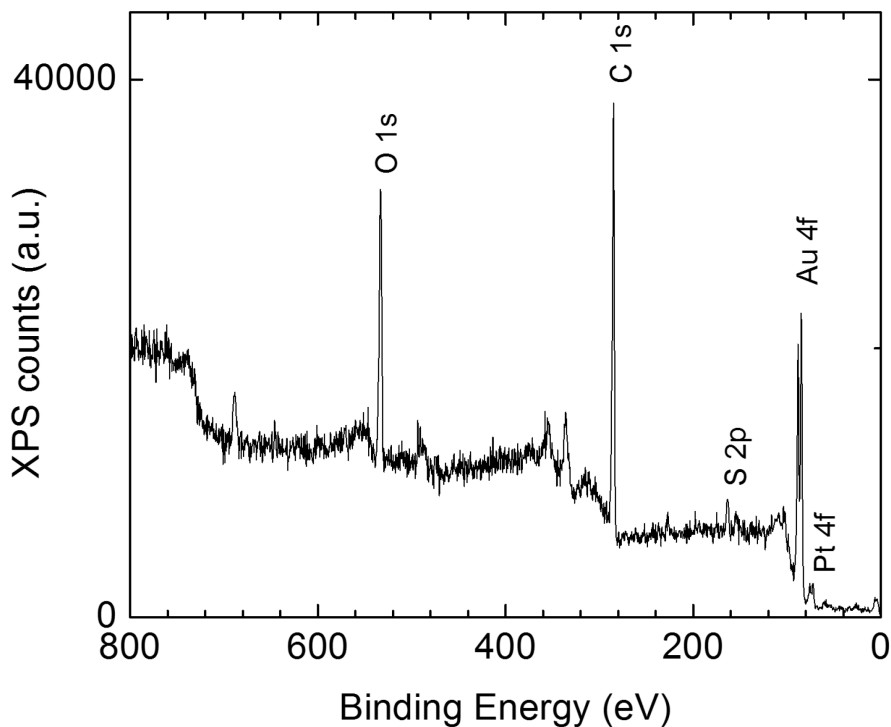


Figure 6-3. XPS survey scan spectra of the Au₂₄Pt nanocluster system taken with incident photon energy of 1000 eV.

In our system, it is clear that the Pt-thiolate component will only show a Pt-S shell in the EXAFS of the mixture, whereas Pt in the doped nanocluster could show a Pt-Au shell (Pt in center), a Pt-S shell (Pt in staple) or a Pt-Au and a Pt-S shell (Pt on surface). The theoretical coordination numbers used for refinement of the Au-S (Pt-S) and Au-Au (Pt-Au) coordination shells in the Au₂₅ and Au₂₄Pt nanocluster systems were calculated using the crystal structure model of Au₂₅.^{52,64} While the CN values for the Au₂₅ nanocluster are known, the CN values in the Au₂₄Pt nanocluster differ relative to the location of the Pt atom in the nanocluster system (Figure 6-2). In order to use Pt L₃-edge EXAFS to deduce the location of the Pt dopant, the theoretical Pt-S and Pt-Au CN values were determined for Pt in each possible location by the summation of the Pt CN values in

both the nanocluster and the remaining Pt-thiolate material (Table 6-2).²²³ The nanocluster and remnant Pt-thiolate Pt CN values were determined by averaging the number of nearest neighbor Au and S atoms surrounding the Pt atom, and multiplying them by the ratio Pt_x/Pt_{total} , where Pt_x is the stoichiometric value of Pt in the nanocluster or remnant Pt-thiolate, and Pt_{total} is the total amount of Pt in the sample.

Table 6-2. Pt L₃-edge EXAFS fit results of Au₂₄Pt^{ab}

	Pt-S	Pt-Au
Theoretical CN_{staple}	3.2	0
Theoretical CN_{surface}	2.8	2.4
Theoretical CN_{center}	2.4	4.9
Experimental CN	2.6(1)	5.5(3)
R (Å)	2.319(4)	2.750(4)
σ² (Å²)	0.0013(2)	0.010(1)
ΔE₀ (eV)	1.0(5)	0.4(9)

^a S₀² fixed at 0.915, ^b brackets denote error

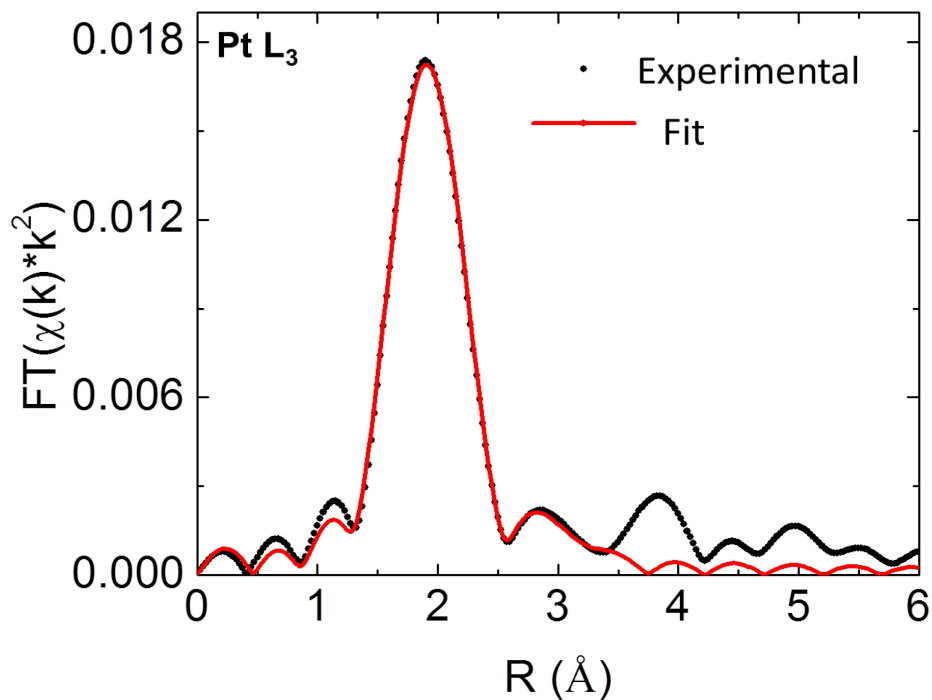


Figure 6-4. Experimental Pt L₃-edge EXAFS spectrum and fitting of the Pt-S shell.

The experimental Pt L₃-edge EXAFS fit results are presented in Table 6-2 and Figure 6-4. Since the difference in the theoretical Pt-S CN values is within the uncertainty of experimental EXAFS (10%-20%), we focus our analysis on the Pt-Au CN values as the theoretical Pt-Au CN values corresponding to the three possible dopant locations are dramatically different. By comparing the experimental Pt-Au CN value (5.5 ± 0.3) with the three calculated values for Pt in staple (0), surface (2.4), and center (4.9) positions, the Pt dopant can be clearly determined to be in the center of the nanocluster. In addition, the Pt-Au bond length (R) was determined to be 2.75 Å (Table 6-2, Figure 6-4). This value is shorter than the Au_{center}-Au_{surface} bond distance in Au₂₅, determined by both X-ray crystallography (2.79 Å),^{52,64} and the Au L₃-edge EXAFS to be presented in

the next section (2.81 Å – Table 6-3). The shorter Pt-Au bond length suggests that inclusion of Pt into the Au₂₅ structure causes contraction of the nanocluster. To further understand the doping effect on the local structure of the nanoclusters, complementary Au L₃-edge EXAFS data are presented next.

6.3.2 Local Structure

Figure 6-5 shows the Au L₃-edge R-space EXAFS spectra for the Au₂₅ and Au₂₄Pt nanocluster systems. Both nanocluster systems show significant contribution from the Au-S coordination shell (Figure 6-5), while the Au-Au and Au-Pt features vary only slightly, as any change is due solely to effects by the center-positioned Pt atom.

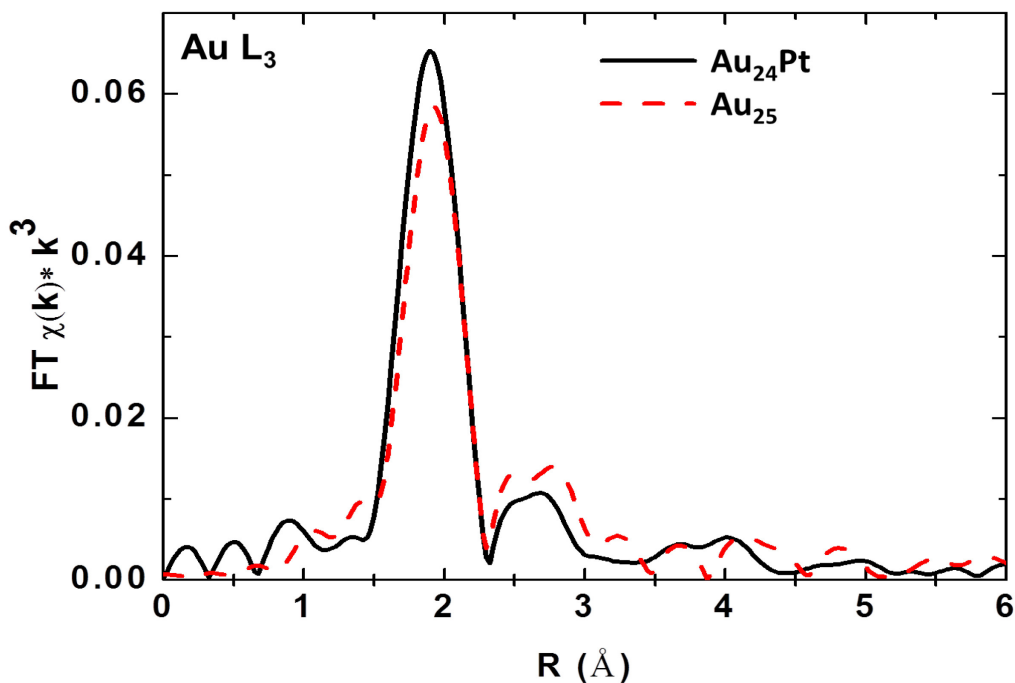


Figure 6-5. Experimental Au L₃-edge EXAFS spectra of the Au₂₄Pt (black solid) and Au₂₅ (red dashed) nanocluster systems.

Refinement of the Au-S and one Au-Au coordination shells were conducted and the results are presented in Figure 6-6 and Table 6-3. No reliable fit could be obtained for the Au-Pt shell, as Pt-Au and Au-Au shells are not distinguishable based on the available EXAFS k-range. The most striking finding is that the Pt doped nanocluster shows a reduction in both the Au-S bond length (~ 0.02 Å) and the Au-Au bond length (~ 0.02 Å), when compared to the results of the Au₂₅ nanocluster.

Table 6-3. Au L₃-edge EXAFS two-shell fit results for Au₂₅ and Au₂₄Pt^{ab}

	Au ₂₄ Pt		Au ₂₅	
	Au-S	Au-Au (Pt)	Au-S	Au-Au
CN	1.7(2)	2(1)	1.6(1)	1.1(2)
R (Å)	2.315(5)	2.79(1)	2.332(7)	2.81(1)
$\sigma^2(\text{Å}^2)$	0.0040(7)	0.013(5)	0.0042(4)	0.006(1)
$\Delta E_0(\text{eV})$	-0.7(9)	-0.7(9)	0.5(5)	0.5(5)

^a S₀² fixed at 0.9, ^b brackets denote error

This finding is consistent with the complementary Pt L₃-edge EXAFS results (Table 6-2). The first-shell Au-Au EXAFS is primarily associated with the Au_{surface}-Pt_{center} and part of the Au_{surface}-Au_{surface} bonds, according to the total structure of Au₂₅(SR)₁₈. The decrease in the Au-Au bond length for the Au₂₄Pt nanocluster system can be attributed to the smaller atomic radius of Pt (1.44 Å for Au vs. 1.28 Å for Pt) and the higher interaction energy for Pt-Au bonds than Au-Au bonds,²²⁴ while the reduction in Au-S bond length could be associated with gold electronic properties caused by Pt-doping. To further study the electronic properties of Au atoms in the nanoclusters, we turn to the Au 4f XPS next.

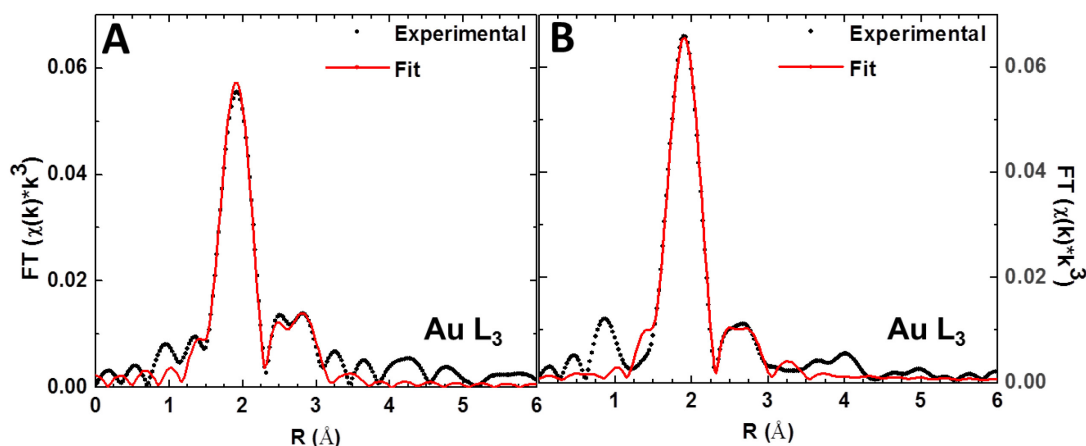


Figure 6-6. Experimental Au L₃-edge EXAFS spectra, and fitting of the Au-S shell, for the A) Au₂₄Pt and B) Au₂₅ nanocluster systems.

6.3.3 Electronic Properties

In Figure 6-7A, the Au 4f high-resolution XPS data of Au₂₅, Au₂₄Pt, and bulk Au reference are presented. The spectra show a positive shift of 0.08 eV for the Au₂₄Pt system, and 0.19 eV for the Au₂₅ system, relative to 84.00 eV for the Au foil system. Interestingly, there is a striking difference in the lineshape of the two nanoclusters, that is, the Au₂₄Pt spectrum shows a significant narrowing in comparison to that of the Au₂₅. Figures 6-7B and 6-7C are the fitted Au 4f spectra of Au₂₅ and Au₂₄Pt, respectively. The Au₂₅ peaks can be fitted with three components, with peak area ratios of 1:12:12 for Au_{center}:Au_{surface}:Au_{staple}, while the Au₂₄Pt, due to the absence of a center Au atom, can only be fit with two components, in a 1:1 peak area ratio of Au_{surface}:Au_{staple} (Table 6-4). Similar to previous XPS work on a larger Au-thiolate nanocluster,¹⁸⁵ there is a shift in component binding energy position as we move from center, to surface, to staple Au sites. The Au₂₄Pt Au 4f peaks are situated at lower binding energies to those of their corresponding Au₂₅ peaks. This shift may be due to a bimetallic bonding (alloying) effect

as seen in bulk Au/Pt alloy samples.²²⁵ A similar negative shift has also been observed by Negishi *et al.* in Ag-doped Au nanoclusters.²¹⁷

Table 6-4. Site-specific comparison of the Au 4f_{7/2} XPS peak positions and full-width half-maxima for Au₂₅ and Au₂₄Pt

	Center		Surface		Staple	
	Position (eV)	FWHM (eV)	Position (eV)	FWHM (eV)	Position (eV)	FWHM (eV)
Au ₂₅	84.00	0.043	84.30	0.85	84.71	1.51
Au ₂₄ Pt	---	---	84.06	0.56	84.48	1.41
Au ₂₅ -Au ₂₄ Pt	---	---	0.24	0.29	0.23	0.10

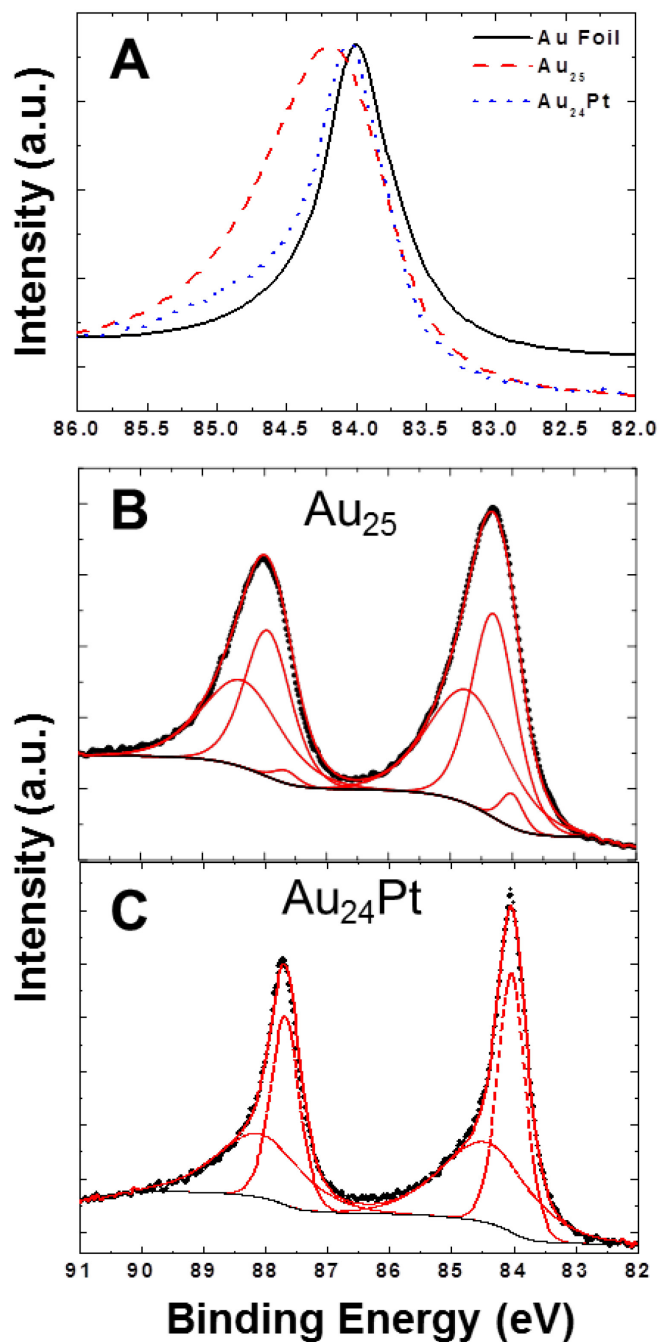


Figure 6-7. A) High-resolution Au $4f_{7/2}$ XPS spectra of the Au_{25} (red dash), $Au_{24}Pt$ (blue dot), and Au foil (black line) denoting binding energy shift of 0.19 eV (Au_{25}) and 0.08 eV ($Au_{24}Pt$). All spectra normalized for peak height, so as to better denote binding energy shift. High-resolution Au 4f spectra of B) Au_{25} and C) $Au_{24}Pt$ are shown, where experimental data is denoted as black dots, envelope and component fitting are denoted in red, and Shirley background is denoted as a black line. All spectra acquired with an incident photon energy of 700 eV.

Differences in the full-width half-maxima (FWHM) for the Au 4f_{7/2} component spectra are denoted in Table 6-4, while Au 4f_{7/2} peak areas and Au 4f_{5/2} energy positions, FWHM, and peak areas can be found in the Table 6-4. For both the surface and staple components, the Au 4f peaks of Au₂₅ have a larger FWHM than those of Au₂₄Pt (Table 6-4 and Figures 6-7B,C). We propose the Au 4f lineshape narrowing to be due to the bond contraction effect. When the nanoclusters contract, as in the Au₂₄Pt system, neighboring atoms are positioned closer together, leading to a more ordered structure, and therefore less broadening of the Au 4f lineshape.

To further elucidate the role of bimetallic bonding and bond contraction effects in causing the difference of electronic properties between Au₂₄Pt and Au₂₅, *ab-initio* calculations were carried out on a series of model systems, including Au₂₅, Au₂₄Pt (central Au replaced with Pt) and Au₂₄ (without central Au atom), using the crystal structure of Au₂₅ in contracted (1%) and non-contracted conformations (Figure 6-8).^{52,64} Comparisons of contracted and non-contracted systems (with the same composition), and doped and non-doped systems (with the same bond length), make it possible to identify the role of the bond contraction effect and bimetallic bonding effect in determining the change of the electronic properties of the nanoclusters.

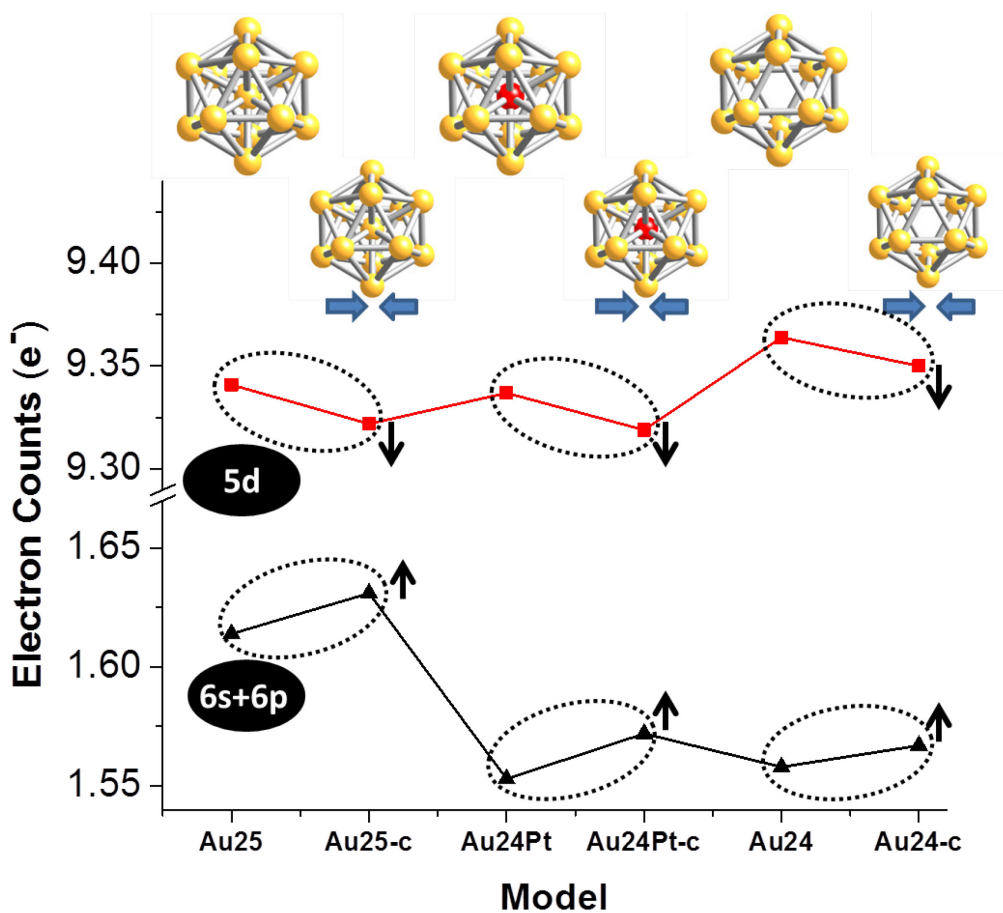


Figure 6-8. Calculated electron counts for 6s+p and 5d-electrons of surface gold atoms in three series of model systems based on the crystal structure of Au₂₅. The three systems are Au₂₅, Au₂₄Pt (central Au replaced with Pt) and Au₂₄ (in absence of central Au atom).

Models with 1% contracted bond distances (e.g. Au_{25-c}, Au₂₄Pt-c and Au_{24-c}) bond distance are also used in calculations in order to illustrate the lattice contraction effect.

For clarity, model systems are depicted without staple motif Au and S atoms.

The bond contraction effect is discussed first. As is seen in Figure 6-8, the bond contraction in the three systems (contracted systems denoted with “-c”) causes an apparent and similar change to surface Au atoms, that is, a decrease of the 5d-electron count associated with an increase of the 6s/p electron counts. The observed change of electron counts caused by the bond contraction effect can be understood by using the donation/back-donation model for the electronic interaction between gold and sulfur.^{198,226} According to this model, gold will donate 5d-electron to sulfur empty 3d state whereas sulfur will back-donate 3p-electron density to the electron deficient Au 6s/p states. Therefore, a Au-S contraction effect will enhance the donation/back-donation effect, causing a decrease of 5d electron counts and an increase of 6s/p electron counts.

Next, the Pt-Au bimetallic bonding effect is investigated by first inspecting the 5d electron counts of the three systems (including contacted and non-contacted models). When comparing the two Au₂₅ models with the corresponding Au₂₄Pt models, it is evident that the Au 5d electron counts essentially remain unchanged after replacing the center Au with Pt. In comparison, the two 25-atom metal cluster systems (Au₂₅ and Au₂₄Pt) both show a sizable decrease in 5d electron counts comparing with the Au₂₄ system. The unchanged 5d electronic behavior of Au between Au₂₅ and Au₂₄Pt systems can be understandable when considering the intense 5d-5d bimetallic bonding interactions between Au and Pt.²²⁷ Therefore, replacement of the center Au with Pt causes almost no change to the 5d electron behavior of Au atoms. In contrast, the absence of the center metal atom in the icosahedron core will reduce the average coordination number of each surface Au atom from 6 to 5. It has been reported that the d-electron counts of Au will increase upon the decrease of its average CN due to the reduced s-p-d

rehybridization effect in lower-coordinated Au system.²²⁸ The decreased d-electron counts for the Au₂₄ system observed in Figure 6-8 are consistent with this mechanism.

When inspecting the Au 6s/p behavior, it can be seen that the 6s/p electron counts of Au₂₄ are decreased relative to that of Au₂₅. This observation again can be interpreted as the reduced s-p-d rehybridization effect (*i.e.* less 5d electron flow to the 6s/p state) for the lower-coordinated Au₂₄ system. Interestingly, the 6s/p electron counts for the Au₂₄Pt system are quite different from that of Au₂₅ counterparts; instead, they are essentially the same as that of the Au₂₄ system. These results suggest that the Au 6s/p electron counts in Au₂₄Pt are largely determined by metal-metal bonding between like-atoms. Therefore, replacement of the center Au atom with Pt makes the Au 6s/p electronic behavior of Au₂₄Pt essentially the same as that of the empty icosahedron Au₂₄ system.

6.4 Summary

In conclusion, we have shown a series of findings on Au₂₄Pt using EXAFS, XPS, and *ab initio* calculations, including (i) determination of the Pt dopant atom location, (ii) metal-S and metal-metal bond contractions caused by Pt-doping, and (iii) significant role of bimetallic bonding and bond contraction effects on the electronic properties of Au₂₄Pt. Finally, the complementary X-ray spectroscopy approach presented in this work (survey/core-level XPS, and EXAFS from Au and dopant perspectives) should be applicable to the studies of many other heteroatom-doped Au-thiolate nanocluster systems recently synthesized.²²⁹

CHAPTER 7 CONCLUSIONS AND FUTURE WORK

7.1 Conclusions

The goal of these studies was to further the understanding of structure and bonding in Au NP systems, with respect to type of ligand, metal:ligand ratio, NP size, and NP composition. As such, it was pertinent to explore change through comparison of similar systems.

Taking advantage of a one-step synthesis capable of reproducibly depositing biomolecule-functionalized Au NPs onto a Ti substrate, it was possible to modify the size and surface of the supported Au NPs. This deposition and modification shows promise in future biomedical applications, as well as advancing control of substrate-supported metal NPs in general. Making use of BSA, a large model biomolecule, the effect of steric bulk on deposition mechanics was studied and determined to play a significant role in the limiting of Au NP size. By limiting access to Au nucleation centres, BSA can limit Au NP size with minimal concentration dependence. On the other hand, in experiments involving smaller model biomolecules (MPG and GSH), concentration of biomolecule varied the mean particle size of deposited Au NPs. This concentration-dependence enabled the fine-tuning of Au NP size (from larger NPs to nanocluster to Au-thiolate polymer). While this had been observed in many solution-phase syntheses, fine-control of substrate-supported NP sizes is much desired for surface-functionalization. Furthermore, modification to a glancing-angle EXAFS experimental setup with sample spinning allows for the acquisition of data from very low substrate loadings, enabling structure and size characterization for systems where this information was previously unattainable.

To approach the study of structure and bonding in Au NP systems from the metal perspective, Au NC samples with exact X-ray crystallographic coordinates were studied (Au_{25} and Au_{102}). By comparing the similar surface structures of both the Au_{25} and Au_{102} , we were able to computationally determine bond length, electronic character, and local environment for the double-staple bonding structure present in both samples. Comparing *ab initio* calculated Au L_3 -edge EXAFS spectra, it was determined that the double-staple motifs retain their coordination, though the staple-surface aurophilic interaction distances in the Au_{25} sample were significantly longer range than for Au_{102} . These findings were supported by charge transfer and electron-density calculations.

Finally, the effect of Pt heteroatom doping, the replacement of a single Au atom with Pt, on the Au_{25} structure was studied using a combination of *ab initio* calculations, EXAFS spectroscopy, and XPS analysis. Using EXAFS and XPS spectroscopy, the exact location of Pt in the Au_{25} structure (Au_{24}Pt) was definitively determined to be the central position. Using this knowledge, it was determined that the introduction of Pt into the Au_{25} structure leads to a contraction, supported by Au L_3 -edge EXAFS, XPS, and *ab initio* calculations.

By studying both supported Au NP and compositionally-precise Au NC samples, much has been learned regarding the effects of ligand and metal composition on the structure and bonding of nanoscale Au-thiolate systems. This work contributes to future supported nanoparticle studies, with potential biological applications, as well as a greater understanding of the properties that govern Au NC systems.

7.2 Future Work

Ti-supported Studies with Varied Nanoparticle Composition

Depositing Au NPs onto Ti provides a platform for further functionalization. Much of this work may be extended to biological systems, and metals such as Ag, Pt, and Pd, or even alloys of these metals, would fine-tune the reactivity of supported NPs. Preliminary studies were carried out in Chapter 3 showing the deposition of Ag and Pd NPs onto a Ti-substrate, demonstrates the viability of the same particle size control mechanisms at play in the Ti-supported biomolecule-functionalized Au NPs.

Bio-activity Studies

An eventual goal for Ti-supported biomolecule-coated metal NPs is use in biological systems (*e.g.* orthopaedic implantation, local delivery of specific biomolecules, etc.). As such, it is important to understand whether the bio-activity of the biomolecule is altered after binding to the NPs. An appropriate first step would be the performance of a BSA enzyme-linked immunosorbent assay (ELISA) on the Ti plates, where the BSA-coated Au NPs are the antigen being analysed. These tests are sensitive to pg/mL in solution, but should be capable of detecting BSA on the Au NP surface.

Though the ELISA would provide information on the Au:BSA samples, no similar tests are available for the Au:MPG and Au:GSH samples. By modification of the Au:BSA, Au:MPG, or Au:GSH samples with a previously characterized prototype protein (*e.g.* lysozyme),^{106,230} it may be possible to gain insight into the ability of these

samples to adhere beneficial biomolecules. These studies could potentially lead to the use of bone morphogenetic protein (BMP), followed by actual bone-adhesion studies using those samples. Initially, a micro bicinchoninic acid (BCA) would be carried out to determine the concentration of lysozyme available on the Au NP surface.¹⁰⁶ Very small quantities of solution would be allowed to react on the Ti surface, followed by colorimetric analysis. This would then be used to normalize the results of a lysozyme activity assay.

Correlate X-ray results of nanocluster studies with catalytic activity experiments

With increasing interest in Au NPs as catalysts,¹¹⁵ it would be interesting to follow catalytic reactions of these AuNPs prepared in this work using X-ray spectroscopy. These *in-situ* experiments would monitor bond length, coordination, and oxidation in Au NCs over the course of a number of general catalytic reactions,^{42,49} providing insight into the electronic and structural changes that govern the catalytic reaction mechanism. These studies may also provide insight into the poisoning of catalytic reactions and perhaps suggest alternative catalytic requirements.

REFERENCES

- (1) Ferrando, R.; Jellinek, J.; Johnston, R. L. *Chem. Rev.* **2008**, *108*, 845.
- (2) Gucci, L. *Catal. Today* **2005**, *101*, 53.
- (3) Liu, F.; Zhang, P. *Appl. Phys. Lett.* **2010**, *96*, 043105.
- (4) Sau, T. K.; Murphy, C. J. *J. Am. Chem. Soc.* **2004**, *126*, 8648.
- (5) Langille, M. R.; Personick, M. L.; Zhang, J.; Mirkin, C. a. *J. Am. Chem. Soc.* **2012**, *134*, 14542.
- (6) Xia, Y. N.; Yang, P. D.; Sun, Y. G.; Wu, Y. Y.; Mayers, B.; Gates, B.; Yin, Y. D.; Kim, F.; Yan, Y. Q. *Adv. Mater.* **2003**, *15*, 353.
- (7) Kim, B. Y.; Shim, I.-B.; Araci, Z. O.; Saavedra, S. S.; Monti, O. L. a; Armstrong, N. R.; Sahoo, R.; Srivastava, D. N.; Pyun, J. *J. Am. Chem. Soc.* **2010**, *132*, 3234.
- (8) Frenkel, A. I.; Nemzer, S.; Pister, I.; Soussan, L.; Harris, T.; Sun, Y.; Rafailovich, M. H. *J. Chem. Phys.* **2005**, *123*, 184701.
- (9) Jana, N. R.; Gearheart, L.; Murphy, C. J. *Langmuir* **2001**, *17*, 6782.
- (10) Kaur, K.; Forrest, J. A. *Langmuir* **2012**, *28*, 2736.
- (11) Subramanian, V.; Wolf, E. E.; Kamat, P. V. *J. Am. Chem. Soc.* **2004**, *126*, 4943.
- (12) Knowles, K. E.; Tice, D. B.; McArthur, E. a; Solomon, G. C.; Weiss, E. a. *J. Am. Chem. Soc.* **2010**, *132*, 1041–50.
- (13) Zhou, M.; Cai, Y. Q.; Zeng, M. G.; Zhang, C.; Feng, Y. P. *Appl. Phys. Lett.* **2011**, *98*, 143103.
- (14) Freestone, I.; Meeks, N.; Sax, M.; Higgitt, C. *Gold Bull.* **2007**, *40*, 270.
- (15) Dykman, L.; Khlebtsov, N. *Chem. Soc. Rev.* **2012**, *41*, 2256.
- (16) Antonii, F. *Panacea Aurea - Auro Potabile*; Bibliopolio Frobeniano: Hamburg, 1618; p. 205.
- (17) Thompson, D. *Gold Bull.* **2007**, *40*, 267.
- (18) Johnbod . *Creative Commons Attribution-Share Alike 3.0 Unported License* **2010**.

- (19) Turkevich, J.; Stevenson, P. C.; Hillier, J. *Discuss. Faraday Soc.* **1951**, *11*, 55.
- (20) Brust, M.; Walker, M.; Bethell, D.; Schiffrin, D. J.; Whyman, R. *J. Chem. Soc., Chem. Commun.* **1994**, 801.
- (21) Daniel, M.-C. C.; Astruc, D. *Chem. Rev.* **2004**, *104*, 293.
- (22) Parker, J. F.; Fields-Zinna, C. A.; Murray, R. W. *Acc. Chem. Res.* **2010**, *43*, 1289.
- (23) Zheng, J.; Zhang, C.; Dickson, R. *Phys. Rev. Lett.* **2004**, *93*, 077402.
- (24) Chevrier, D. M. *J. Nanophoton.* **2012**, *6*, 064504.
- (25) Qian, H.; Zhu, M.; Wu, Z.; Jin, R. *Acc. Chem. Res.* **2012**, *45*, 1470.
- (26) Kubo, R.; Kawabata, A.; Kobayashi, S. *Annu. Rev. Mater. Sci.* **1984**, *14*, 49.
- (27) Henderson, W. *Adv. Organomet. Chem.* **2006**, *54*, 207.
- (28) Jadzinsky, P. D.; Calero, G.; Ackerson, C. J.; Bushnell, D. A.; Kornberg, R. D. *Science* **2007**, *318*, 430.
- (29) Schmidbaur, H. *Gold Bull.* **2000**, *33*, 3.
- (30) Schmidbaur, H.; Schier, A. *Chem. Soc. Rev.* **2008**, *37*, 1931.
- (31) Pyykko, P. *Angew. Chem. Int. Ed.* **2004**, *43*, 4412.
- (32) Runeberg, N.; Schütz, M.; Werner, H.-J. *J. Chem. Phys.* **1999**, *110*, 7210.
- (33) Vicente, J.; Chicote, M.; Lagunas, M.-C. *Inorg. Chem.* **1993**, *32*, 3748.
- (34) Schmidbaur, H.; Graf, W.; Muller, G. *Angew. Chem. Int. Ed.* **1988**, *27*, 417.
- (35) Brown, T. L.; Lemay, H. E.; Bursten, B. E. *Chemistry: The Central Science*; 8th ed.; Prentice Hall: Upper Saddle River, 1999.
- (36) Jiang, Y.; Alvarez, S.; Hoffmann, R. *Inorg. Chem.* **1985**, *24*, 749.
- (37) Schmidbaur, H.; Cronje, S.; Djordjevic, B.; Schuster, O. *Chem. Phys.* **2005**, *311*, 151.
- (38) Ziegler, T.; Snijders, J. G.; Baerends, E. J. *Int. J. Quantum Chem.* **1980**, *18*, 393.
- (39) Wang, S.-G.; Schwarz, W. H. E. *J. Am. Chem. Soc.* **2004**, *126*, 1266.

- (40) Grönbeck, H.; Walter, M.; Häkkinen, H. *J. Am. Chem. Soc.* **2006**, *128*, 10268.
- (41) Love, J. C.; Estroff, L. A.; Kriebel, J. K.; Nuzzo, R. G.; Whitesides, G. M. *Chem. Rev.* **2005**, *105*, 1103.
- (42) Zhu, Y.; Qian, H.; Drake, B. a; Jin, R. *Angew. Chem. Int. Ed.* **2010**, *49*, 1295.
- (43) Simard, J.; Briggs, C.; Boal, A. K.; Rotello, V. M. *Chem. Commun.* **2000**, 1943.
- (44) Murphy, P. B.; Liu, F.; Cook, S. C.; Jahan, N.; Marangoni, D. G.; Grindley, T. B.; Zhang, P. *Can. J. Chem.* **2009**, *87*, 1641.
- (45) Barnett, C. M.; Gueorguieva, M.; Lees, M. R.; McGarvey, D. J.; Darton, R. J.; Hoskins, C. *J. Nanopart. Res.* **2012**, *14*, 1170.
- (46) Toshima, N.; Yonezawa, T. *New J. Chem.* **1998**, *22*, 1179.
- (47) Zhou, M.; Cai, Y. Q.; Zeng, M. G.; Zhang, C.; Feng, Y. P. **2012**, *143103*, 1.
- (48) Zhu, M.; Aikens, C. M.; Hendrich, M. P.; Gupta, R.; Qian, H.; Schatz, G. C.; Jin, R. *J. Am. Chem. Soc.* **2009**, *131*, 2490.
- (49) Qian, H.; Jiang, D.; Li, G.; Gayathri, C.; Das, A.; Gil, R. R.; Jin, R. *J. Am. Chem. Soc.* **2012**, *134*, 16159.
- (50) Frenkel, A. I. *Chem. Soc. Rev.* **2012**, *41*, 8163.
- (51) Mahl, D.; Diendorf, J.; Ristig, S.; Greulich, C.; Li, Z.-A.; Farle, M.; Köller, M.; Epple, M. *J. Nanopart. Res.* **2012**, *14*, 1153.
- (52) Heaven, M. W.; Dass, A.; White, P. S.; Holt, K. M.; Murray, R. W. *J. Am. Chem. Soc.* **2008**, *130*, 3754.
- (53) Zhu, M.; Lanni, E.; Garg, N.; Bier, M. E.; Jin, R. *J. Am. Chem. Soc.* **2008**, *130*, 1138.
- (54) Donkers, R. L.; Song, Y.; Murray, R. W. *Langmuir* **2004**, *20*, 4703.
- (55) Jin, R.; Egusa, S.; Scherer, N. F. *J. Am. Chem. Soc.* **2004**, *126*, 9900.
- (56) Jiang, D. E.; Chen, W.; Whetten, R. L.; Chen, Z. F. *J. Phys. Chem. C* **2009**, *113*, 16983.
- (57) Jiang, D. E.; Whetten, R. L.; Luo, W. D.; Dai, S. *J. Phys. Chem. C* **2009**, *113*, 17291.

- (58) Negishi, Y.; Nobusada, K.; Tsukuda, T. *J. Am. Chem. Soc.* **2005**, *127*, 5261.
- (59) Negishi, Y.; Chaki, N. K.; Shichibu, Y.; Whetten, R. L.; Tsukuda, T. *J. Am. Chem. Soc.* **2007**, *129*, 11322.
- (60) Li, Y.; Galli, G.; Gygi, F. *ACS Nano* **2008**, *2*, 1896.
- (61) Qian, H.; Jin, R. *Nano Lett.* **2009**, *9*, 4083.
- (62) Pei, Y.; Gao, Y.; Zeng, X. C. *J. Am. Chem. Soc.* **2008**, *130*, 7830.
- (63) Zhu, M.; Qian, H.; Jin, R. *J. Am. Chem. Soc.* **2009**, *131*, 7220.
- (64) Zhu, M.; Aikens, C. M.; Hollander, F. J.; Schatz, G. C.; Jin, R. *J. Am. Chem. Soc.* **2008**, *130*, 5883.
- (65) Qian, H.; Eckenhoff, W. T.; Zhu, Y.; Pintauer, T.; Jin, R. *J. Am. Chem. Soc.* **2010**, *132*, 8280.
- (66) Zeng, C.; Qian, H.; Li, T.; Li, G.; Rosi, N. L.; Yoon, B.; Barnett, R. N.; Whetten, R. L.; Landman, U.; Jin, R. *Angew. Chem. Int. Ed.* **2012**, *51*, 13114.
- (67) Wu, Z. K.; Jin, R. C. *ACS Nano* **2009**, *3*, 2036–2042.
- (68) Qian, H.; Zhu, Y.; Jin, R. *ACS nano* **2009**, *3*, 3795.
- (69) Zhu, M.; Eckenhoff, W. T.; Pintauer, T.; Jin, R. *J. Phys. Chem. C* **2008**, *112*, 14221.
- (70) Kauffman, D. R.; Alfonso, D.; Matranga, C.; Qian, H.; Jin, R. *J. Am. Chem. Soc.* **2012**, *134*, 10237.
- (71) Jiang, D. E.; Luo, W.; Tiago, M. L.; Dai, S. *J. Phys. Chem. C* **2008**, *112*, 13905.
- (72) Aikens, C. M. *J. Phys. Chem. C* **2008**, *112*, 19797.
- (73) Qian, H.; Zhu, Y.; Jin, R. *J. Am. Chem. Soc.* **2010**, *132*, 4583.
- (74) Dharmaratne, A. C.; Krick, T.; Dass, A. *J. Am. Chem. Soc.* **2009**, *131*, 13604.
- (75) Fields-Zinna, C. A.; Sampson, J. S.; Crowe, M. C.; Tracy, J. B.; Parker, J. F.; DeNey, A. M.; Muddiman, D. C.; Murray, R. W. *J. Am. Chem. Soc.* **2009**, *131*, 13844.

- (76) Toikkanen, O.; Ruiz, V.; Ronholm, G.; Kalkkinen, N.; Liljeroth, P.; Quinn, B. M. *J. Am. Chem. Soc.* **2008**, *130*, 11049.
- (77) Negishi, Y.; Kurashige, W.; Niihori, Y.; Iwasa, T.; Nobusada, K. *PCCP* **2010**, *12*, 6219.
- (78) Qian, H.; Zhu, M.; Lanni, E.; Zhu, Y.; Bier, M. E.; Jin, R. *J. Phys. Chem. C* **2009**, *113*, 17599.
- (79) Shibata, T.; Bunker, B. A.; Zhang, Z. Y.; Meisel, D.; Vardeman, C. F.; Gezelter, J. D. *J. Am. Chem. Soc.* **2002**, *124*, 11989.
- (80) Gao, Y.; Shao, N.; Pei, Y.; Zeng, X. C. *Nano Lett.* **2010**, *10*, 1055.
- (81) Qian, H.; Ellen, B.; Yan, Z.; Jin, R.; Huifeng, Q. *Acta. Phys. - Chim. Sin.* **2011**, *27*, 513.
- (82) Christensen, S. L.; Padmos, J. D.; Chatt, A.; Zhang, P. *Rev. Nanosci. Nanotechnol.* **2013**, *2*, 63.
- (83) Zhou, X.; Xu, W.; Liu, G.; Panda, D.; Chen, P. *J. Am. Chem. Soc.* **2010**, *132*, 138–46.
- (84) Haruta, M.; Daté, M. *Appl. Catal., A* **2001**, *222*, 427.
- (85) Rosi, N. L.; Mirkin, C. *Chem. Rev.* **2005**, *105*, 1547.
- (86) Boisselier, E.; Astruc, D. *Chem. Soc. Rev.* **2009**, *38*, 1759.
- (87) Gao, X. H.; Cui, Y. Y.; Levenson, R. M.; Chung, L. W. K.; Nie, S. M. *Nat. Biotechnol.* **2004**, *22*, 969–976.
- (88) Shim, S.-Y.; Lim, D.-K.; Nam, J.-M. *Nanomedicine* **2008**, *3*, 215.
- (89) Yen, C.-W.; Hayden, S. C.; Dreaden, E. C.; Szymanski, P.; El-Sayed, M. a *Nano Lett.* **2011**, *11*, 3821.
- (90) Ghosh, P.; Han, G.; De, M.; Kim, C. K.; Rotello, V. M. *Adv. Drug Delivery Rev.* **2008**, *60*, 1307.
- (91) Paciotti, G. F.; Myer, L.; Weinreich, D.; Goia, D.; Pavel, N.; McLaughlin, R. E.; Tamarkin, L. *Drug Deliv.* **2004**, *11*, 169.
- (92) Mout, R.; Moyano, D. F.; Rana, S.; Rotello, V. M. *Chem. Soc. Rev.* **2012**, *41*, 2539.

- (93) Chen, C.-L.; Rosi, N. L. *Angew. Chem. Int. Ed.* **2010**, *49*, 1924.
- (94) Tan, Y. N.; Lee, J. Y.; Wang, D. I. C. *J. Am. Chem. Soc.* **2010**, *132*, 5677.
- (95) Toroz, D.; Corni, S. *Nano Lett.* **2011**, *11*, 1313.
- (96) Keresteci, M.; Estabrooks, T.; Zhu, N.; Amuah, J.; Chen, S.; Marin, M.; Gu, J. *CJRR* **2009**.
- (97) Emery, D. F. G.; Clarke, H. J.; Grover, M. L. *J. Bone Joint Surg.* **1997**, *79-B*, 240.
- (98) Sato, M.; Webster, T. J. *Expert Rev. Med. Devic.* **2004**, *1*, 105.
- (99) Davila-Martinez, R.; Cueto, L.; Sanchez, E. *Surf. Sci.* **2006**, *600*, 3427.
- (100) Armelao, L.; Barreca, D.; Bottaro, G.; Gasparotto, A.; Tondello, E.; Ferroni, M.; Polizzi, S. *Chem. Mater.* **2004**, *16*, 3331.
- (101) Barreca, D.; Gasparotto, A.; Tondello, E.; Bruno, G.; Losurdo, M. *J. Appl. Phys.* **2004**, *96*, 1655.
- (102) Okumura, M.; Nakamura, S. *Stud. Surf. Sci. Catal.* **1998**, *118*, 277.
- (103) Parkhomenko, R. G.; Morozova, N. B.; Zharkova, G. I.; Shubin, Y. V.; Trubin, S. V.; Kriventsov, V. V.; Kuchumov, B. M.; Koretskaya, T. P.; Igumenov, I. K. *Chem. Vapor. Depos.* **2012**, *18*, 336.
- (104) Kokkinidis, G.; Papoutsis, A.; Stoychev, D.; Milchev, A. *J. Electroanal. Chem.* **2000**, *486*, 48.
- (105) Porter, L. a.; Choi, H. C.; Ribbe, A. E.; Buriak, J. M. *Nano Lett.* **2002**, *2*, 1067.
- (106) Padmos, J. D.; Duchesne, P.; Dunbar, M.; Zhang, P. *J. Biomed. Mater. Res., Part A* **2010**, *95A*, 146.
- (107) Christensen, S. L.; Chatt, A.; Zhang, P. *Langmuir* **2012**, *28*, 2979.
- (108) Christensen, S. L.; Chatt, A.; Zhang, P. *Langmuir* **2013**, *29*, 4894.
- (109) Li, L.-H.; Kong, Y.-M.; Kim, H.-W.; Kim, Y.-W.; Kim, H.-E.; Heo, S.-J.; Koak, J.-Y. *Biomater.* **2004**, *25*, 2867.
- (110) Das, K.; Bose, S.; Bandyopadhyay, A.; Karandikar, B.; Gibbins, B. L. *J. Biomed. Mater. Res., Part B* **2008**, *87*, 455–60.

- (111) Eisenbarth, E.; Velten, D.; Muller, M.; Thull, R.; Breme, J. *Biomater.* **2004**, *25*, 5705–5713.
- (112) Buser, D.; Broggini, N.; Wieland, M.; Schenk, R. K.; Denzer, A. J.; Cochran, D. L.; Hoffman, B.; Lussi, A.; Steinemann, S. G. *J. Dent. Res.* **2004**, *83*, 529.
- (113) Smith, B. D.; Liu, J. *J. Am. Chem. Soc.* **2010**, *132*, 6300.
- (114) Corma, A.; Serna, P. *Science* **2006**, *313*, 332.
- (115) Oliver-Meseguer, J.; Cabrero-Antonino, J. R.; Domínguez, I.; Leyva-Pérez, A.; Corma, A. *Science* **2012**, *338*, 1452.
- (116) Xie, S.; Tsunoyama, H.; Kurashige, W.; Negishi, Y.; Tsukuda, T. *ACS Catal.* **2012**, *2*, 1519.
- (117) Zhang, Y.; Cui, X.; Shi, F.; Deng, Y. *Chem. Rev.* **2012**, *112*, 2467.
- (118) Corma, A.; Juárez, R.; Boronat, M.; Sánchez, F.; Iglesias, M.; García, H. *Chem. Commun.* **2011**, *47*, 1446.
- (119) Hashmi, A. S. K.; Braun, I.; Rudolph, M.; Rominger, F. *Organometallics* **2012**, *31*, 644.
- (120) Leyva-Pérez, A.; Corma, A. *Angew. Chem. Int. Ed.* **2012**, *51*, 614.
- (121) Haruta, M.; Kobayashi, T.; Sano, H.; Yamada, N. *Chem. Lett.* **1987**, *16*, 405.
- (122) Hashmi, a S. K. *Science* **2012**, *338*, 1434.
- (123) Santra, a *Surf. Sci.* **2004**, *548*, 324.
- (124) Gao, Y.; Shao, N.; Zeng, X. C. *J. Chem. Phys.* **2008**, *129*.
- (125) Schierhorn, M.; Liz-Marzán, L. M. *Nano Lett.* **2002**, *2*, 13–16.
- (126) Lim, B.; Kobayashi, H.; Yu, T.; Wang, J.; Kim, M. J.; Li, Z.-Y.; Rycenga, M.; Xia, Y. *J. Am. Chem. Soc.* **2010**, *132*, 2506–7.
- (127) Kobayashi, Y.; Kiao, S.; Seto, M.; Takatani, H.; Nakanishi, M.; Oshima, R. *Hyperfine Interact.* **2004**, *156/157*, 75.
- (128) Jalilehvand, F. *Chem. Soc. Rev.* **2006**, *35*, 1256.

- (129) Bertin, E. P. *Introduction to X-Ray Spectrometric Analysis*; Plenum Press: New York, 1978.
- (130) Durham, P. J. *X-Ray Absorption*; Koningsberger, D. C.; Prins, R., Eds.; Chemical A.; Wiley-Interscience: New York, 1988.
- (131) Stohr, J. *NEXAFS Spectroscopy*; Springer: New York, 2003.
- (132) Christensen, S. L.; MacDonald, M. A.; Chatt, A.; Zhang, P.; Qian, H.; Jin, R. *J. Phys. Chem. C* **2012**, *116*, 26932.
- (133) Wu, Z.; Suhan, J.; Jin, R. *J. Mater. Chem.* **2009**, *19*, 622.
- (134) Jin, R.; Qian, H.; Wu, Z.; Zhu, Y.; Zhu, M.; Mohanty, A.; Garg, N. *J. Phys. Chem. Lett.* **2010**, *1*, 2903.
- (135) Nychyporuk, T.; Zhou, Z.; Fave, A.; Lemiti, M.; Bastide, S. *Sol. Energy Mater. Sol. Cells* **2010**, *94*, 2314.
- (136) Porter, L. a.; Choi, H. C.; Schmeltzer, J. M.; Ribbe, A. E.; Elliott, L. C. C.; Buriak, J. M. *Nano Lett.* **2002**, *2*, 1369.
- (137) Lim, Y. J.; Oshida, Y.; Andres, C. J.; Barco, M. T. *Int. J. Oral. Max. Surg.* **2001**, *16*, 333.
- (138) Chen, C.; Chen, J.; Chao, C.; Say, W. C. *J. Mater. Sci.* **2005**, *40*, 4053.
- (139) Kong, D.-S. *Langmuir* **2008**, *24*, 5324.
- (140) Takeuchi, M.; Abe, Y.; Yoshida, Y.; Nakayama, Y.; Okazaki, M.; Akagawa, Y. *Biomater.* **2003**, *24*, 1821.
- (141) Fjellstedt, E.; Harnevik, L.; Jeppsson, J.-O.; Tiselius, H.-G.; Söderkvist, P.; Denneberg, T. *Urol. Res.* **2003**, *31*, 417.
- (142) Ala, A.; Walker, A. P.; Ashkan, K.; Dooley, J. S.; Schilsky, M. L.; Park, F. *Lancet* **2007**, *369*, 397.
- (143) Simpson, C. A.; Farrow, C. L.; Tian, P.; Billinge, S. J. L.; Huffman, B. J.; Harkness, K. M.; Cliffler, D. E. *Inorg. Chem.* **2010**, *49*, 10858.
- (144) Sham, T. K.; Kim, P. S. G.; Zhang, P. *Solid State Commun.* **2006**, *138*, 553.
- (145) Zhang, P.; Zhou, X. T.; Tang, Y. H.; Sham, T. K. *Langmuir* **2005**, *21*, 8502.

- (146) Xie, J. P.; Zheng, Y. G.; Ying, J. Y. *J. Am. Chem. Soc.* **2009**, *131*, 888.
- (147) Moulder, J.; Stickle, W. F.; Sobol, P. E.; Bomben, K. D. *Handbook of X-Ray Photoelectron Spectroscopy*; Muilenberg, G., Ed.; Perkin-Elmer: Eden Prairie, 1992; p. 261.
- (148) Brewer, S. H.; Glomm, W. R.; Johnson, M. C.; Knag, M. K.; Franzen, S. *Langmuir* **2005**, *21*, 9303.
- (149) Simms, G. A.; Padmos, J. D.; Zhang, P. *J. Chem. Phys.* **2009**, *131*, 214703.
- (150) Voicescu, M.; Ionescu, S.; Angelescu, D. G. *J. Nanopart. Res.* **2012**, *14*, 1174.
- (151) Zhang, X.-D.; Wu, D.; Shen, X.; Liu, P.-X.; Fan, F.-Y.; Fan, S.-J. *Biomater.* **2012**, *33*, 4628.
- (152) Pompella, A.; Visvikis, A.; Paolicchi, A.; Tata, V. De; Casini, A. F. *Biochem. Pharmacol.* **2003**, *66*, 1499.
- (153) Schaaff, T. G.; Knight, G.; Shafiqullin, M. N.; Borkman, R. F.; Whetten, R. L. *J. Phys. Chem. B* **1998**, *102*, 10643.
- (154) Wu, Z.; Gayathri, C.; Gil, R. R.; Jin, R. *J. Am. Chem. Soc.* **2009**, *131*, 6535–42.
- (155) Attwood, D. *Soft X-Rays and Extreme Ultraviolet Radiation: Principles and Applications.*; Cambridge University Press: Berkeley, 2007.
- (156) Regier, T.; Chevrier, D. High Resolution Spherical Grating Monochromator (SGM) 11ID-1 http://exshare.lightsource.ca/sgm/Pages/SGM_Home.aspx.
- (157) Hu, Y. Soft X-ray Microcharacterization Beamline (SXRMB) 06B1-1 <http://www.lightsource.ca/experimental/sxrmb.php>.
- (158) Chen, N.; Chen, W. Hard X-ray MicroAnalysis (HXMA) 06ID-1 <http://exshare.lightsource.ca/hxma/Pages/HXMAHome.aspx>.
- (159) Gordon, R. X-ray Science Division partnered with the Pacific Northwest Consortium Advanced Photon Source, Sector 20 <http://www.sfu.ca/~ragordon/sector20/bm.htm>.
- (160) Ghosh, P. K. *Introduction to photoelectron spectroscopy*; Wiley: New York, 1983; p. 377.
- (161) Hufner, S. *Photoelectron Spectroscopy*; Springer: New York, 2003.

- (162) Bunker, G. *Introduction to XAFS: A Practical Guide to X-ray Absorption Fine Structure Spectroscopy*; Cambridge University Press: Cambridge, 2010.
- (163) Ressler, T. *J. Synch. Rad.* **1998**, *5*, 118.
- (164) Cormier, Z. R.; Andreas, H. A.; Zhang, P. *J. Phys. Chem. C* **2011**, *115*, 19117.
- (165) MacDonald, M. A.; Chevrier, D. M.; Zhang, P.; Qian, H. F.; Jin, R. C. *J. Phys. Chem. C* **2011**, *115*, 15282.
- (166) Liu, F.; Wechsler, D.; Zhang, P. *Chem. Phys. Lett.* **2008**, *461*, 254.
- (167) Newville, M. *J. Synch. Rad.* **2001**, *8*, 322.
- (168) Ankudinov, A. L.; Ravel, B.; Rehr, J. J.; Conradson, S. D. *Phys. Rev. B* **1998**, *58*, 7565.
- (169) Simchi, A.; Tamjid, E.; Pishbin, F.; Boccaccini, a R. *Nanomed. Nanotechnol. Biol. Med.* **2011**, *7*, 22.
- (170) Variola, F.; Brunski, J. B.; Orsini, G.; Tambasco de Oliveira, P.; Wazen, R.; Nanci, A. *Nanoscale* **2011**, *3*, 335.
- (171) Tran, N.; Webster, T. J. *Rev. Nanomed. Nanobiotechnol.* **2009**, *1*, 336.
- (172) Montanaro, L.; Campoccia, D.; Arciola, C. R. *Int. J. Artif. Organs* **2008**, *31*, 771.
- (173) Geetha, M.; Singh, A. K.; Asokamani, R.; Gogia, A. K. *Prog. Mater Sci.* **2009**, *54*, 397.
- (174) Rack, H. J.; Long, M. *Biomater.* **1998**, *19*, 1621.
- (175) Morra, M. *Expert Rev. Med. Devic.* **2007**, *4*, 361.
- (176) Nanci, A.; Wuest, J. D.; Peru, L.; Brunet, P.; Sharma, V.; Zalzal, S.; McKee, M. D. *J. Biomed. Mater. Res., Part A* **1998**, *40*, 324.
- (177) Streicher, R. M.; Schmidt, M.; Fiorito, S. *Nanomedicine* **2007**, *2*, 861.
- (178) Armelao, L.; Barreca, D.; Gasparotto, A.; Pierangelo, E.; Tondello, E.; Polizzi, S. *J. Nanosci. Nanotechnol.* **2005**, *5*, 259.
- (179) Tran, P. a; Sarin, L.; Hurt, R. H.; Webster, T. J. *J. Biomed. Mater. Res., Part A* **2010**, *93*, 1417.

- (180) Zhao, L.; Wang, H.; Huo, K.; Cui, L.; Zhang, W.; Ni, H.; Zhang, Y.; Wu, Z.; Chu, P. K. *Biomater.* **2011**, *32*, 5706.
- (181) Kiyonaga, T.; Jin, Q.; Kobayashi, H.; Tada, H. *ChemPhysChem* **2009**, *10*, 2935.
- (182) Chua, P. H.; Neoh, K. G.; Kang, E. T.; Wang, W. *Biomater.* **2008**, *29*, 1412.
- (183) Puleo, D. A.; Nanci, A. *Biomater.* **1999**, *20*, 2311.
- (184) Wilson, C. J.; Clegg, R. E.; Leavesley, D. I.; Pearcy, M. J. *Tissue Eng.* **2005**, *11*, 1.
- (185) MacDonald, M. A.; Zhang, P.; Qian, H. F.; Jin, R. C. *J. Phys. Chem. Lett.* **2010**, *1*, 1821.
- (186) Wagner, C. D.; Davis, L. E.; Zeller, M. V.; Taylor, J. A.; Raymond, R. H.; Gale, L. H. *Surf. Interface Anal.* **1981**, *3*, 211.
- (187) Zhang, P.; Sham, T. *Phys. Rev. Lett.* **2003**, *90*, 245502.
- (188) Cook, S. C.; Padmos, J. D.; Zhang, P. *J. Chem. Phys.* **2008**, *128*, 154705.
- (189) Wei, H.; Wang, Z.; Zhang, J.; House, S.; Gao, Y.-G.; Yang, L.; Robinson, H.; Tan, L. H.; Xing, H.; Hou, C.; Robertson, I. M.; Zuo, J.-M.; Lu, Y. *Nat. Nanotechnol.* **2011**, *6*, 93.
- (190) Barreca, D.; Gasparotto, A.; Maragno, C.; Tondello, E.; Gialanella, S. *J. Appl. Phys.* **2005**, *97*, 054311.
- (191) Kim, J. S.; Kuk, E.; Yu, K. N.; Kim, J.-H.; Park, S. J.; Lee, H. J.; Kim, S. H.; Park, Y. K.; Park, Y. H.; Hwang, C.-Y.; Kim, Y.-K.; Lee, Y.-S.; Jeong, D. H.; Cho, M.-H. *Nanomed. Nanotechnol. Biol. Med.* **2007**, *3*, 95.
- (192) Weng, H.-A.; Wu, C.-C.; Chen, C.-C.; Ho, C.-C.; Ding, S.-J. *J. Mater. Sci. - Mater. Med.* **2010**, *21*, 1511.
- (193) Xia, Y.; Xiong, Y. J.; Lim, B.; Skrabalak, S. E. *Angew. Chem. Int. Ed.* **2009**, *48*, 60.
- (194) Schwartz, V.; Mullins, D. R.; Yan, W.; Zhu, H.; Dai, S.; Overbury, S. H. *J. Phys. Chem. C* **2007**, *111*, 17322.
- (195) Cha, S.; Kim, J.-U.; Kim, K.; Lee, J. *Chem. Mater.* **2007**, *19*, 6297.
- (196) Renevier, H.; Proietti, M. G.; Grenier, S.; Ciatto, G.; González, L.; García, J. M.; Gérard, J. M. *Mater. Sci. Eng., B* **2003**, *101*, 174.

- (197) Turchini, S.; Proietti, M. G.; Martelli, F.; Prosperi, T.; García, J. *Physica B* **1995**, *208-209*, 557.
- (198) MacDonald, M. A.; Zhang, P.; Chen, N.; Qian, H. F.; Jin, R. C. *J. Phys. Chem. C* **2011**, *115*, 65.
- (199) Chevrier, D. M.; MacDonald, M. A.; Chatt, A.; Zhang, P.; Wu, Z.; Jin, R. *J. Phys. Chem. C* **2012**, *116*, 25137.
- (200) Schaaff, T. G.; Shafigullin, M. N.; Khoury, J. T.; Vezmar, I.; Whetten, R. L. *J. Phys. Chem. B* **2001**, *105*, 8785.
- (201) Fields-Zinna, C. A.; Sardar, R.; Beasley, C. a; Murray, R. W. *J. Am. Chem. Soc.* **2009**, *131*, 16266.
- (202) Jiang, D.-E.; Tiago, M. L.; Luo, W.; Dai, S. *J. Am. Chem. Soc.* **2008**, *130*, 2777.
- (203) Aikens, C. M. *J. Phys. Chem. Lett.* **2011**, *2*, 99.
- (204) Aikens, C. M. *J. Phys. Chem. Lett.* **2010**, *1*, 2594.
- (205) Kelly, K. L.; Coronado, E.; Zhao, L. L.; Schatz, G. C. *J. Phys. Chem. B* **2003**, *107*, 668.
- (206) Alvarez, M. M.; Khoury, J. T.; Schaaff, T. G.; Shafigullin, M. N.; Vezmar, I.; Whetten, R. L. *J. Phys. Chem. B* **1997**, *101*, 3706.
- (207) Haruta, M. *CATTECH* **2002**, *6*, 102.
- (208) Burt, J. L.; Gutiérrez-Wing, C.; Miki-Yoshida, M.; José-Yacamán, M. *Langmuir* **2004**, *20*, 11778.
- (209) Pei, Y.; Gao, Y.; Shao, N.; Zeng, X. C. *J. Am. Chem. Soc.* **2009**, *131*, 13619.
- (210) Zhu, M.; Qian, H.; Jin, R. *J. Phys. Chem. Lett.* **2010**, *1*, 1003.
- (211) Maeland, A.; Flanagan, T. B. *J. Phys. Chem.* **1965**, *69*, 3575.
- (212) Wang, E. A.; Israel, D. I.; Kelly, S.; Luxenberg, D. P. *Growth Factors* **1993**, *9*, 57.
- (213) Shichibu, Y.; Negishi, Y.; Tsunoyama, H.; Kanehara, M.; Teranishi, T.; Tsukuda, T. *Small* **2007**, *3*, 835.
- (214) Kumara, C.; Dass, A. *Nanoscale* **2011**, *3*, 3064.

- (215) Kumara, C.; Dass, A. *Nanoscale* **2012**, *4*, 4084.
- (216) Fields-Zinna, C. A.; Crowe, M. C.; Dass, A.; Weaver, J. E. F.; Murray, R. W. *Langmuir* **2009**, *25*, 7704.
- (217) Negishi, Y.; Iwai, T.; Ide, M. *Chem. Commun.* **2010**, *46*, 4713–5.
- (218) Negishi, Y.; Munakata, K.; Ohgake, W.; Nobusada, K. *J. Phys. Chem. Lett.* **2012**, *3*, 2209–2214.
- (219) Negishi, Y.; Igarashi, K.; Munakata, K.; Ohgake, W.; Nobusada, K. *Chem. Commun.* **2012**, *48*, 660–2.
- (220) Sinfelt, J. H.; Meitzner, G. D. *Acc. Chem. Res.* **1993**, *26*, 1–6.
- (221) Benfield, R. E.; Grandjean, D.; Kröll, M.; Pugin, R.; Sawitowski, T.; Schmid, G. *J. Phys. Chem. B* **2001**, *105*, 1961.
- (222) Chen, L. X.; Jäger, W. J.; Jennings, G.; Gosztola, D. J.; Munkholm, A.; Hessler, J. *P. Science* **2001**, *292*, 262.
- (223) Sellmann, D.; Häußinger, D.; Heinemann, F. W. *Eur. J. Inorg. Chem.* **1999**, 1715.
- (224) Jiang, D.; Dai, S. *Inorg. Chem.* **2009**, *48*, 2720.
- (225) Wolter, S. D.; Brown, B.; Parker, C. B.; Stoner, B. R.; Glass, J. T. *Appl. Surf. Sci.* **2010**, *257*, 1431.
- (226) Park, Y. S.; Whalley, A. C.; Kamenetska, M.; Steigerwald, M. L.; Hybertsen, M. S.; Nuckolls, C.; Venkataraman, L. *J. Am. Chem. Soc.* **2007**, *129*, 15768.
- (227) Xia, B.-H.; Zhang, H.-X.; Che, C.-M.; Leung, K.-H.; Phillips, D. L.; Zhu, N.; Zhou, Z.-Y. *J. Am. Chem. Soc.* **2003**, *125*, 10362.
- (228) Zhang, P.; Sham, T. K. *Appl. Phys. Lett.* **2002**, *81*, 736.
- (229) Pei, Y.; Zeng, X. C. *Nanoscale* **2012**, *4*, 4054.
- (230) Puleo, D. .; Kissling, R. .; Sheu, M.-S. *Biomater.* **2002**, *23*, 2079.
- (231) Zhang, H.; Fu, Q.; Yao, Y.; Zhang, Z.; Ma, T.; Tan, D.; Bao, X. *Langmuir* **2008**, *24*, 10874.

APPENDIX A

A-1. Study of Silver Nanoparticles

Ag:BSA Systems

Ag:BSA samples were produced for metallic comparison with Au:BSA samples. Ag forms Ti-supported NPs similar in size to Au NPs but are more reactive.²³¹ Although the conditions are similar, Ag-S bonds are not as strong as Au-S bonds. SEM micrographs of the 20:1, 5:1, and 2:1 Ag:BSA systems were taken to determine the effect of concentration on surface coverage, as well as the resulting nanoparticle sizes (Figure A-1).

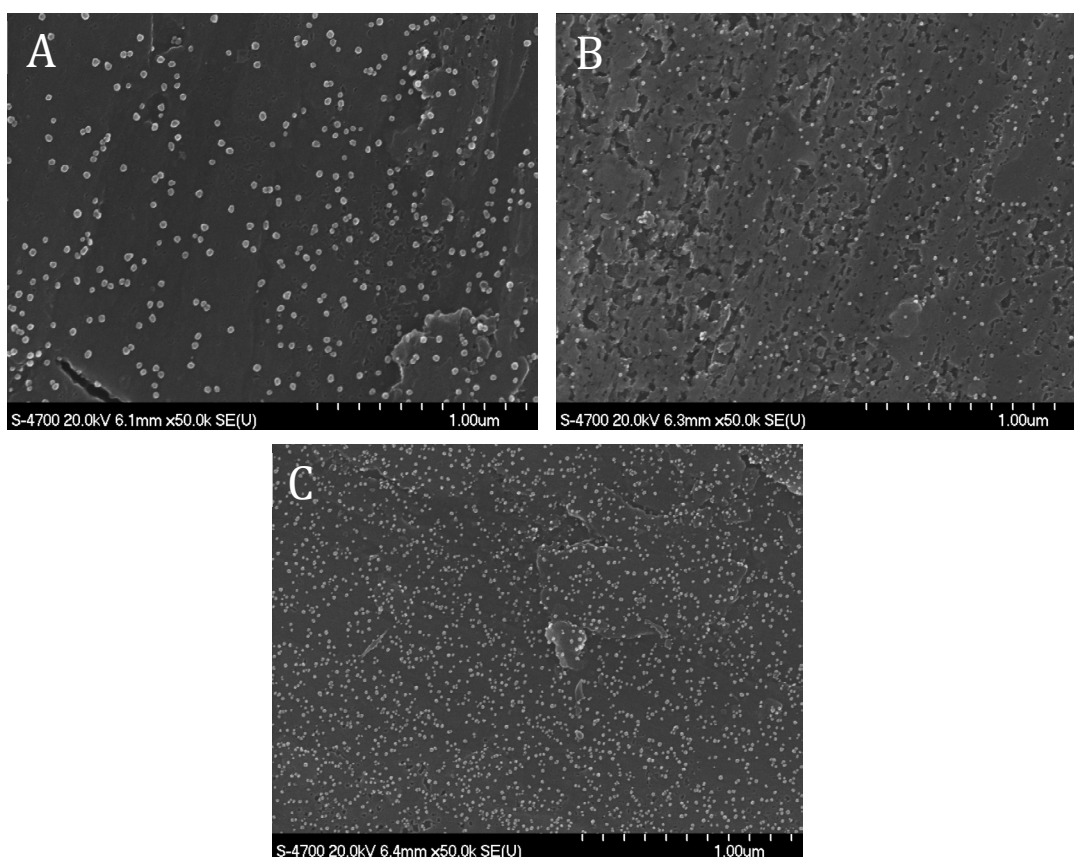


Figure A-1. SEM Micrographs of Ag:BSA on titanium system. A) 20:1 Ag:BSA, B) 5:1 Ag:BSA and C) 2:1 Ag:BSA.

Interestingly, changes in concentration of the ligand affect the Ag:BSA systems differently than those of Au:BSA. In contrast with the Au:BSA systems, there is a noticeable trend towards increasing coverage and decreasing particle size with increasing concentration of BSA. This is of interest as the proposed mechanism for Au:BSA nanoparticle formation is the inward-facing cysteine groups of the BSA protein. It is therefore hypothesized that inward-facing thiol groups have the same effect on Ag.

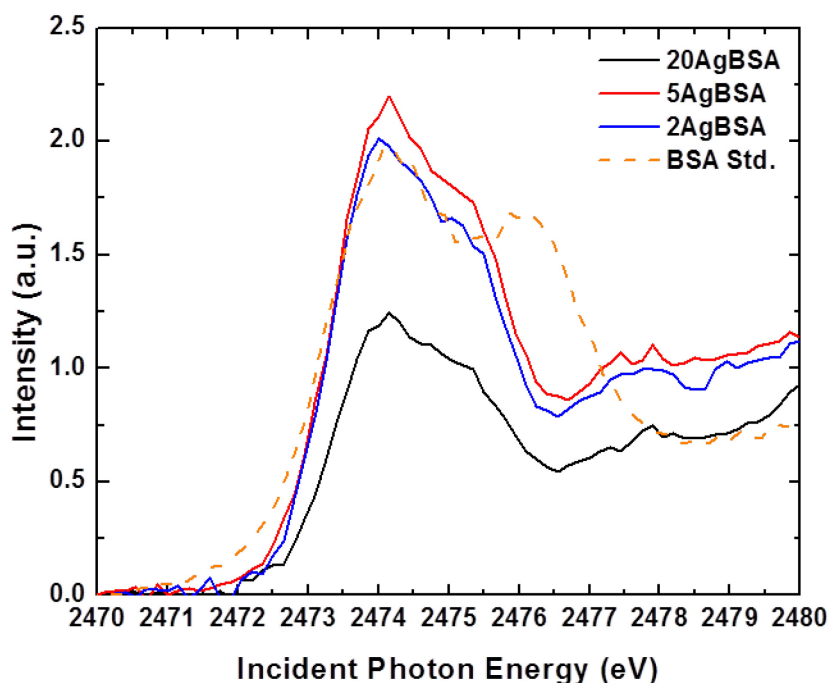


Figure A-2. Sulfur K-edge XANES spectra of 20:1, 5:1, and 2:1 Ag:BSA on titanium, in comparison with a BSA standard.

Figure A-2 is the S K-edge XANES spectrum of the 20:1, 5:1, and 2:1 Ag:BSA systems in comparison with the BSA standard pure component spectrum. The peak positions are similar to the Au:BSA system, as well as the disulfide feature and its disappearance with Ag-S bonding. There is no discernible shift towards higher binding energy with decreasing

particle size, which is curious as one would expect more surface interaction with smaller particle size.

XPS experiments on the Ag:BSA system show a narrowing of the Ag 3d XPS peaks with increasing concentration of BSA ligand. This may be indicative of the smaller particle size seen with a decreasing Ag:BSA ratio. The S K-edge XANES spectrum for these particles shows a clear difference in the width of the Ag-bound BSA peak, most likely due to the binding. There is a slight shift towards lower binding energy with increasing ligand concentration, which may be due to the smaller particle size and therefore more Ag-thiolate surface interaction expected in smaller particles.

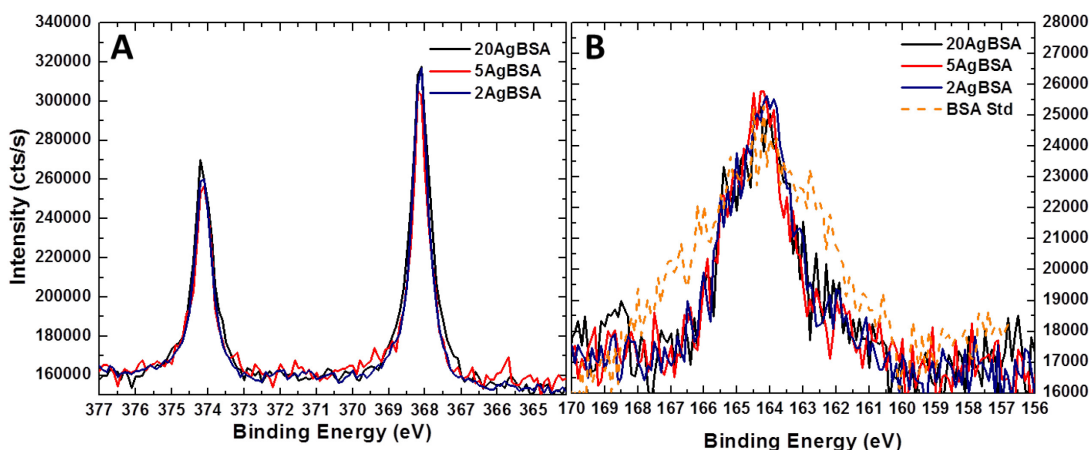


Figure A-3. XPS spectrum of Au:BSA on titanium. A) Ag 3d spectra, B) S 2p spectra with BSA standard for comparison.

Ag:MPG Systems

The Ag:MPG system, much like the Au:MPG system has less coverage due to MPG in the 2:1 Ag:MPG system, reducing the aggregation of Ag before nanoparticle formation on

the titanium surface. The 20:1 and 5:1 Ag:MPG systems demonstrate similar coverage, and nanoparticle sizes (~5 nm), although particle distribution and size analysis is yet to be done.

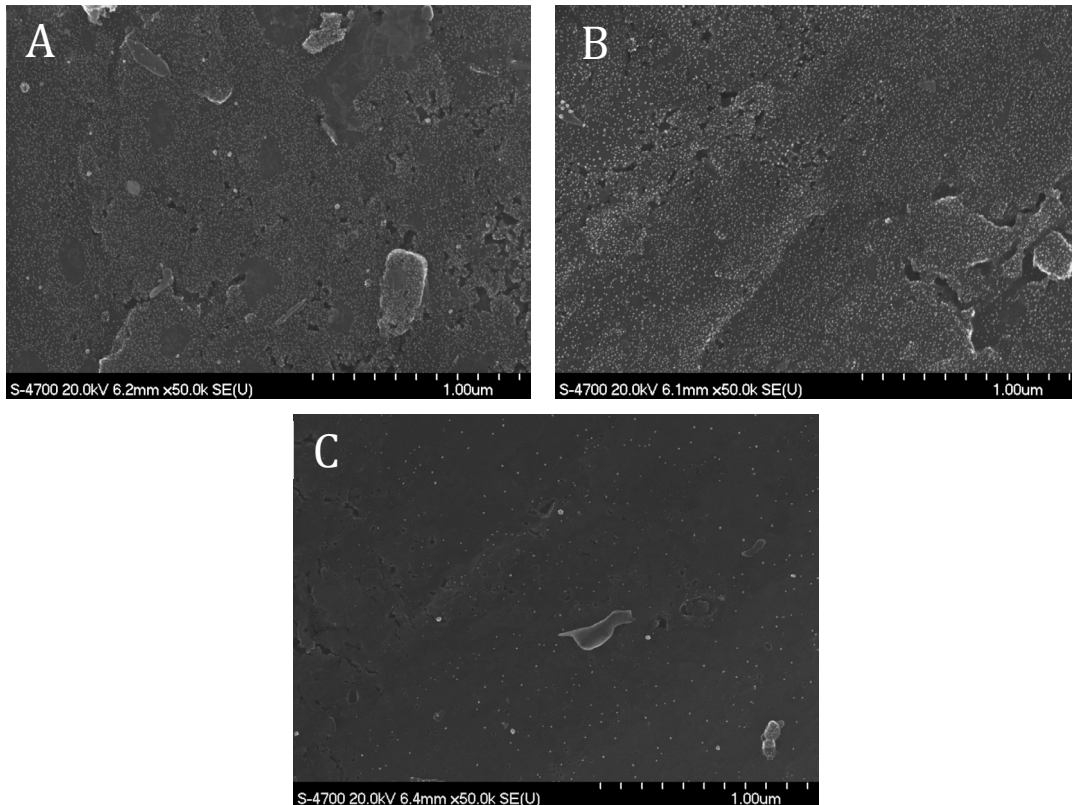


Figure A-4. SEM Micrographs of Ag:MPG on titanium system. A) 20:1 Ag:MPG, B) 5:1 Ag:MPG and C) 2:1 Ag:MPG.

In the S K-edge XANES spectrum, the deviation from the MPG standard pure component spectrum indicates that the spectra of the Ag:MPG systems is due to Ag-S bonding. The difference in peak intensity is most likely due to surface coverage. 2:1 Ag:MPG, with the least surface coverage, shows greatly reduced Ag-S signal.

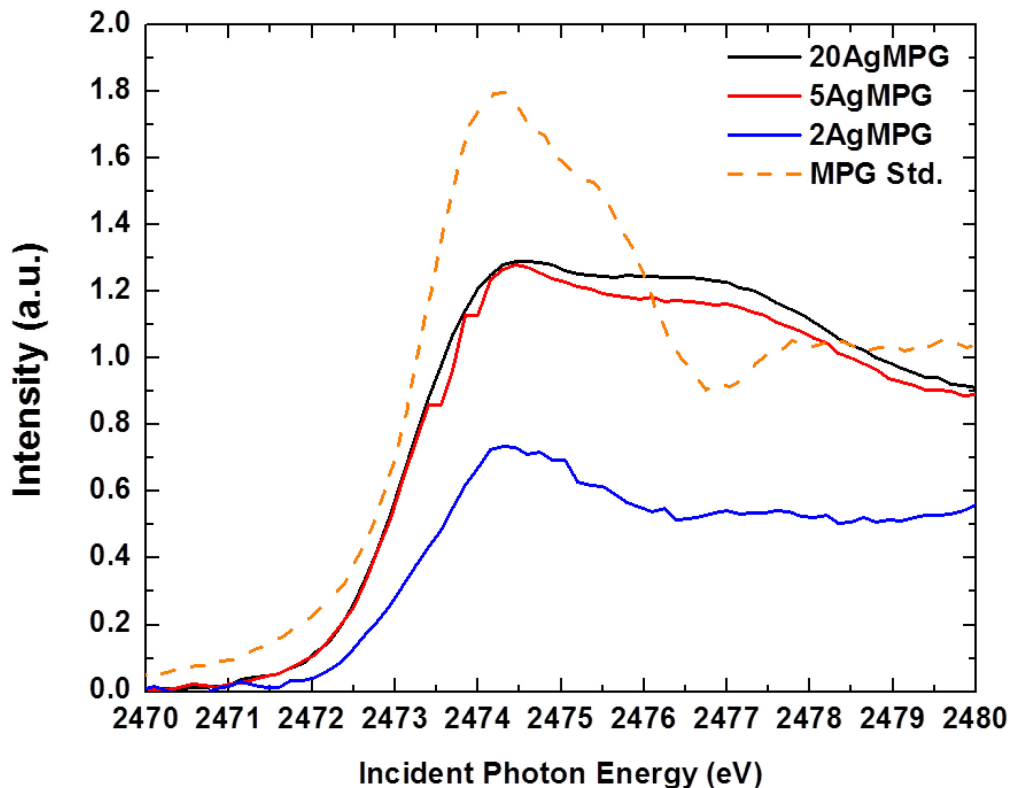


Figure A-5. Sulfur K-edge XANES spectra of 20:1, 5:1, and 2:1 Ag:MPG on titanium, in comparison with a MPG standard.

The Ag 3d XPS spectra of the Ag:MPG system is somewhat confusing, as the trend seen in the Ag 3d_{5/2} peak is different from that seen in the Ag 3d_{3/2} peak. This may be due to the low signal of the 2Ag:MPG system, as the 20:1 vs. 5:1 Ag:MPG trend is similar to that seen in their respective Au:MPG systems. The S 2p XPS spectra show similarity between the 20:1 and 5:1 Ag:MPG systems, as they have more Ag-S bonding.

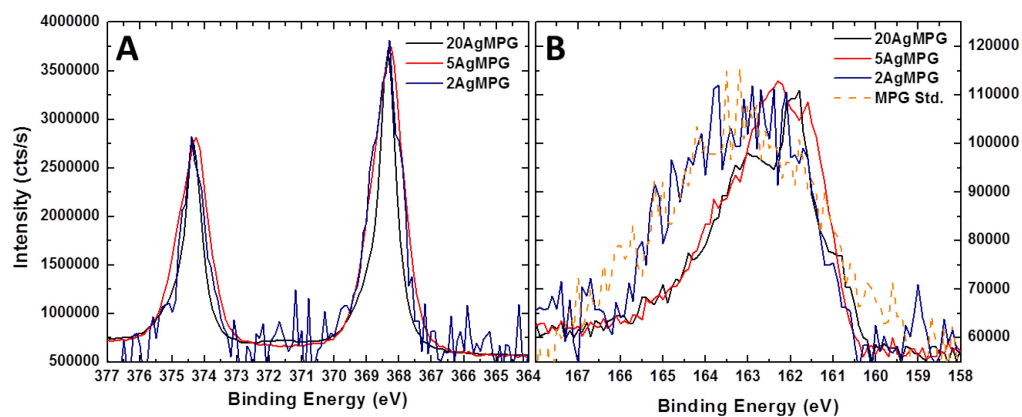


Figure A-6. XPS spectrum of Au:MPG on titanium. A) Ag 3d spectra, B) S 2p spectra with MPG standard for comparison.

APPENDIX B

B-1. Copyright Agreement Letter – Chapter 3

28/01/2013

Rightslink® by Copyright Clearance Center



RightsLink®

Home

Account
Info

Help



ACS Publications
High quality High impact.

Title: Biomolecule-Coated Metal Nanoparticles on Titanium
Author: Stephen L. Christensen, Amares Chatt, and Peng Zhang
Publication: Langmuir
Publisher: American Chemical Society
Date: Feb 1, 2012
Copyright © 2012, American Chemical Society

Logged in as:
Stephen Christensen
Account #:
3000503867

LOGOUT

PERMISSION/LICENSE IS GRANTED FOR YOUR ORDER AT NO CHARGE

This type of permission/license, instead of the standard Terms & Conditions, is sent to you because no fee is being charged for your order. Please note the following:

- Permission is granted for your request in both print and electronic formats, and translations.
- If figures and/or tables were requested, they may be adapted or used in part.
- Please print this page for your records and send a copy of it to your publisher/graduate school.
- Appropriate credit for the requested material should be given as follows: "Reprinted (adapted) with permission from (COMPLETE REFERENCE CITATION). Copyright (YEAR) American Chemical Society." Insert appropriate information in place of the capitalized words.
- One-time permission is granted only for the use specified in your request. No additional uses are granted (such as derivative works or other editions). For any other uses, please submit a new request.

BACK

CLOSE WINDOW

Copyright © 2013 [Copyright Clearance Center, Inc.](#) All Rights Reserved. [Privacy statement.](#)
Comments? We would like to hear from you. E-mail us at customercare@copyright.com

B-2. Copyright Agreement Letter – Chapter 4

3/28/13

Rightslink® by Copyright Clearance Center



RightsLink®

[Home](#)[Account Info](#)[Help](#)

ACS Publications
High quality High impact.

Title: Peptide-Directed Preparation and X-ray Structural Study of Au Nanoparticles on Titanium Surfaces

Author: Stephen Lynd Christensen, Amares Chatt, and Peng Zhang

Publication: Langmuir

Publisher: American Chemical Society

Date: Mar 1, 2013

Copyright © 2013, American Chemical Society

Logged in as:
Stephen Christensen
Account #:
3000503867

[LOGOUT](#)

PERMISSION/LICENSE IS GRANTED FOR YOUR ORDER AT NO CHARGE

This type of permission/license, instead of the standard Terms & Conditions, is sent to you because no fee is being charged for your order. Please note the following:

- Permission is granted for your request in both print and electronic formats, and translations.
- If figures and/or tables were requested, they may be adapted or used in part.
- Please print this page for your records and send a copy of it to your publisher/graduate school.
- Appropriate credit for the requested material should be given as follows: "Reprinted (adapted) with permission from (COMPLETE REFERENCE CITATION). Copyright (YEAR) American Chemical Society." Insert appropriate information in place of the capitalized words.
- One-time permission is granted only for the use specified in your request. No additional uses are granted (such as derivative works or other editions). For any other uses, please submit a new request.

[BACK](#)[CLOSE WINDOW](#)

Copyright © 2013 [Copyright Clearance Center, Inc.](#) All Rights Reserved. [Privacy statement.](#) Comments? We would like to hear from you. E-mail us at customercare@copyright.com

B-3. Copyright Agreement Letter – Chapter 6

29/01/2013

Rightslink® by Copyright Clearance Center



RightsLink®

[Home](#)[Account Info](#)[Help](#)

ACS Publications
High quality High impact.

Title: Dopant Location, Local Structure, and Electronic Properties of Au₂₄Pt(SR)₁₈ Nanoclusters

Author: Stephen L. Christensen, Mark A. MacDonald, Amares Chatt, Peng Zhang, Huifeng Qian, and Rongchao Jin

Publication: The Journal of Physical Chemistry C

Publisher: American Chemical Society

Date: Dec 1, 2012

Copyright © 2012, American Chemical Society

Logged in as:
Stephen Christensen
Account #: 3000503867

[LOGOUT](#)

PERMISSION/LICENSE IS GRANTED FOR YOUR ORDER AT NO CHARGE

This type of permission/license, instead of the standard Terms & Conditions, is sent to you because no fee is being charged for your order. Please note the following:

- Permission is granted for your request in both print and electronic formats, and translations.
- If figures and/or tables were requested, they may be adapted or used in part.
- Please print this page for your records and send a copy of it to your publisher/graduate school.
- Appropriate credit for the requested material should be given as follows: "Reprinted (adapted) with permission from (COMPLETE REFERENCE CITATION). Copyright (YEAR) American Chemical Society." Insert appropriate information in place of the capitalized words.
- One-time permission is granted only for the use specified in your request. No additional uses are granted (such as derivative works or other editions). For any other uses, please submit a new request.

[BACK](#)[CLOSE WINDOW](#)

Copyright © 2013 [Copyright Clearance Center, Inc.](#) All Rights Reserved. [Privacy statement.](#) Comments? We would like to hear from you. E-mail us at customercare@copyright.com